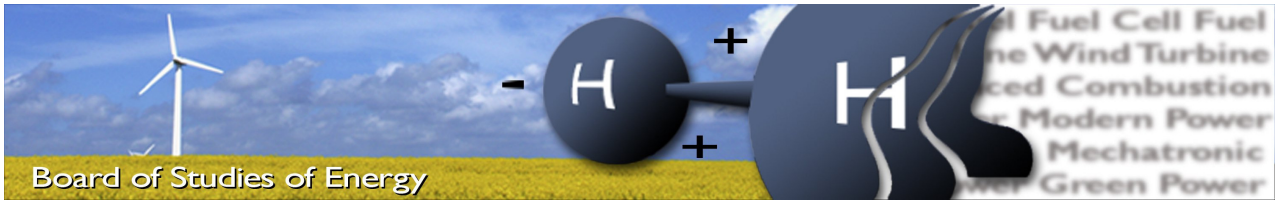


# Modeling and Validation of the SR-30 Turbojet Engine



Thermal Energy Technology  
6. Semester  
Group TE6-604  
Aalborg University





**Title:** Modeling and Validation of the SR-30 Turbojet Engine

**Semester:** 6.

**Semester theme:** Flow Machines

**Project period:** 02.02.12 to 25.05.12

**ECTS:** 19

**Supervisor:** Thomas Condra & Lasse Aistrup Rosendahl

**Project group:** ET6-604

---

Claus Uhrenholt Jensen

---

Hélène Lebreton

---

Simon Sand Nielsen

---

Kristine Møllenbach Rasmussen

**Synopsis:**

The first step of combining biofuels and aviation requires a model of the examined turbojet engine. The aim of the project is a validated performance model of the SR-30 turbojet engine. The modeling is based on compressible and isentropic flow relations and two dimensional velocity triangles. The modeling predicts a pressure ratio across the compressor of 3.4 at 80,000 RPM, whereas test runs reveal 3.1. Although incidence losses, disk friction, friction in the blade rows and slip are accounted for, the model seems to overestimate the performance of the compressor and the turbine. The predicted thrust equals that measured during test runs, and thus the modeling of mass flow entering the engine is considered accurate. The modeling predicts performance of the SR-30 engine with an accuracy sufficient to analyse the tendencies when changing variables. The accuracy of the modeling approach is expected to rise, when applied at larger engines, since the negative impact of using two dimensional velocity triangles is reduced.

**Copies:** 7

**Pages, total:** 107

**Appendix:** A-F

**Supplements:** CD

**By signing this document, each member of the group confirms that all participated in the project work and thereby all members are collectively liable for the content of the report.**



# Summary

---

A first step of combining biofuels and aviation is, according to interest groups, engine and fuel testing rather than flight testing. A validated model of the particular engine that is examined is required in order to succeed with this first step. The ability of modeling a particular engine just by the use of engine dimensions is inspiring, as this enables modeling of various turbojet engines. The SR-30 turbojet engine has been available at Aalborg University during the project period and thus, the aim of the project has been to present a modeling approach that predicts the performance of this particular engine with high accuracy. Furthermore, the model is validated by test runs of the SR-30 engine.

Firstly, drawings of the SR-30 engine have been analysed and based on these, considerations prior to the modeling are discussed. Relevant dimensions are presented and related to theory that describes the choice of design. In addition, the manufacturer may have compromised with the design optimum in order to ensure a wider range of performance or flow stability. This may result in losses, which is also discussed.

Secondly, the premises for choosing compressible flow conditions instead of incompressible are presented. General formulas, applicable for compressible flows are listed, and the use of these in the modeling is explained. Furthermore, the modeling approach specific to each component of the SR-30 engine is explained. The effect incidence losses, slip and deviation have on the velocity triangles is sketched and explained. To model the combustion chamber of the SR-30 engine, experiments have been performed. The experiments are explained and the outcome is evaluated prior to implementation in the combustion model.

Finally, the modeling results are evaluated at a range of engine speeds and compared to the measurements obtained during test runs. The results are analysed and possible improvements are considered. It is found by comparison that the modeling seem to overestimate the performance of the compressor and turbine. The modeling of incidence losses are analysed thoroughly, since they form an issue with respect to energy balances.

The predicted thrust equals that of the measurements and based on that it is concluded that the mass flow of air entering the engine is modeled accurately. In general, the model predictions have the same tendencies as the measurements when the engine speed is varied. The model is considered valid to the extend of predicting the performance of the SR-30 engine with an accuracy that is sufficient to analyse the tendencies when changing for instance the fuel. The modeling does however not predict the performance of the SR-30 engine with a high accuracy as aimed for in the problem statement. When using two dimensional velocity triangles to model small scale engines, the impact of neglecting the third velocity component rises. Thus it is expected that the modeling approach will reveal accurate results with respect to turbojet engines at a larger scale.



# Preface

---

This report is carried out by a group of 6<sup>th</sup> semester students from the department of Thermal Energy Technology at Aalborg University. The overall theme for this project is *Flow machines*.

## Reading Guide

References are made using the Harvard method, where the reference in the text will be included as (Name, Year). In the bibliography article and book references are stated with author, title, edition, publisher and year and websites are stated with author, title, hyperlink and date.

Figures, tables and equations have numbers that indicate to which chapter they belong, and a number that indicates which number of figure, table or equation in the chapter it is. E.g. The first figure in chapter 4 will have number 4.1 and the second will have number 4.2. There is a caption to each figure and table. Appendixes are indicated with a capital letter. E.g. the first appendix will be appendix A.

A CD containing all program files and a PDF-version of the report is attached. The files on the CD are listed in appendix F. The references to these files in the text will be a reference to appendix F. A digital copy of the report is also attached on the CD.



# Nomenclature

Symbol	Description	Unit
$A$	Area	$m^2$
$\alpha$	Angle between absolute velocity and axial or radial direction	$^\circ$
$\beta$	Angle between relative velocity and axial or radial direction	$^\circ$
$c$	Speed of sound	$m/s$
$E_T$	Relative error	.
$h$	Enthalphy	$J/kg$
$\Delta h_{i1}$	Specific incidence loss	$J/kg$
$\Delta h_{f1}$	Specific friction loss	$J/kg$
$\Delta h_{d1}$	Specific disk loss	$J/kg$
$\kappa$	Specific heat ratio	.
$\dot{m}$	Mass flow	$kg/s$
$Ma$	Mach number	.
$\eta$	Efficiency	.
$\sigma$	Slip and deviation factor	.
$P$	Static pressure	kPa
$P_0$	Stagnation pressure	kPa
$\rho$	Density	$kg/m^3$
$R$	Degree of reaction	.
$r$	Local radius	$m$
$T$	Static temperature	$K$
$T_0$	Stagnation temperature	$K$
$U$	Tip speed of impeller or turbine rotor	$m/s$
$\bar{U}$	Tip speed of impeller or turbine rotor as a 2D vector	$m/s$
$V$	Absolute velocity	$m/s$
$\bar{V}$	Absolute velocity as a 2D vector	$m/s$
$V_\theta$	Tangential component of the absolute velocity	$m/s$
$V_{Ax}$	Axial component of the absolute velocity	$m/s$
$V_r$	Radial component of the absolute velocity	$m/s$
$\dot{w}$	Specific work	$J/kg$
$W$	Relative Velocity	$m/s$
$\bar{W}$	Relative velocity vector	$m/s$
$W_{Ax}$	Axial component of the relative velocity	$m/s$
$W_\theta$	Tangential component of the relative velocity	$m/s$
$W_r$	Radial component of the relative velocity	$m/s$



# Contents

---

<b>1</b>	<b>Biofuel in Aviation Requires Modeling</b>	<b>1</b>
1.1	Problem Statement . . . . .	1
<b>2</b>	<b>Premodeling Considerations</b>	<b>3</b>
2.1	The Single Stage Centrifugal Compressor . . . . .	4
2.2	Considerations Related to the Combustion . . . . .	9
2.3	The Single Stage Axial Turbine . . . . .	10
2.4	Nozzles at Subsonic Flows . . . . .	13
<b>3</b>	<b>Modeling of the SR-30 Turbojet Engine</b>	<b>15</b>
3.1	Compressible or Incompressible Flow Relations . . . . .	16
3.2	General Modeling Assumptions and Approaches . . . . .	18
3.3	Modeling of the Inlet Nozzle and the Exhaust Nozzle . . . . .	20
3.4	Modeling of the Impeller and Diffuser . . . . .	22
3.5	Modeling the Combustion Chamber . . . . .	29
3.6	Modeling of the Axial Turbine . . . . .	34
<b>4</b>	<b>Modeling Evaluation and Validation</b>	<b>39</b>
4.1	The Inlet Nozzle . . . . .	39
4.2	The Compressor Results . . . . .	41
4.3	The Combustion Chamber . . . . .	44
4.4	The Turbine Results . . . . .	45
4.5	The Exhaust Nozzle Results . . . . .	47
4.6	General System Results . . . . .	50
<b>5</b>	<b>Conclusion</b>	<b>57</b>
5.1	Future Work . . . . .	59
	<b>Bibliography</b>	<b>61</b>
	<b>Appendix</b>	<b>61</b>
<b>A</b>	<b>The Modeling</b>	<b>65</b>
<b>B</b>	<b>Test Run of the SR-30 Engine</b>	<b>79</b>
<b>C</b>	<b>Combustion Calculations by CEA NASA</b>	<b>83</b>
<b>D</b>	<b>Determining the Excess Air Ratio using the Inlet Mass Flow</b>	<b>87</b>
<b>E</b>	<b>Estimating the Oxygen Content in the Exhaust Pipe</b>	<b>91</b>
<b>F</b>	<b>CD Content</b>	<b>95</b>



# Biofuel in Aviation Requires Modeling

# 1

Commercial aviation is mainly sourced by fossil fuels and currently constitutes 2 - 2.5 % of the global carbon dioxide emissions by emitting more than 677 million tonnes per year (Ph. Novelli, 2011) (ATAG, 2009). As with all other energy consuming industries, the possibility of substituting the fossil fuels by alternatives are of high interest from both an environmental and economic point of view.

Interest groups, such as CAAFI and SWAFEA, are formed with the purpose of accelerating the development and commercialisation of aviation biofuels. Implementation of new technologies such as fuel cells or batteries are possible, but practically very limited and as a result the possibility is not considered by these interest groups (Ph. Novelli, 2011). The environmental and economical benefits of changing the fuel rather than the technology are extremely significant, as a change of fuel most probably also will be compatible with existing aircrafts.

According to CAAFI's roadmap for their future milestones, the first steps of combining biofuels and aviation are component and engine testing rather than flight testing (CAAFI, 2007). To succeed with this first step, a validated model of a turbojet engine is required in order to analyse the consequences of varying different parameters in that particular engine. Obviously the aviation industry applies a range of different turbojet engines. The ability of modeling a particular engine just by the use of engine dimensions is however inspiring, as this enables modeling of various turbojet engines. Furthermore, validation is a necessity to any model for it to be useful, and in the case of flight testing, the importance of reducing the margin of error is crucial. This defines the scope of this report.

## 1.1 Problem Statement

The motivational arguments for implementing different biofuels in aviation are numerous. As mentioned, technologies are however still limited and as a result the first intermediate steps are fuel and engine testing rather than flight testing. To obtain enough knowledge for performing high gain tests, a detailed model of the particular engine is required. This formulates the hypothesis and aim of this report:

*A validated model of the SR-30 turbo jet engine is to be made in order to predict the performance of the engine with high accuracy*

The SR-30 turbojet engine is a small scale laboratory gas turbine mounted in a test stand with the purpose of experiments only. Accurate drawings of the engine has been provided by the manufacturer, *Turbine Technologies*, which forms the major basis for the model. Firstly, the design of the engine will be analysed and considered prior to engine modeling. Secondly, the modeling approach will be presented in details. Finally, test-runs are performed on the SR-30 engine and the measured values are compared with the modeling predictions in order to validate the model.



# Premodeling Considerations 2

The purpose of this chapter is to present considerations made prior to modeling the SR-30 turbojet engine. Relevant dimensions are presented and related to theory that describes the choice of design. In addition, the manufacturer may have compromised with the design optimum in order to ensure a wider range of performance or flow stability. This may result in losses, which is also discussed in the following sections.

The SR-30 turbojet engine is a laboratory scale engine composed by an inlet nozzle, a single stage centrifugal compressor, an annular combustor, a single stage axial flow turbine and an outlet nozzle. The components are displayed in figure 2.1. At first, the air is accelerated in the inlet nozzle, then compressed in the compressor. Next, the air is mixed with fuel in the combustion chamber. Hereafter, a flue gas under high pressure and temperature enters the turbine, which extracts power from the flow to drive the compressor. Finally, the gas expands in the exhaust nozzle and leaves at a high velocity, creating thrust.

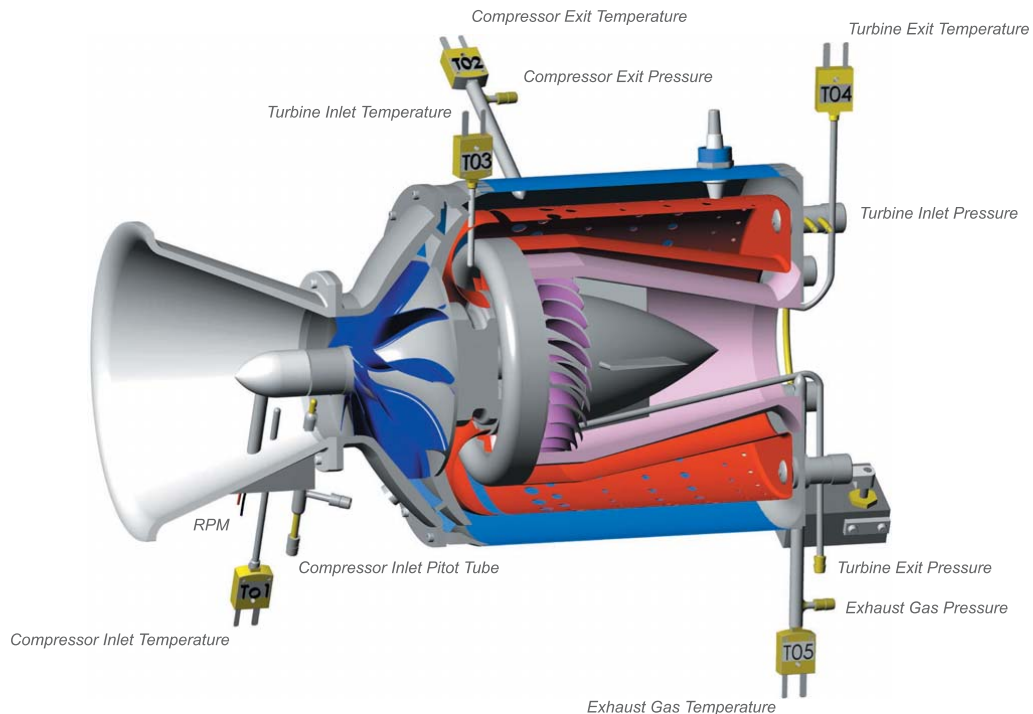


Figure 2.1. Computer rendered model of the SR-30 turbojet engine. (Turbine Technologies, 2012)

Figure 2.1 is a computer rendered model of the SR-30 jet engine. It appears that the test engine is equipped with several temperature and pressure sensors. These are used to validate the model that will be the product of this project.

The SR-30 engine operates with liquid fuels, such as kerosene based or diesel blended fuels. Table 2.1 lists some general specifications of the engine delivered by the manufacturer. These specifications are rounded numbers, and therefore considered inaccurate. However, they reveal the size of the engine and they have been used as indicators throughout the project.

Manufacturer:	Turbine Technologies, Ltd.
Model Number:	SR-30
Max. RPM:	87,000
Max. Thrust	40 lb. ( $\approx 180$ N)
Max. Exhaust Gas Temperature:	720°C
Mass Flow:	0.5 kg/s
Pressure Ratio:	3.4:1
Specific Fuel Consumption:	1.22 lb./lb.-hr ( $\approx 6$ g/s)

*Table 2.1.* Specifications on the SR-30 turbojet engine delivered by *Turbine Technologies* (2012).

The purpose of the different components in figure 2.1 are presented along with relevant engine dimensions in the following sections.

## 2.1 The Single Stage Centrifugal Compressor

There are two types of compressors. Axial compressors where the flow is parallel to the axis of rotation and radial compressors where the exit flow is turned perpendicular to the axis of rotation. The purpose of the compressor is to raise the pressure of the incoming air before it enters the combustion chamber. The SR-30 jet engine has a single stage radial compressor with one impeller row and one diffuser row. The dynamic pressure is increased through the impeller as the velocity is increased when work is applied to the air by the impeller. Through the diffuser the velocity is reduced and thus the dynamic pressure is converted into static pressure.

From the impulse change of the fluid it can easily be derived that the work  $\dot{w}_{Comp}$  done by the impeller on the fluid is expressed with equation (2.1).  $U$  is the tip speed of the impeller and  $V_\theta$  is the tangential component of the fluid velocity. (Dixon and Hall, 2010)

$$\dot{w}_{Comp} = U_2 \cdot V_{\theta 2} - U_1 \cdot V_{\theta 1} \quad [J/kg] \quad (2.1)$$

Work equals the enthalpy change of the fluid, and from the above it can be derived that the enthalpy change across the impeller can be expressed with equation (2.2). The derivation is rather long, but is based on the fact that  $\bar{W} = \bar{V} - \bar{U}$ , where  $\bar{W}$  is the relative velocity vector.

$$h_2 - h_1 = 1/2 (U_2^2 - U_1^2) + 1/2 (W_1^2 - W_2^2) \quad [J/kg] \quad (2.2)$$

The second expression,  $1/2 (W_1^2 - W_2^2)$ , on the right-hand side of equation (2.2) is the contribution from the relative velocity, which is present in both axial and radial compressors, while the first term,  $1/2 (U_2^2 - U_1^2)$ , is only present in radial compressors as it relates to the change in radius. The enthalpy is related to the pressure and thus a higher enthalpy change in the radial compressor causes a higher pressure ratio than in the axial compressor. This is consistent with the statement of radial compressors being able to obtain a pressure ratio of more than 4, while axial compressors need several stages in order to do the same. (Dixon and Hall, 2010)

### 2.1.1 Impeller and Diffuser Dimensions

This subsection presents the dimensions of the impeller and diffuser of the centrifugal compressor. Figure 2.2 presents the measurements of the impeller.

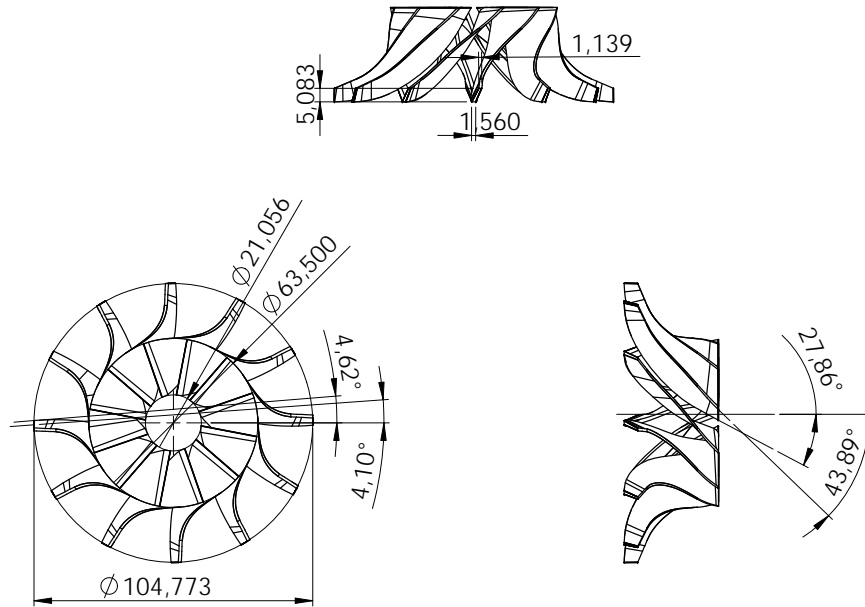


Figure 2.2. Measurements of the impeller drawings. Lengths are given in mm.

The inlet area is measured perpendicular to the axial velocity component and the outlet area is measured perpendicular to the radial velocity component. Blade thicknesses are neglected at inlet of the impeller, but included at the outlet. The areas and angles are listed in table 2.2.

Figure 2.3 presents the measurements of the diffuser.

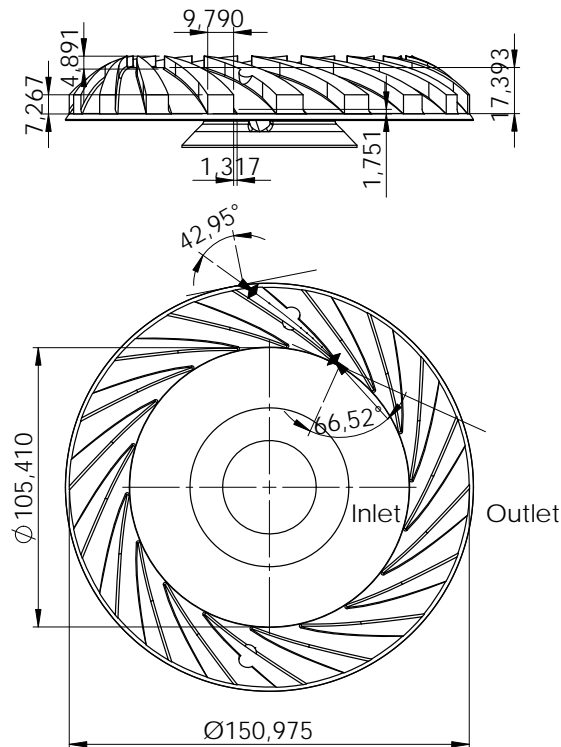


Figure 2.3. Measurements of the diffuser drawings. Lengths are given in mm.

The areas are measured perpendicular to the radial velocity component. Notice that the blade area is neglected at the diffuser inlet as the tips have an aerodynamic shape and are very thin. Blade thicknesses are included at the outlet since the shape has thickened at this point and occupies more area. The areas and the blade angles are listed in table 2.2.  $\alpha$  is the angle between the absolute velocity and either axial or radial direction, whereas  $\beta$  represents the angle between the relative velocity and either axial or radial direction. Some angles are not listed, as they depend on the axial speed which varies.

Compressor	Area [m <sup>2</sup> ]	$\alpha$ [°]	$\beta$ [°]
Impeller inlet	0.0055	-	35
Impeller outlet	0.0016	-	4
Diffuser inlet	0.0016	67	-
Diffuser outlet	0.0021	43	-

Table 2.2. Areas and angles calculated from the drawings.

### 2.1.2 Impeller Design

The impeller is unshrouded in the SR-30 engine which means that the flow channels are not closed by the impeller design itself, but by a stationary housing in which the impeller is mounted. This is known to degrade the performance compared to a shrouded impeller due to the small gap between housing and impeller. Figure 2.4 displays the difference between a shrouded and unshrouded impeller. (Cumsty, 2004)



Figure 2.4. Impellers with and without shrouding. (Bridgat, 2012)

A shrouded impeller is often used for industrial purposes and when several compressor stages are needed, but it tends to complicate design and greatly increase mass. Greater mass means by definition larger stress due to tip speed, though the shroud would increase the strength of the impeller. A steel impeller for an industrial compressor, for example, at maximum tip speed of 380-430  $m/s$  would be acceptable with an unshrouded impeller, but that speed would not be possible for the shrouded impeller due to the high mass. This explains the manufacturers choice of an unshrouded impeller in the SR-30 engine. (Cumsty, 2004)

The impeller in the SR-30 jet engine has an inducer in order to maximise performance. The inducer is in the inlet of the compressor, where the flow mainly has an axial direction. The inducer raises the static pressure before the fluid experiences the curvature of the shroud, but the main advantage is that it gives a larger throat area than an impeller without inducer. This enables a higher mass flow compared to a compressor of same size without inducer. Impellers without inducers are often used in industrial purposes where multi stage compressors are used. Here the inducer will contribute to a longer compressor, which may cause practical complications. (Cumsty, 2004)

The impeller in the SR-30 engine has backswept blades at the impeller outlet, meaning that the tangential component of the relative flow leaving the impeller is increased. This appears from figure 2.5 that sketches the effect of backswept blades with respect to velocity triangles. Backswept blades improves stability, however, at the expense of work since the tangential component of the absolute flow is decreased (Dixon and Hall, 2010).

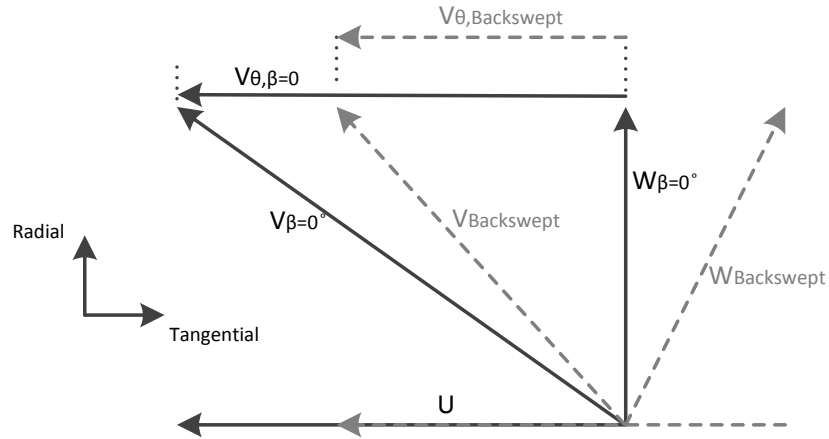


Figure 2.5. The tangential component of the absolute velocity is decreased when using backswept blades.

The manufacturer of the SR-30 engine has chosen backswept blades with a small angle of  $4^\circ$  and because the angle is so small it is difficult to point out the argument for using backswept blades.

### 2.1.3 Diffuser Design

The air flow exits the impeller with a high velocity and the purpose of the diffuser is to convert the dynamic pressure into static pressure. *Dixon and Hall (2010)* uses the term diffusion to describe the deceleration and compression of the fluid, which arises in a diffuser. This term is used throughout this report. Diffusion is done by increasing the cross sectional flow area in the flow direction. The diffuser geometry seems to be relatively simple, but there are two very important aspects of its appearance. One, is the tendency of the boundary layer to separate from the walls if the local rate of diffusion becomes too big. The other occurs if the diffusion rate becomes too small, and the flow is exposed to a long channel where friction between wall and fluid becomes significant. In other words, the design optimum depends on the diffusion angle, which is the angle between the flow direction and the diffuser blades. According to *Dixon and Hall (2010)* the optimum diffusion angle is between  $8-10^\circ$ . Figure 2.6 illustrates measurements of the diffusion angle for the SR-30 diffuser. The measurements are made at the location where the rate of diffusion is considered largest. It is the angle between the meridional flow direction and the channel wall which is relevant, thus the angle of diffusion is  $5.2^\circ$ . Compared to an optimum angle of  $8-10^\circ$  it seems that the diffusion rate could be increased in the SR-30 diffuser and thereby the compressor could be designed more compact and friction in the blade row could be reduced.

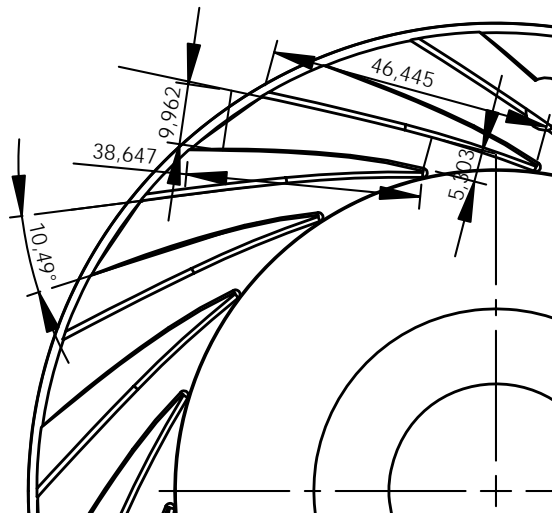


Figure 2.6. Measurements of diffusion angle and L/W ratio of the SR-30 diffuser.

According to *Dixon and Hall (2010)* experiments done by Clements and Artt (1998) indicated that an optimum between length and width of the diffuser vanes exists. They concluded that increasing L/W (length and width ratio) above 3.7 did not improve the performance of the diffuser. From the measurements illustrated in figure 2.6, it is calculated that the SR-30 jet engine has a L/W ratio of more than 5.5. The measurements are approximate and the calculation is based on mean values of channel length and width. According to Clements and Artt the SR-30 diffuser could be optimised in size by reducing the vane length in order to reduce the L/W ratio. This would not affect the performance, and it complies with the suggestion presented above about increasing the angle of diffusion.

Diffusers also come without vanes, but these are most often used in industry where size is of secondary importance compared to manufacturing costs. The vaned diffuser is clearly advantageous where a small unit is required, which has probably been the argument when choosing a vaned diffuser for the SR-30 engine. Furthermore, the peak efficiency may be higher for vaned diffusers compared to vaneless ones, but the range of mass flow at a given speed is reduced by the risk of stall in the diffuser vanes. (Ferguson, 1963)

According to both *Ferguson (1963)* and *Dixon and Hall (2010)* it is standard practice to design a compressor such that the diffuser has less blades than the impeller. The reason is to ensure an even distribution of the flow entering the diffuser. This is however inconsistent with the SR-30 compressor design, where the impeller has 12 blades and the diffuser has 18. This might result in an uneven flow distribution, where stall can occur in some of the diffuser channels.

In a vaned diffuser, there is a small clearance between the impeller blades and the diffuser vanes. This gap corresponds to a vaneless diffuser and its purpose is to smooth out velocity variations between impeller tip and diffuser vanes. However it seems to be a good approximation to neglect this gap (*Cumsty, 2004*). From equation (2.3), describing the meridional velocity in a vaneless diffuser based on a mass balance, it is seen that with no change in flow area there is no change in meridional velocity.

$$V_2 = \frac{A_1 \rho_1 V_1}{A_2 \rho_2} \quad [m/s] \quad (2.3)$$

$A_1$ ,  $A_2$ ,  $V_1$  and  $V_2$  is the area and the velocity at the impeller outlet and diffuser inlet respectively and therefore the density can be assumed constant. In addition to this, notice from table 2.2 how the outlet area of the impeller is designed to equal the inlet area of the diffuser. The ratio between the area at impeller outlet and diffuser inlet is 0.993, which means that there is a minor increase in the cross sectional area from impeller to diffuser. Thus the gap has the effect of a vaneless diffuser without eliminating the wish of having a smooth expansion of the flow. When evaluating the diameters given in figure 2.3 the particular gap is 0.32 mm in the SR-30 compressor.

## 2.2 Considerations Related to the Combustion

The combustion in a jet engine is a reaction between fuel and oxygen. Dry air consists of 20.9 % oxygen, 78.1 % nitrogen, 0.9 % argon and small amounts of carbon dioxide, helium, neon and hydrogen. The argon is treated as nitrogen and air humidity is neglected along with the small amounts of carbon dioxide, helium, neon and hydrogen. Thus, air is approximated to consist of 21 % oxygen and 79 % nitrogen by volume. (*Cengel and Boles, 2007*)

By investigation of the mole fraction of moisture in atmospheric air, it can be determined whether it is a good assumption to neglect the water content. The conditions, at which the jet engine is tested, are 14°C, atmospheric pressure and a relative humidity of 30 %. Evaluating the mole fraction of water in humid air reveals a fraction of less than  $10^{-5}$ . Thus, it is an acceptable assumption to neglect air humidity.

The combustion products consists of carbon dioxide, water, nitrogen and excess air along with small amounts of e.g. N, NO<sub>2</sub> and OH. These small amounts are neglected since the mole fraction of these products are found in appendix C to be less than 5 ppm.

The combustion process can occur when the air fuel mixture is above its ignition temperature and a proper amount of oxygen is present in the chamber. However, excess air is added in order to ensure a reaction as complete as possible. Secondly, excess air lowers the adiabatic flame temperature and thereby decreases the rate of dissociation. Finally, by reducing the temperature out of the combustion chamber the material requirements of the turbojet engine are reduced. (*Turns, 2000*)

The amount of excess air can be related to the air fuel ratio, AF, given in equation (2.4). (*Turns, 2000*)

$$AF = \frac{\dot{m}_{air}}{\dot{m}_{fuel}} \quad [\cdot] \quad (2.4)$$

The mass flow of air and the fuel consumption is given in table 2.1 listing the general specifications of the SR-30 engine. These mass flows are probably evaluated at the maximum speed of 87,000 RPM. If this is correct the AF ratio is 83 at this speed. However, the AF ratio will change with RPM and there is no specifications about this variation. In order to obtain such, experiments measuring the mass flow of air and fuel consumption as a function of RPM, have been performed. The experiment and the results are presented in section 3.5.

### 2.3 The Single Stage Axial Turbine

As with compressors, the flow can either leave a turbine in a radial or axial direction. A radial turbine will only be used in a case where compactness is the primary consideration and performance is of secondary importance. Axial flow turbines are always used in jet turbines, which is also the case for the SR-30 engine. The turbine used in this particular engine is a single stage turbine and thus it is not designed with a geometry that ensures that the axial component of the flow velocity at outlet of the stage equals that of the inlet. For multistage turbines this is standard procedure in order to simplify the design, but there is no need for this simplification as the SR-30 turbine consists of one stage only. Based on this, it is expected that the manufacturer has designed the turbine with other considerations in mind, for instance performance over simplicity. The dimensions of the stator and rotor of the SR-30 turbine appears in figure 2.7 and 2.8 respectively. (Dixon and Hall, 2010)

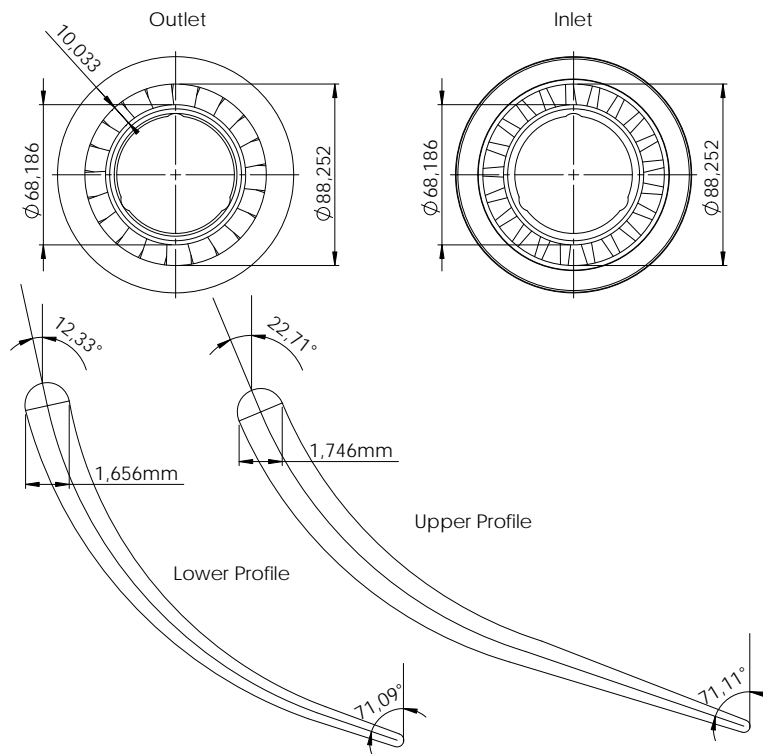


Figure 2.7. Measurements of the stator drawings. Both upper and lower blade profiles are drawn to consider that the blade is twisted. Lengths are given in mm.

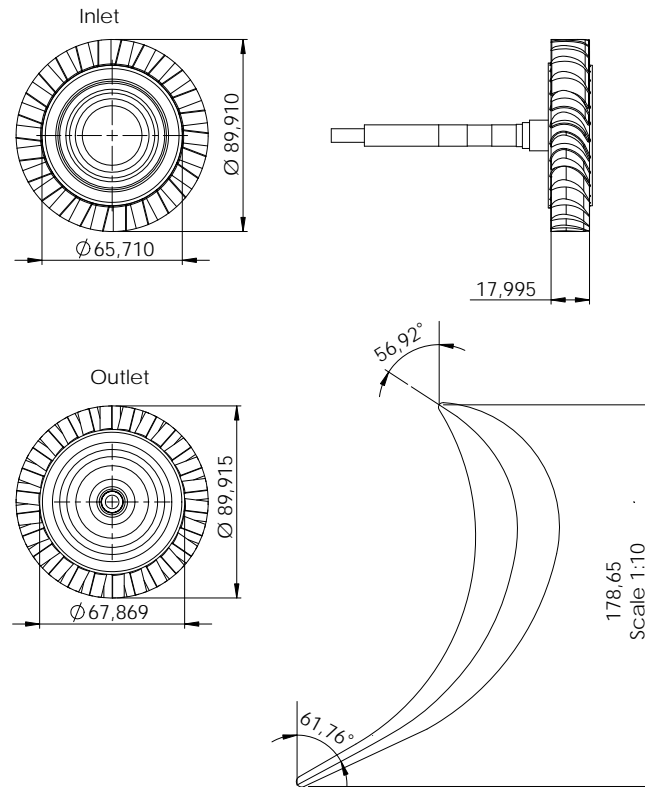


Figure 2.8. Measurements of the rotor drawings. Lengths are given in mm.

It appears from the drawings how all areas are measured perpendicular to the axial direction for both the stator and rotor part. Notice also that all blade areas are neglected due to aerodynamic blade designs. The areas and the blade angles are listed in table 2.3. Some angles are not listed, as they depend on the axial speed.

Turbine	Area [m <sup>2</sup> ]	$\alpha$ [°]	$\beta$ [°]
Stator inlet	0.0025	18	-
Stator outlet	0.0025	71	-
Rotor inlet	0.0025	-	62
Rotor outlet	0.0024	-	62

Table 2.3. Areas and angles calculated from the drawings of the SR-30 turbine.

The stator blades are twisted and it is assumed to be accurate to calculate  $\alpha$  at stator in- and outlet as mean values of the angles given at upper and lower blade profiles in figure 2.7.

The general purpose of the turbine is to drive the compressor through a shaft. As with the compressor, the turbine consists of a rotor row and a stator row, but in the turbine the stator is placed before the rotor. A main consideration when designing the turbine stage is to avoid deceleration of the fluid throughout the blade rows of the stator and rotor. According to *Dixon and Hall (2010)* this is very important, since diffusion within the blade rows will cause flow separation and large scale losses. Furthermore, the acceleration of the fluid in a turbine enables a high blade loading compared to that of a compressor without the risk of boundary layer separation. On top of that, if diffusion is avoided a turbine can operate efficiently under a large variation of mass flows. This is not the case for a compressor, which along with a higher blade loading, explains why one turbine stage is able to drive several compressor stages. (*Dixon and Hall, 2010*)

The areas given in table 2.3 appear to be rather constant, although with a slight decrease at outlet of the rotor. From figure 2.7 it is seen how the blade angle,  $\alpha$ , increases throughout the blade row of the stator, which ensures an acceleration of the fluid. This acceleration affects density in such a way that diffusion is definitely avoided in the turbine stator. With respect to the turbine rotor it appears from figure 2.8 that the blade angle,  $\beta$ , decreases from  $56^\circ$  in one direction to  $62^\circ$  in the opposite direction. Notice, it is the relative velocity,  $\overline{W}$ , which is following the blades in a rotating blade row, and therefore it is the relative velocity that should not be decelerated. If the flow area of the blade row is kept constant when the angle goes from  $56^\circ$  to  $0^\circ$ , such a bending would cause deceleration of the fluid. This is because the axial velocity component is defined from the conservation of mass flow and thus the relative velocity decreases with a decreasing angle. However, it appears from figure 2.8 that the flow area is decreased when the blade angle goes from  $62^\circ$  to  $0^\circ$  by thickening the blade. Thereby, it seems that the manufacturer attempts to avoid deceleration by compensating for a decreasing blade angle through a reduction in flow area. At inlet  $\overline{W}$  has the same direction as the tip speed  $\overline{U}$ , whereas they have opposite directions at outlet due to the change in the angle  $\beta$ . As the absolute velocity  $\overline{V}$  is defined as  $\overline{V} = \overline{W} + \overline{U}$ , the fact that  $\overline{W}$  and  $\overline{U}$  have opposite directions at outlet may then result in diffusion of the absolute velocity,  $\overline{V}$ . This depends on the pressure drop across the blade row, which is analysed further in the modeling results in chapter 4.

The above given discussion about how the rotor dimensions affect the change of velocity relates highly to the degree of reaction, which is described in the following.

### Degree of Reaction

The degree of reaction,  $R$ , is an indicator of the increase of relative flow velocity across the rotor part of an axial turbine. For an axial turbine, the degree of reaction can be defined as the ratio of the static enthalpy change in the rotor part to the static enthalpy change in the whole turbine stage. This is expressed by equation (2.5). (Dixon and Hall, 2010)

$$R = \frac{h_2 - h_3}{h_1 - h_3} \quad [\cdot] \quad (2.5)$$

By derivation equation (2.5) can be changed into (2.6).

$$R = \frac{1/2 \cdot (U_2^2 - U_3^2) + 1/2 \cdot (W_3^2 - W_2^2)}{(h_{01} - h_{03}) + 1/2 \cdot ((W_3 + U_3)^2 - (W_1 + U_1)^2)} \quad [\cdot] \quad (2.6)$$

In the SR-30 jet engine the radii at in- and outlet of the rotor are very similar, which means that the blade speed,  $U$ , can be assumed constant. Thereby, it appears from equation (2.6) how the reaction stage mainly depends on relative velocities for axial turbines. Since the degree of reaction depends on relative velocity, it is related with the shape of the rotor blades. As shown with figure 2.9, the velocity triangles change with the shape of the blade and so does the degree of reaction. Subscript 1 represents the outlet of the stator part and subscript 2 the outlet of the rotor part.

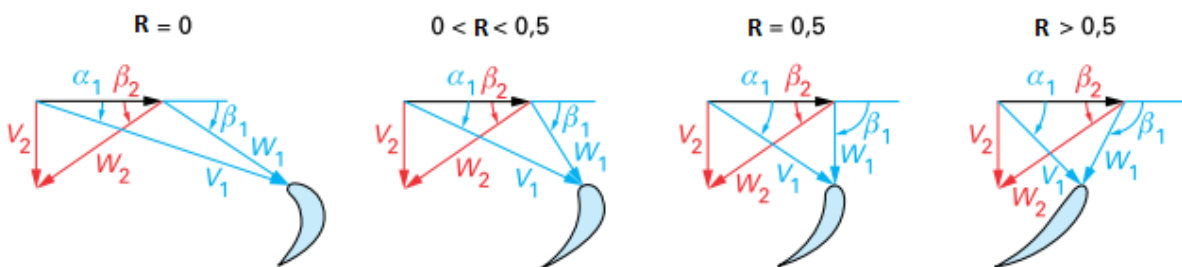


Figure 2.9. Velocity triangle for different reaction degrees. Modified from Paul (1998).

The blade dimensions of the SR-30 turbine rotor have the most in common with the velocity triangle with zero reaction to the left in figure 2.9. Evaluated with equation (2.5) a zero reaction reveals that all enthalpy change occur in the stator.

A zero reaction stage can be related to an impulse turbine for which the rotor and stator shapes differ. This is also the case for the SR-30 turbine, which appears from the drawings presented earlier in this section. However, an impulse turbine is by definition characterised by no pressure drop across the rotor, which is not the case for a zero reaction turbine. The advantages of a zero reaction stage are that a high loading is possible, there is low pressure force tending to move the wheel in the axial direction, the gas does not tend to leak over the tips of the blade row and the thrust on the rotor is lower. However, a low reaction degree can create a boundary layer separation and when increasing the stage loading, the efficiency tends to decrease. Concluding, turbines are most often designed with a low reaction degree when it is important to have a low number of stages. This could very likely be the critical argument when the type of turbine was chosen for the SR-30 engine. (Dixon and Hall, 2010)

When the degree of reaction is equal to unity, the turbine is a purely reaction turbine, but commonly the degree of reaction used in reaction turbines is 50 %. In this case, the enthalpy drop in the stator part equals that of the rotor part. Furthermore, 50 % reaction stages are characterised by symmetrical rotor and stator blades and an inlet area bigger than the outlet area. (Dixon and Hall, 2010)

The degree of reaction is calculated as a result of the turbine modeling and compared to the hypothesis of a low degree of reaction. It is expected that  $R$  is low, but not zero as the flow in reality will not leave the blade rows at an angle perfectly parallel with the blades.

## 2.4 Nozzles at Subsonic Flows

In the SR-30 jet engine a nozzle is used to increase the velocity of the fluid both entering and leaving the SR-30 engine. The velocity of the fluid leaving the engine is increased in order to get the highest possible thrust since thrust is proportional to the velocity difference from exhaust to free stream velocity. The cross sectional area of the exit nozzle is decreasing with the flow direction and thus it is a converging nozzle where the velocity increase is limited to a sonic velocity with a maximum Mach number of 1. The flow is considered isentropic through the nozzle and thus the relation between pressure change and area change can be described by equation (2.7). (Cengel and Boles, 2007)

$$\frac{dA}{A} = \frac{dP}{\rho \cdot V^2} (1 - Ma^2) \quad [.] \quad (2.7)$$

For a subsonic flow where the Mach number is less than one, the term  $(1 - Ma^2)$  in the equation is positive and because  $\rho$ ,  $V$  and  $A$  are positive parameters the area change,  $dA$ , and pressure change,  $dP$ , must have equal signs. That is, the pressure distribution decreases along the nozzle because of the decreasing area of the converging nozzle. (Cengel and Boles, 2007)

From equation (2.7) it can also be seen that no pressure change in a diverging nozzle must equal zero velocity and thereby zero mass flow. Furthermore, a larger pressure difference results in increasing velocity. The velocity increase reaches a maximum at the nozzle throat. The nozzle is said to be choked if the pressure decrease yields a sonic exit velocity equal to the speed of sound. When the nozzle is said to be choked the maximum mass flow rate is reached and a further pressure decrease has no influence on the mass flow rate or velocity. (W.Bathie, 1984)

To exceed a Mach number of 1 a converging nozzle must be extended by a diverging nozzle. The two types of nozzles are displayed in figure 2.10.

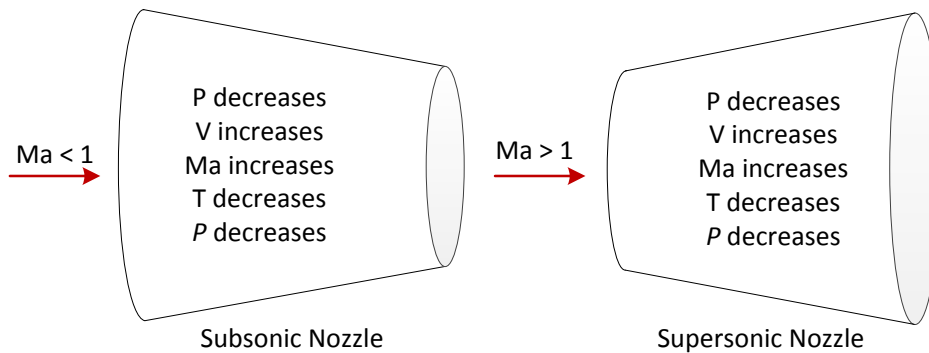


*Figure 2.10.* Converging and diverging nozzles with Mach number below and above unity. Modified from *Cengel and Boles (2007)*.

In the converging part, the velocity is increased until reaching the velocity of sound. Once a Mach number of unity is reached, an increasing cross sectional area is needed for the gas to expand in order to obtain even higher Mach numbers. This can also be derived from equation (2.7). For turbojet engines such as the SR-30 engine it is crucial not to have supersonic flows, since the flow behavior becomes very complicated. (Condra, 2012)

The nozzle exit pressure equals the free stream pressure at subsonic flows. For supersonic flows the backpressure may go below or very much above ambient without flow separation due to the high jet velocity. (Dixon and Hall, 2010)

The purpose of this chapter was to present the SR-30 turbojet engine with respect to dimensions and considerations relevant prior to modeling the engine. In the following chapter the modeling approach is presented.

# Modeling of the SR-30 Turbojet Engine 3

The purpose of this chapter is to describe how each component of the SR-30 turbojet engine is modeled. Firstly, the premises for choosing compressible flow conditions instead of incompressible are presented. Secondly, general formulas, applicable for compressible flows are listed, and the use of these in the modeling is explained. The modeling is made in Matlab using a mainfile to implement different submodels. These submodels are from now on referred to as the inlet, impeller, diffuser, combustion, turbine stator, turbine rotor and nozzle model respectively. In the mainfile a submodel determining the inlet mass flow is also included. This model is based on test results determining the inlet mass flow and the fuel consumption as a function of RPM. The Matlab models can be found in appendix A and the test determining the inlet mass flow is described in appendix D. Figure 3.1 illustrates a schematic of how the different submodels interact. The numbers given in the figure are used as subscripts throughout the rest of the report, when referring parameters to different stages of the engine.

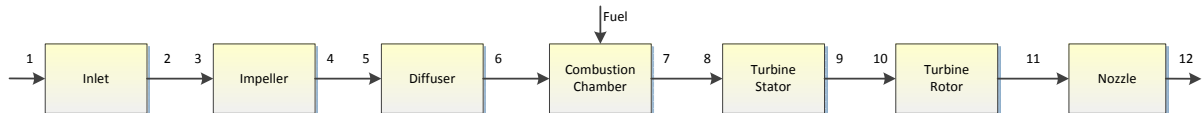


*Figure 3.1.* Schematic of the SR-30 turbojet engine model with the notation applied in the model.

Thermodynamic properties such as density, enthalpy, speed of sound, specific heat values and molar masses are taken from REFPROP, which is a software that contains NIST databases and easily interacts with Matlab. Density for a particular fluid depends for instance on temperature and pressure and thus these parameters are inputs to REFPROP. For thermodynamic properties it is avoided to use other databases than REFPROP in the modeling in order to ensure that data, such as enthalpies are based on the same reference point. The fluid is assumed to be air throughout the modeling and thus the flue gas from the combustion chamber is assumed to be air as well. The REFPROP software is included in appendix F, since it is required to run the modeling.

### 3.1 Compressible or Incompressible Flow Relations

Throughout the modeling of the turbojet engine, it must be decided whether to use compressible or incompressible flow relations. This section compares the differences of modeling the inlet nozzle considering the air as either incompressible or compressible. In many applications incompressible conditions are chosen as the density is constant, which simplifies the modeling. As a general approach compressible conditions are chosen if the Mach number exceeds 0.3 (Munson et al., 2006).

To compare the flow conditions in the nozzle, the output parameters are determined when knowing the inlet parameters. The outlet parameters determined are flow velocity, Mach number, static pressure, temperature and density. The density is constant in the case of incompressible flow whereas REFPROP is used to determine the density as a function of temperature and pressure in the compressible case.

Equations (3.1) and (3.2) are used as general equations to determine the velocity and Mach number for both compressible and incompressible flow conditions. In this particular analysis the mass flow is assumed to be  $0.5 \text{ m/s}$  based on the data given by *Turbine Technologies*.  $R_s$  is the specific gas constant.

$$V = \frac{\dot{m}}{\rho \cdot A} \quad [m/s] \quad (3.1)$$

$$Ma = \frac{V}{c} = \frac{V}{\sqrt{\kappa \cdot R_s \cdot T}} \quad [\cdot] \quad (3.2)$$

To determine the outlet temperature and pressure different formulas are applied for compressible and incompressible flow relations. The process that occurs in the nozzle is considered isentropic since no work is done to the air flow and thus the stagnation quantities are constant throughout the nozzle. The fact that the stagnation properties are constant are used when determining the outlet temperature and pressure.

Equation (3.3) is the definition of stagnation temperature which is used in the modeling of the outlet temperature during incompressible conditions. Equation (3.4) is Bernoulli's incompressible flow equation where no elevation is considered. (Cengel and Boles, 2007)

$$T + \frac{V^2}{2 \cdot C_p} = T_0 \quad [K] \quad (3.3)$$

$$P + \rho \cdot \frac{V^2}{2} = \text{constant} \quad [kPa] \quad (3.4)$$

Equations (3.5) and (3.6) are relations applicable for compressible flows where the stagnation properties are expressed in terms of the Mach number and the specific heat ratio,  $\kappa$ . (Cengel and Boles, 2007)

$$\left(1 + \frac{\kappa - 1}{2} \text{Ma}^2\right) T = T_0 \quad [K] \quad (3.5)$$

$$\left(1 + \frac{\kappa - 1}{2} \text{Ma}^2\right)^{\frac{\kappa}{\kappa - 1}} P = P_0 \quad [kPa] \quad (3.6)$$

Since the stagnation properties are constant throughout the nozzle the inlet conditions can be used to determine the outlet parameters.

The static quantities are a function of  $C_p$  or Mach number, while  $C_p$  and Mach number are functions of density, temperature and pressure. This indicates that the model cannot be evaluated directly since all parameters depend on each other and thus iterations must be used to solve the problem. The iteration method used throughout the modeling will be presented in details in subsection 3.2.2.

Figure 3.2 shows how the velocity increases through the nozzle as the area ratio increases. Compressible flow conditions reveals a higher velocity increase with area ratio than the incompressible flow conditions. The Mach number is proportional to the velocity and thus the Mach number increase as a function of area ratio is higher for compressible conditions as well.

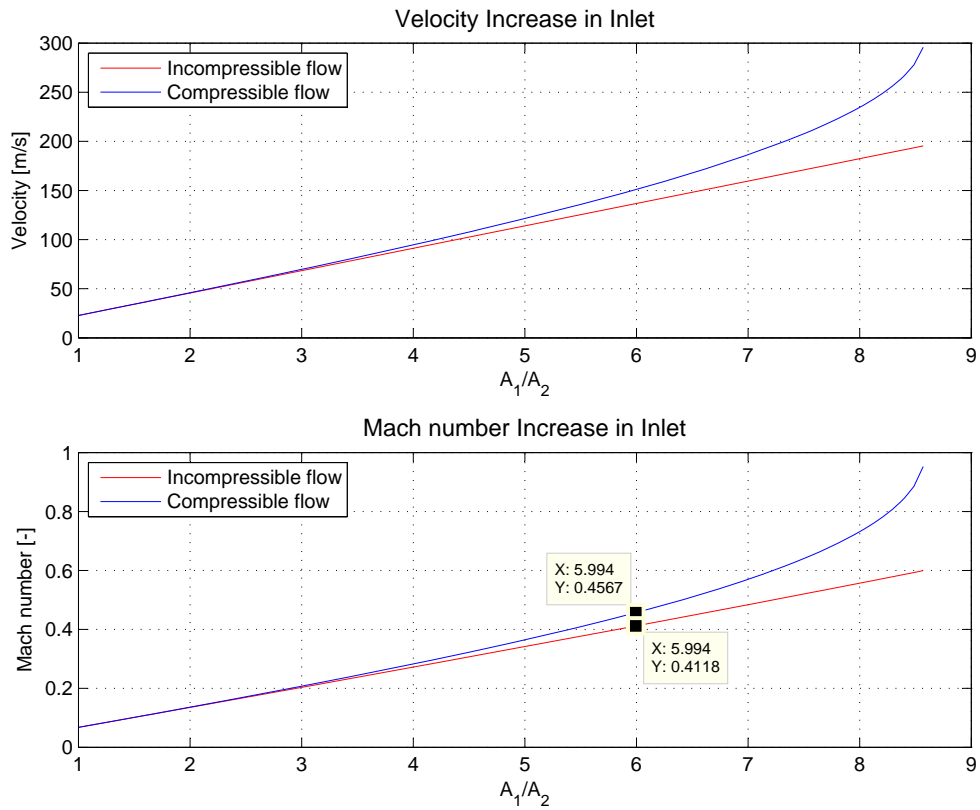


Figure 3.2. The results from the modeling of the inlet nozzle comparing compressible and incompressible flow conditions.

The inlet nozzle in the turbojet engine has an area ratio between in- and outlet of 6. The Mach number at this ratio is illustrated in figure 3.2. The velocity and Mach number do not differ very much between the two cases at the particular area ratio. However, the Mach number is above 0.3 in both cases, which can be used as an argument for choosing compressible flow conditions.

Figure 3.3 illustrates the density related to Mach number for incompressible and compressible flows. It is obvious from the figure how the density decreases as Mach number increases for the compressible case. The actual Mach number with the specific area ratio was found in figure 3.2 and figure 3.3 illustrates the densities corresponding to the determined Mach numbers.

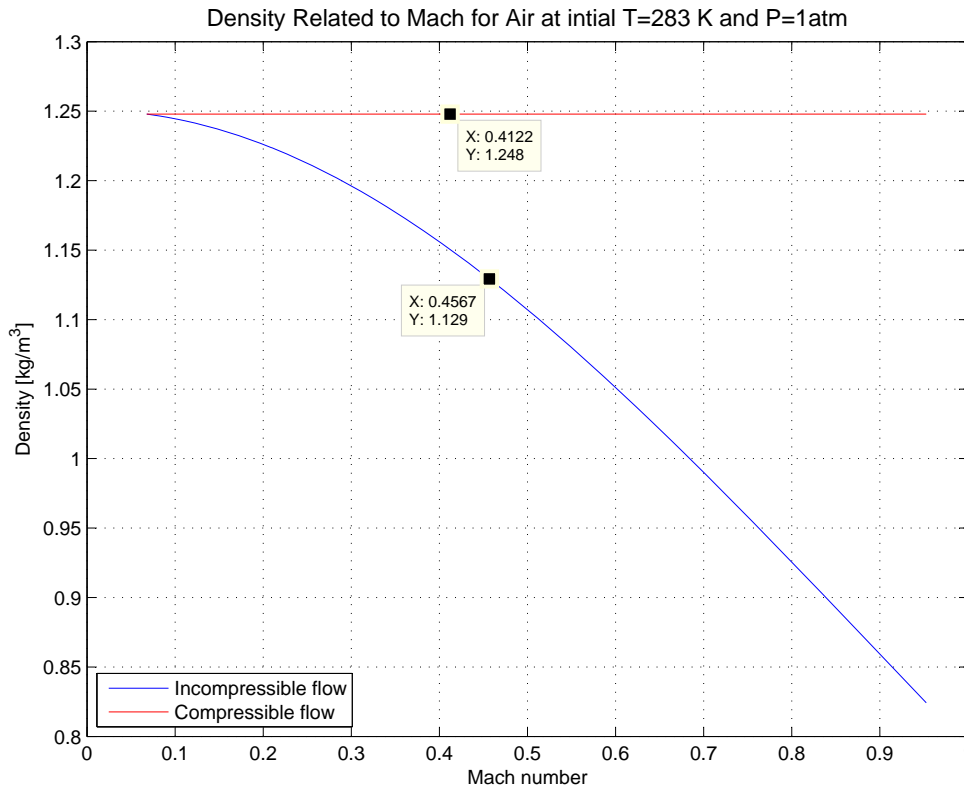


Figure 3.3. Density related to Mach number for incompressible and compressible air flow. The data points correspond to Mach numbers for the nozzle flow considered as incompressible and compressible respectively at an area ratio of 6.

For the specific area ratio the density for incompressible flow is 10 % higher than the density used for compressible flows. The variation between the two ways of considering the flow will be more significant, when higher Mach numbers are reached in for example the compressor. Because of the density deviation and the general approach that compressibility should be considered for Mach numbers above 0.3 it is chosen to work with compressible flow relations throughout the report.

### 3.2 General Modeling Assumptions and Approaches

Stagnation and static quantities at different locations can be related to the local Mach number. The local Mach number can be calculated by equation (3.2), where the nominator represents the absolute flow velocity, which can be calculated from equation (3.1) with a cross sectional area perpendicular to the flow. The denominator of equation (3.2) represents the speed of sound at a particular state, which as previously mentioned is calculated using REFPROP throughout the modeling.

If no shaft work is done to an isentropic flow, the stagnation properties are constant. More precisely the flow must be adiabatic to ensure constant stagnation temperature along a streamline, whereas it must be isentropic to ensure constant stagnation pressure (Hughes and Brighton, 1991). This is considered to be the case for the in- and outlet nozzle. The remaining components in the SR-30 model include losses and addition or subtraction of work, and thus the formulas used to define stagnation quantities for these components will be stated later.

Equation (3.7) is applicable along a streamline of an isentropic flow (Dixon and Hall, 2010). This relation is used to determine either stagnation temperature or pressure for processes, where the stagnation quantities are not constant.

$$\frac{P_{02}}{P_{01}} = \left( \frac{T_{02}}{T_{01}} \right)^{\frac{\kappa}{\kappa-1}} \quad [\cdot] \quad (3.7)$$

Once the stagnation quantities are determined, the static temperature can be calculated with either equation (3.8) or (3.9). Likewise, the static pressure can be calculated with equation (3.10). (Dixon and Hall, 2010)

$$T = T_0 - \frac{V^2}{2 \cdot C_p} \quad [K] \quad (3.8)$$

$$\frac{T_0}{T} = 1 + \frac{\kappa - 1}{2} Ma^2 \quad [\cdot] \quad (3.9)$$

$$\frac{P_0}{P} = \left( 1 + \frac{\kappa - 1}{2} Ma^2 \right)^{\frac{\kappa}{\kappa-1}} \quad [\cdot] \quad (3.10)$$

Equation (3.8) and (3.9) are derived from the definition of stagnation enthalpy for an ideal gas, whereas equation (3.10) is based on the assumption that the process of going from stagnation to static pressure is isentropic (Dixon and Hall, 2010). Both (3.8) and (3.9) are listed since both are applied in the modeling.

### 3.2.1 Velocity Cascades Assumed to be Suitable

The formulas presented above are used throughout the model to calculate stagnation and static quantities of a particular flow. The equations are all functions of the local Mach number, which depends on the absolute velocity. The absolute velocity is defined differently as its direction and value vary through the turbojet engine. Some relations and notations for velocity vectors are however common for all the submodels.

Most importantly, the modeled performance of the compressor and turbine are based on two dimensional velocity triangles. This simplifies the modeling because velocity triangles can be applied to visualise the relation between absolute, relative and blade velocities as well as blade and flow angles. Velocity cascades provide according to *Dixon and Hall (2010)* good approximations of the performance of axial turbomachines at high hub tip radius ratios. The compressor is however centrifugal rather than axial and the hub tip radius ratios are relatively low for the SR-30 turbojet engine. The boundary layer of for instance the impeller surface will affect the velocity profile of the flow in the impeller more with low blade heights. Furthermore, the assumption of stream lined flow will be even more inaccurate when the component sizes are reduced. More advanced modeling tools do exist for turbomachinery in the SR-30 size range, but it is beyond the scope of this project to use these. Therefore, the modeling problem is reduced to two dimensions and any swirl is neglected. Meanwhile, some losses are implemented in the model, which to some extent may make up for the assumptions about stream lined and isentropic flow conditions.

Throughout the model, the tangential velocity component is the first element of any velocity vector. The second element is then the axial or radial component dependent on which direction is neglected in the velocity triangle. As mentioned previously, equation (3.11) relates the absolute velocity vector,  $\bar{V}$ , to blade speed,  $\bar{U}$ , and the relative velocity vector,  $\bar{W}$  (W.Bathie, 1984).

$$\bar{V} = \bar{U} + \bar{W} \Leftrightarrow \begin{bmatrix} V_\theta \\ V_{Ax} \end{bmatrix} = \begin{bmatrix} U \\ 0 \end{bmatrix} + \begin{bmatrix} W_\theta \\ W_{Ax} \end{bmatrix} \quad [m/s] \quad (3.11)$$

The blade speed,  $\bar{U}$ , at some location depends on the local radius,  $r$ , and is calculated from equation (3.12). This vector is applied for blade speeds throughout the model, where the first entrance is tangential

velocity and the second component is zero radial or axial velocity.

$$\bar{U} = \begin{bmatrix} \frac{RPM \cdot 2\pi}{60} \cdot r \\ 0 \end{bmatrix} \quad [m/s] \quad (3.12)$$

The above given relations are common for all the velocity triangles presented in the following sections.

### 3.2.2 Iteration Method

The major part of the submodels contain one or two iteration loops. Once the number of equations equals the number of unknowns, a while loop is made in the particular submodel. All loops are based on the Gauss Seidel iterative method, which is a method of successive corrections, where the newest value of each variable is used in the next equation as soon as it is calculated. This is done to increase the speed of convergence.

Relative errors are calculated for each variable as the variation of the variables are very different. To give an example, the specific heat ratio does not vary a lot, whereas the variation of pressures that are given in kPa may be relatively high. By calculating relative errors the same tolerance can be used for all variables. Equation (3.13) presents the definition of a relative error,  $E_T$ , where  $T$  represents the variable that is evaluated and  $i$  is the counting subscript. (Kreyszig, 2006)

$$E_T^{(i+1)} = \frac{T^{i+1} - T^i}{T^i} \quad [.] \quad (3.13)$$

All relative errors for one iteration loop are compared and with respect to the absolute values the biggest relative error is then evaluated with the convergence criteria. The convergence criteria for all loops is that the biggest relative error must be less than 0.1 %. This accuracy is very good compared to the uncertainty of for instance the measurements of the component dimensions. However, the model converges within 5 seconds, thus a tolerance of 0.1 % might as well be used.

The errors are calculated for every variable at each iteration step and for each loop an error matrix is saved in order to analyse the convergence and stability of the equation set. This will be discussed further when the modeling results are presented in chapter 4. The velocity triangles, along with the formulas presented in section 3.2, do not provided sufficient information to iterate the model towards a solution. Therefore, the remaining equations specific to the submodels are presented in the following sections.

## 3.3 Modeling of the Inlet Nozzle and the Exhaust Nozzle

The purpose of the inlet nozzle and the exhaust nozzle is to accelerate the incoming air and the flue gas respectively. The incoming air is accelerated before entering the compressor and the flue gas is accelerated in order to gain more thrust. The nozzles are converging nozzles for which the accelerations are limited to sonic exit velocities with a maximum Mach number of unity. This was explained in details in section 2.4.

For both nozzles the flow direction is assumed to be fully axial and as a result the cross sectional areas at in- and outlets are applied in equation (3.1) in order to set up expressions for the absolute velocities at these locations. These areas are measured from the drawings of the SR-30 engine and it may be noticed that the area ratios for the inlet and outlet nozzles are 6 and 1.3 respectively. Furthermore, the general compressible flow relations presented in section 3.2 are applied in the modeling of the two nozzles. With these, it is possible to obtain a solution for the stagnation and static quantities by iterations. Assumptions related to the two nozzles are presented in the following two subsections. Common for both are that friction loss is neglected, thus the processes are considered isentropic.

### 3.3.1 Considerations Related to the Inlet Model

The modeling results will be compared with experimental measurements in order to validate the model as mentioned in the problem statement. However, it must be noticed that the temperature is measured 19.3 mm upstream from the exit of the nozzle and the modeled temperature must be evaluated at this point in order to compare correctly. The rest of the modeled parameters are evaluated at the nozzle exit. The measurements are presented in figure 3.4.

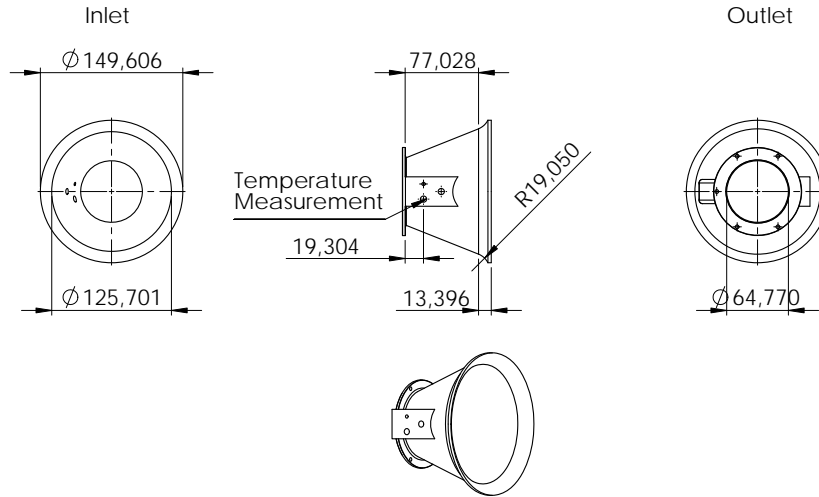


Figure 3.4. Measurements of the inlet nozzle in mm. Notice the temperature measurement is located before the exit.

The exit properties of the inlet model are used at the inlet of the impeller model, and thus the inlet model is also evaluated at the very end of the nozzle. The thermodynamic properties at the inlet of the turbojet engine are set equal to those present at the experiments in order to make a reliable validation. In other words, the static pressure and static temperature at inlet are set equal to 1 atmosphere and 14°C respectively.

### 3.3.2 Considerations Related to the Nozzle Model

The exit nozzle is converging and as previously mentioned the flow will therefore, at most reach a sonic velocity. For subsonic flows the static pressure at outlet of the nozzle equals the ambient pressure (Condra, 2012). A pipe with constant cross sectional area is however mounted at the end of the nozzle to work as a silencer, and thus the location of atmospheric static pressure is moved to the outlet of the silencer. Due to the constant cross sectional area, any pressure loss in the silencer will be caused by friction. The flow is considered isentropic in the silencer, which implies a flow free of friction and thus it is assumed that the pressure loss across the silencer can be neglected. As a result, the static pressure at outlet of the nozzle is assumed to be equal to 1 atmosphere in the model.

Within the nozzle, a cone is placed in order to obtain a smooth flow path for the flue gas. The dimensions of the cone and nozzle are illustrated in figure 3.5. It appears how the cross sectional area of the cone decreases faster than the cross sectional area of the nozzle and thus the flow area does not decrease linearly. This is however assumed not to affect the flow and therefore not taken into account in the modeling.

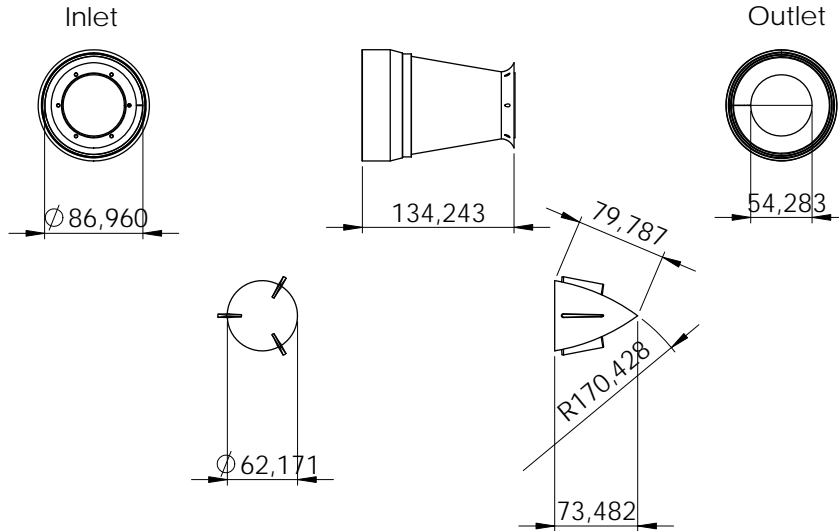


Figure 3.5. Measurements in mm. of the exit nozzle and the cone inside the nozzle.

The purpose of the turbojet engine is to gain thrust. Thrust for a non moving object is a reaction force defined by equation (3.14), where  $V_{12}$  is the absolute velocity at exit of the nozzle in parallel to the direction of the motion.

$$\text{Thrust} = \dot{m} \cdot V_{12} \quad [N] \quad (3.14)$$

The nozzle should be designed to accelerate the flow in order to reach a Mach number close to unity. Thereby, the highest possible thrust is obtained and losses associated with pressure are avoided. This issue depends on the axial speed of the engine and it is further analysed when the results are presented later.

### 3.4 Modeling of the Impeller and Diffuser

The air flow enters the compressor impeller from the inlet nozzle with an absolute velocity that is assumed to be purely axial. The impeller increases pressure, temperature and velocity and thereby the stagnation enthalpy of the flow is increased. As mentioned in section 2.1, the change of enthalpy across the impeller equals the work done by the compressor on the fluid. The specific work is, according to Eulers work equation, defined from the change of tangential velocities, which is summarised by equation (3.15) (Dixon and Hall, 2010). Notice that this is the ideal work where no losses are implemented.

$$\dot{w}_{comp} = U_4 \cdot V_{\theta 4} - U_3 \cdot V_{\theta 3} \quad [J/kg] \quad (3.15)$$

$U$  represents the blade speed at impeller in- and outlet, which differs in a centrifugal compressor due to the increasing radius.  $V_{\theta}$  is the tangential component of the absolute velocity, but as mentioned this component is assumed zero at inlet. However, incidence loss is modeled in a way that affects  $V_{\theta 3}$  and because the absolute velocity is then not purely axial it cannot be neglected from equation (3.15). Modeling of the incidence loss is presented next. The specific work can, for a centrifugal compressor, be related to the rise of stagnation temperature across the impeller with equation (3.16). This equation is

based on the first law of thermodynamics for a steady flow in a control volume with one stream entering and leaving and for which potential energy can be neglected (W.Bathie, 1984).

$$T_{04s} = T_{03} + \frac{\dot{w}_{comp}}{C_p} \quad [K] \quad (3.16)$$

The above given equations are based on an isentropic process, where no losses are implemented and thus  $T_{04s}$  represents the isentropic outlet stagnation temperature. Ideally, the increase in temperature will not be higher than the one defined with equation (3.16), but losses do occur and the real temperature rise across the impeller varies from the isentropic case. The real stagnation temperature rise is introduced with the presentation of compressor losses.

### 3.4.1 Compressor Losses and Efficiency

In the compressor models, four different sources of losses are implemented. Firstly, the modeling of each is described and finally it is presented, how the losses affect the efficiency of the compressor. The calculation of mean dimensions such as hydraulic diameters, channel lengths etc. are left out of the description, as they are rather simple and have a small impact on the final modeling results.

#### Incidence losses

Incidence losses occur when the direction of a flow differs from the optimum flow angle. For airfoils this angle is usually -4 to -8 degrees relative to the blade angle (Glassman, 1994), which is defined from the camber. The sign convention for the optimum flow angle is positive at the pressure side of the blade and negative on the suction side. The blade profiles of both the impeller and diffuser are however not typical airfoils and based on that, it is assumed in the modeling of the compressor that the optimum flow angle equals the blade angle.

With the velocity triangle approach, presented in subsection 3.2.1, it is assumed that the flow adapts to a blade angle by changing its direction instantaneously. This adaptation is, according to *Jiang et al. (2005)*, associated with a flow separation that leads to a degradation of kinetic energy leading to a loss in total pressure. When evaluating the incidence loss at the impeller and diffuser inlet, the losses are associated with tangential velocities, as the axial and radial components for the impeller and diffuser respectively are defined from the conservation of mass flow. To illustrate the losses related to tangential velocities, figure 3.6 sketches a velocity triangle used for implementing incidence losses at inlet of the diffuser. Here it is illustrated how the absolute velocity,  $\bar{V}_4$ , leaving the impeller blade is modeled to adapt with the blade direction by eliminating the tangential component,  $V_{t5}$ , marked in red. To model this loss of tangential velocity, it is assumed that  $V_{r4} = V_{r5}$ , which is only a fair assumption when the change of density and flow area is negligible. It should be mentioned that for diffusers it is the absolute velocity that is exposed to incidence losses, whereas it is the relative velocity for impellers. The loss of tangential component is however the same for both the absolute and relative velocity, as the difference between these equals  $\bar{U}$ . (*Jiang et al., 2005*) (*Glassman, 1994*)

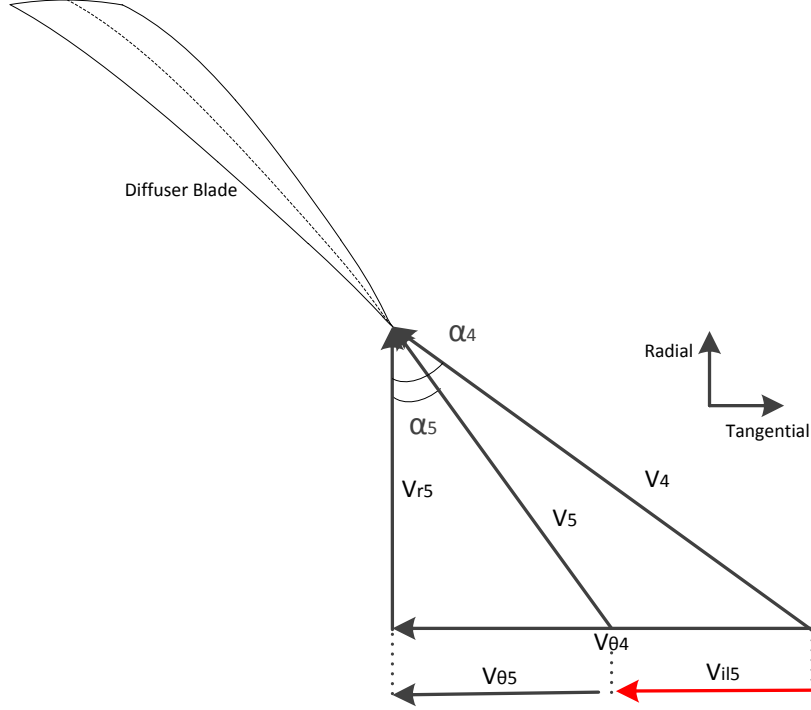


**Figure 3.6.** Incidence loss is related to  $V_{il}$ , which is assumed to be lost. The optimum flow angle is assumed to equal the blade angle in the compressor modeling.

The tangential velocity,  $V_{i15}$ , that is lost at the diffuser inlet is calculated with equation (3.17), which is derived from figure 3.6. Equation (3.18) presents how specific incidence loss,  $\Delta h_{i15}$ , is approximated in the diffuser model. (Jiang et al., 2005)

$$V_{i15} = V_{\theta 5} - V_{\theta b5} = V_{r5} \cdot \tan(\alpha_5) - V_{r5} \cdot \tan(\alpha_{b5}) \quad [m/s] \quad (3.17)$$

$$\Delta h_{i15} = \frac{V_{i15}^2}{2} \quad [J/kg] \quad (3.18)$$

In figure 3.6 the incidence loss is associated with a loss of kinetic energy. The corresponding specific incidence loss,  $\Delta h_{i15}$ , is assumed to work as a heat source at the point where the incidence loss occurs, and thereby the stagnation quantities are kept rather constant. But dependent on the relation between blade angle and flow angle, the incidence loss might be associated with an increase in kinetic energy. This is for instance the case for the impeller inlet and to ensure rather constant stagnation quantities at this point also, the corresponding incidence loss,  $\Delta h_{i13}$  is subtracted from the stagnation temperature at the previous point. Equation (3.19) defines how the specific incidence loss is converted into an increase in static temperature at points where the incidence loss causes a reduction in kinetic energy, and equation (3.20) defines the relation for the opposite case.

$$T_5 = T_4 + \frac{\Delta h_{i15}}{C_p} \quad \Downarrow \Delta \bar{V} \quad [K] \quad (3.19)$$

$$T_3 = T_2 - \frac{\Delta h_{i13}}{C_p} \quad \Uparrow \Delta \bar{V} \quad [K] \quad (3.20)$$

The stagnation quantities cannot be assumed completely constant from impeller outlet to diffuser inlet due to the way incidence loss is defined. Equation (3.18) considers the change of tangential velocity only, which does not correspond completely to the change of absolute velocity. The change of tangential velocity will always be less than the change of absolute velocity. Consequently, there will be a loss of stagnation quantities when the absolute velocity goes down ( $\Downarrow \Delta \bar{V}$ ) and more problematically an increase in stagnation quantities when the absolute velocity is accelerated ( $\Uparrow \Delta \bar{V}$ ). Based on that, the

stagnation temperature at a point with incidence loss is recalculated with equation (3.8). The rise in temperature is assumed to affect pressure isentropically and thus stagnation and static pressures are calculated by equations (3.7) and (3.10). Since temperature and pressure will change due to the incidence loss, so will the density. This affects the velocities at inlet of the diffuser. These have however already been defined, since the radial velocity component of  $\bar{V}_5$  is assumed equal to that of  $\bar{V}_4$ . Therefore, an irregularity of conservation of mass flow may occur. But as long as the incidence loss increases temperature with only a couple of degrees, the irregularity is neglected and the above given approach is assumed correct. This is however kept in mind and the modeling results will be analysed with respect to this issue and the mentioned fact that stagnation quantities might increase at a point where no work is added to the control volume.

### Slip and Deviation

Slip is the phenomenon of flow not leaving an impeller blade at an angle equal to the blade angle at outlet. The purpose of a curved blade is to direct the flow in a particular direction, but with slip the flow will not quite obtain the desired direction and thus slip constitutes a source of loss or more precisely a deviation from ideal performance. According to the Kutta-Jukowsky condition, the pressure difference between the pressure and suction side must go towards zero as the flow approaches the trailing edge. Consequently, the loading of the blade also decreases towards zero somewhere upstream from the trailing edge in order to reach zero at the trailing edge. It is due to the loading that the flow is able to bend along a curved blade. As a consequence of the zero loading at the trailing edge, the flow cannot follow the blade if the camber is curved all the way to the trailing edge. This explains the phenomenon of slip and equation (3.21) shows how a slip factor  $\sigma_4$  is applied to implement slip in the impeller model. The slip factor is in the range from zero to one. (Cumsty, 2004)

$$V_{\theta 4} = \sigma_4 \cdot V_{\theta b 4} \quad [m/s] \quad (3.21)$$

$V_{\theta}$  is the tangential component of the actual flow velocity and  $V_{\theta b}$  is the tangential component of the ideal velocity obtained if slip is neglected.

*Cumsty (2004)* presents three different formulas for determining the slip factor,  $\sigma_4$ , for impeller outlet and states that equation (3.22), approximated by *Wiesner*, is the best expression to use even though it is simple.

$$\sigma_4 = 1 - \frac{\sqrt{\cos(\beta_4)}}{N^{0.7}} \quad [\cdot] \quad (3.22)$$

It appears how the above presented approximation depends only on the number of blades,  $N$ , and the outlet blade angle, which is  $\beta$  for an impeller. It is obvious how a small blade angle demands a small bending of the flow, and thus the slip is small. Likewise, the flow will follow the blade perfectly with an infinite number of blades, which explains how an increasing number of blades reduces slip which agrees with formula (3.22). Equation (3.22) is an approximation where no blade geometry other than the blade angle is taken into account. This is also the case for the other two approximations analysed in *Cumsty (2004)*. This is surprising, as the slip depends on the curvature of the profile near the trailing edge. If the last part of the camber is straight, then the effect of a decreasing blade load near the trailing edge will be reduced and so will the slip. However, based on the priority made by *Cumsty (2004)*, equation (3.22) is assumed to be applicable in the modeling of losses related to slip.

The impeller has 12 blades with a slight backswept outlet angle,  $\beta_4$ , of  $4^\circ$ . With equation (3.22) the slip factor for the impeller outlet can then be determined to be 0.82. According to experimental data presented in *Cumsty (2004)*, the major part of slip factors for centrifugal compressors are between 0.8 and 0.9.

Deviation is the term for slip at a stationary blade row. It is assumed that the deviation at the diffuser outlet can be approximated with equations (3.21) and (3.22) although by using the blade angle  $\alpha_6$  instead of  $\beta_4$ . As a result, the deviation factor  $\sigma_6$  at outlet of the diffuser equals 0.89, which is also within the general range given by *Cumsty (2004)*. In subsection 3.4.3 it is illustrated how slip and deviation affects the velocity triangles.

### Friction loss in Blade Rows

Friction losses are implemented in the impeller and diffuser models even though they are minor due to short blade channels and high Reynolds numbers. Friction loss in both the impeller and diffuser can be approximated by the formula for pressure loss in a pipe due to friction (Ferguson, 1963) (Cumsty, 2004). The expression is given in equation (3.23).

$$\Delta P_f = f \cdot \frac{l}{D_h} \frac{V_m^2}{2} \cdot \rho_m \quad [Pa] \quad (3.23)$$

$l$  is the mean channel length of the impeller and diffuser.  $V_m$  is the average velocity through the channel, which is the relative velocity when considering the impeller and the absolute velocity when modeling the diffuser. The hydraulic diameter,  $D_h$ , is calculated with equation (3.24), where  $h_m$  and  $w_m$  are the mean height and width of the channel.

$$D_h = \frac{4 \cdot h_m \cdot w_m}{2h_m + 2w_m} \quad [m] \quad (3.24)$$

$f$  represents the friction factor in equation (3.23), which is approximated by the Colebrook formula given in equation (3.25) (Munson et al., 2006).

$$\frac{1}{\sqrt{f}} = -2.0 \log \left( \frac{\epsilon}{D_h \cdot 3.7} + \frac{2.51}{\text{Re} \sqrt{f}} \right) \quad [\cdot] \quad (3.25)$$

$\epsilon$  is the mean height of roughness of the pipe, which is assumed to equal that of commercial steel ( $\epsilon = 450 \mu\text{m}$ ) (Munson et al., 2006). The Reynolds number for a centrifugal impeller can, according to Ferguson (1963), be well approximated with equation (3.26).  $h_4$  is the blade height at outlet and  $v_3$  is the kinematic viscosity found at inlet conditions.

$$\text{Re}_{\text{impeller}} = \frac{U_4 \cdot h_4}{v_3} \quad [\cdot] \quad (3.26)$$

The Reynolds number for the diffuser is expressed with equation (3.27), which is based on the general formula for flow in a duct.  $D_h$  is the hydraulic diameter of the diffuser. (Munson et al., 2006)

$$\text{Re}_{\text{diffuser}} = \frac{V_5 \cdot D_h}{v_5} \quad [\cdot] \quad (3.27)$$

The pressure drops,  $\Delta P_{f4}$  and  $\Delta P_{f6}$ , due to friction losses in the impeller and diffuser channels are subtracted from the outlet stagnation pressures  $P_{04}$  and  $P_{06}$  respectively. Meanwhile, the pressure drops are converted into a specific enthalpy change with equation (3.28), which is used to model the rise in temperature due to friction losses. In other words, the friction loss is modeled as a drop in pressure and a rise in temperature.

$$\Delta h_{fl} = \frac{\Delta P_f}{\rho_m} \quad [J/kg] \quad (3.28)$$

With respect to the diffuser, the friction loss,  $\Delta h_{fl}$ , is just added as a heat source with same procedure as shown for incidence losses in equation (3.19). For the impeller it is more complicated as shaft work is added to the fluid throughout the impeller. Therefore, the procedure is instead to sum up friction losses, which includes friction loss for each blade channel and disk friction,  $\Delta h_{df}$  (described next). Then an friction efficiency,  $\eta_{fl4}$ , can be calculated for the impeller from equation (3.29). Notice,  $\eta_{fl4}$  is only used in the modeling of friction losses and does not say anything about impeller performance in general.

$$\eta_{fl4} = 1 - \frac{\Delta h_{fl} + \Delta h_{df}}{\Delta h_{fl} + \Delta h_{df} + \dot{w}_{\text{comp}}} \quad [\cdot] \quad (3.29)$$

$\dot{w}_{\text{comp}}$  is the ideal specific impeller work, which was previously defined with equation (3.15) from tangential velocity components. The so called friction efficiency  $\eta_{fl4}$  can also be expressed as the

isentropic change in stagnation temperature to the real change in stagnation temperature. The real stagnation temperature  $T_{04}$  at impeller outlet can then be calculated with equation (3.30).

$$T_{04} = \frac{T_{04s} - T_{03}}{\eta_{fl4}} + T_{03} \quad [K] \quad (3.30)$$

Now, to calculate the increase in stagnation pressure across the impeller, equation (3.7) is used. But notice that it is the ideal stagnation temperature,  $T_{04s}$ , that is used in this equation to calculate the pressure at outlet of the impeller, and not the real stagnation temperature,  $T_{04}$ . This is caused by the fact that the process from  $T_{03}$  to  $T_{04}$  is not isentropic due to the friction losses, whereas the process from  $T_{03}$  to  $T_{04s}$  is isentropic.

### Disk Friction

Disk friction represents the amount of additional power consumption of the compressor due to friction when the impeller rotates in the fluid. There are various approaches to the modeling of disk friction and equation (3.31) used by *Pfleiderer and Petermann* is assumed to be applicable for a centrifugal compressor impeller (Grundfos, 2008).  $\rho_m$  and  $\nu_m$  are mean values of density and kinematic viscosity between in- and outlet of the impeller.  $l_{gap}$  is the gap between the impeller and housing. This value is difficult to measure and therefore assumed to be 0.3 mm, which is the same as the gap between outlet of impeller and inlet of diffuser.

$$\Delta h_{df} = k \cdot \rho_m \cdot U_4^3 \cdot D_4 \cdot (D_4 + 5 \cdot l_{gap}) \quad [J/kg] \quad (3.31)$$

$$k = 7.3e^{-4} \left( \frac{2 \cdot \nu_m \cdot 10^6}{U_4 \cdot D_4} \right)^s \quad [\cdot] \quad (3.32)$$

$k$  is an empirical value defined by equation (3.32) where  $s$  is an exponent that equals  $1/6$  for smooth surfaces, which is considered to be the case for the impeller. As mentioned  $\Delta h_{df}$  is applied in equation (3.29) to implement the disk friction as a heat source in the modeling of the impeller outlet.

To sum up, disk friction has been implemented in the impeller model, whereas pressure losses caused by friction in blade rows are modeled for both impeller and diffuser. Likewise, incidence losses and losses related to slip and deviation have been considered in the compressor models. The formulation for the impact of losses on compressor efficiency is presented next.

### 3.4.2 The Efficiency of the Compressor

Two main definitions of efficiency are the total-to-static efficiency and the total-to-total efficiency. The first one can be applied when the exit kinetic energy does not contribute to the process, whereas the second efficiency is used when the exit kinetic energy is used in the particular process. For a turbojet engine the velocity is never lost, since it delivers the thrust at exit of the engine. Based on this, the efficiencies considered in this report are all total-to-total. (Dixon and Hall, 2010)

The total-to-total efficiency,  $\eta_{comp}$ , for the compressor is defined with equation (3.33) as minimum adiabatic work over the real adiabatic work input. The minimum adiabatic work equals the stagnation enthalpy change during the isentropic process between the pressure  $P_{02}$  and  $P_{06}$ . The real adiabatic work equals the real stagnation enthalpy change between the same two pressures. (Dixon and Hall, 2010)

$$\eta_{comp} = \frac{h_{06s} - h_{02}}{h_{06} - h_{02}} \quad [\cdot] \quad (3.33)$$

When the efficiency is not unity it is due to incidence loss, disk friction and friction loss in the blade rows. As mentioned, slip and deviation is not directly a loss and thus it does not affect the efficiency. Both the modeled and measured compressor efficiencies will be presented along with the results in chapter 4.

### 3.4.3 Velocity Triangles in the Compressor

The modeling is based on two dimensional velocity triangles, even though the flow is three dimensional. This is done for simplicity, and thus one of three velocity components is neglected. In the previous sections slip and deviation as well as incidence loss were presented. These phenomena affect the velocity triangles, which is illustrated in this subsection. Remark, that the triangles are sketches without exact dimensions.

At inlet of the impeller it is the radial velocity components that are neglected, whereas it is the axial velocity components at impeller outlet. This is due to the axial flow direction at inlet, the radial flow direction at outlet and the fact that the blade speed is always purely tangential. In the diffuser it is the axial component that is neglected for both in- and outlet. Figure 3.7 illustrates a velocity triangle where outlet (2) of the nozzle and inlet (3) of the impeller are combined. In that way it is illustrated how the incidence loss is modeled.

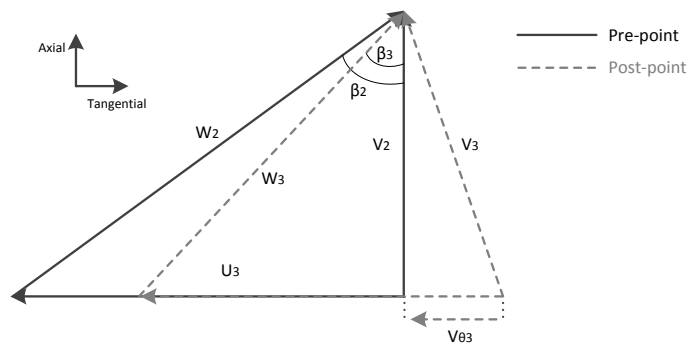


Figure 3.7. Velocity triangle used to model the inlet of the impeller.

The incidence loss is defined as the change in tangential velocity from  $V_{\theta 2}$  to  $V_{\theta 3}$ . Notice, how the absolute velocity  $\bar{V}_3$  becomes longer due to the modeling of incidence loss. This is remarkable and seems incorrect, but when  $\bar{V}_3$  has a tangential component in the same direction as  $\bar{U}$ , the impeller work  $\dot{w}_{comp}$  is reduced, which can be seen from equation (3.15). Furthermore, the modeling is done in such a way, that the static temperature and pressure decreases as a result of the increase in absolute velocity.

Figure 3.8 illustrates the velocity triangle used to define size and direction of the absolute velocity,  $\bar{V}_4$ , at impeller outlet and more importantly, the tangential component,  $V_{\theta 4}$ , which is used in equation (3.15) to calculate the specific work done by the impeller. At impeller outlet, the relative velocity,  $\bar{W}_4$ , is leaving with an angle,  $\beta_4$ , to the radial direction. The flow direction is not parallel to the blade angle  $\beta_{b4}$ , since the modeling accounts for slip at outlet of the impeller. As defined, slip reduces the length of the ideal  $V_{\theta b4}$ , so that the absolute flow becomes more radial than ideally.

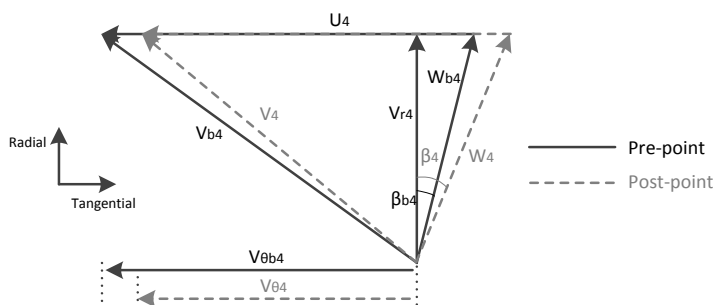


Figure 3.8. Velocity triangle for impeller outlet illustrates how slip makes the velocity triangle deviate from the ideal case.

Figure 3.9 illustrates a combination of the velocity diagram for impeller outlet and diffuser inlet. Again, notice how incidence loss affects the velocity triangles.

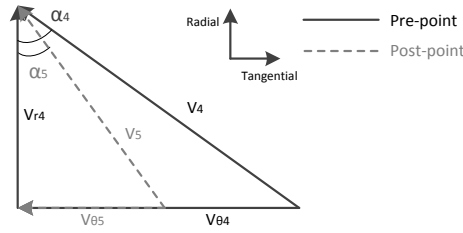


Figure 3.9. Velocity triangle for diffuser inlet.

In figure 3.9 the absolute velocity  $\bar{V}_5$  is reduced compared to  $\bar{V}_4$  and thus the incidence loss is modeled as an increase in static pressure and temperature.

Finally the velocity diagram for the diffuser outlet is illustrated with figure 3.10.

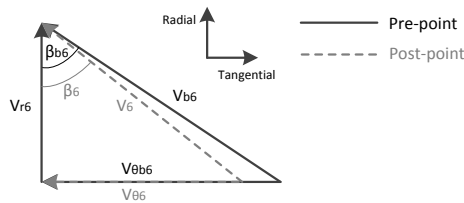


Figure 3.10. Velocity triangle for diffuser outlet.

From the velocity triangle it appears how the deviation factor decreases the length of  $\bar{V}_6$  compared to the ideal case.

The modeling of the compressor has been described in this section. In the following section the modeling of the combustion chamber will be presented.

### 3.5 Modeling the Combustion Chamber

This section presents the modeling of the combustion chamber. Test results of the fuel consumption,  $\dot{m}_{\text{fuel}}$ , and the inlet air mass flow,  $\dot{m}_{\text{air}}$ , are used to determine the mass flow through the modeling as a function of RPM. Furthermore, the AF ratio is determined by the ratio of  $\dot{m}_{\text{air}}$  and  $\dot{m}_{\text{fuel}}$ . To validate the calculation the excess air ratio,  $\lambda$ , is determined and the concentration of oxygen is measured in the exhaust pipe during tests. The test stand used for the measurements is described in appendix B. The validation will be described in details in subsection 3.5.2.

The air flow from the diffuser enters the combustion chamber where it is mixed with a small amount of fuel. In the modeling of the combustion chamber no flow patterns are considered, only composition of the flue gas and its temperature. The combustion reaction is modeled in the program CEA NASA for chemical equilibrium calculations. In CEA NASA the inlet temperature of the reactants must be known along with inlet pressure and the AF ratio of the process. From the input parameters CEA NASA calculates the adiabatic flame temperature and the composition of reaction products. In the modeling the adiabatic flame temperature is implemented as a function of RPM.

### 3.5.1 Determining the adiabatic flame temperature by use of $\dot{m}_{\text{fuel}}$ and $\dot{m}_{\text{air}}$

The AF ratio is directly determined from the tests using equation (2.4) presented in section 2.2 about the considerations related to the combustion.

The amount of excess air,  $\lambda$ , entering the combustion chamber is closely related to the AF ratio.  $\lambda$  is given as the ratio of the actual amount of air entering the combustion to the stoichiometric amount as stated in equation (3.34).

$$\lambda = \frac{\dot{m}_{\text{air}}}{\dot{m}_s} \quad [.] \quad (3.34)$$

To determine the stoichiometric amount of air the stoichiometric combustion reaction is used. In appendix D it is described in details how  $\dot{m}_s$ ,  $\lambda$  and AF are determined. The engine tests measuring  $\dot{m}_{\text{fuel}}$  and  $\dot{m}_{\text{air}}$  are done at different RPM to determine how the AF ratio and  $\lambda$  varies at different speeds in order to model the mass flow correctly. Figure 3.11 shows the results of the calculations. The calculation is based on linear approximations of the fuel flow and the air flow. During the tests it was possible to run the engine within an RPM of 45,000 to 80,000 and therefore the figure is plotted in this range.

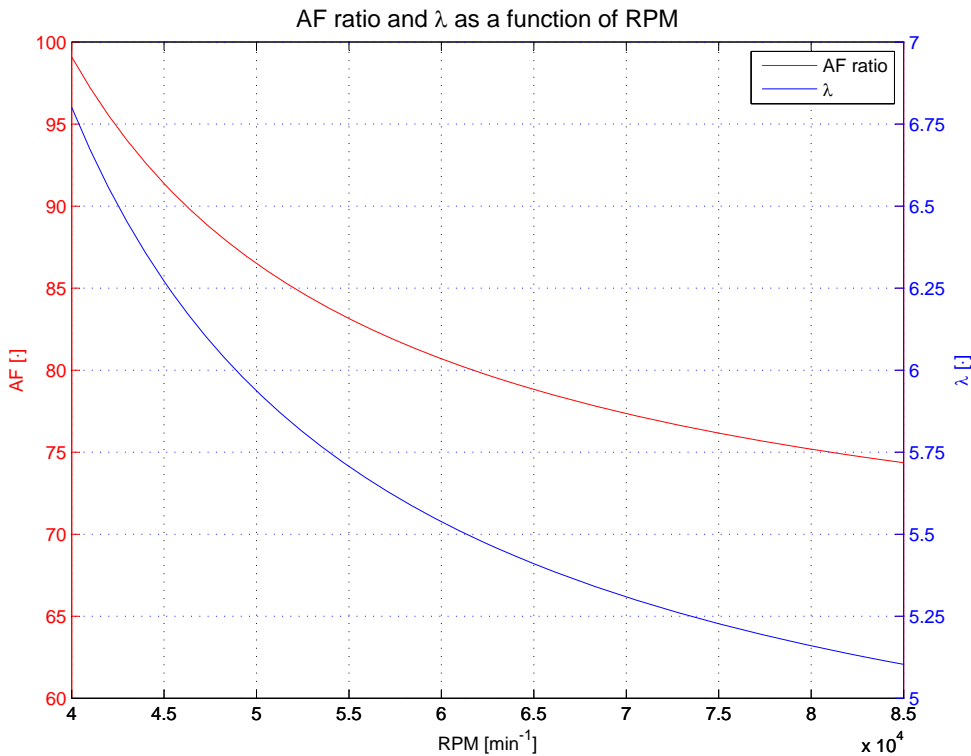


Figure 3.11. The AF ratio and excess air,  $\lambda$ , as a function of RPM based on experimental data and the stoichiometric amount of air,  $m_s$ .

From figure 3.11 it can be seen how both AF and  $\lambda$  decrease as RPM increases. The AF ratio is in the range of 70 to 100 kg air per kg fuel and  $\lambda$  is in the range of 5 to 7 meaning that around 5 to 7 times the stoichiometric amount of air enters the combustion chamber. An AF ratio calculated using the specifications from *Turbine Technologies* listed in table 2.1 reveals a ratio of 80 at a RPM of 87,000 which deviates around 10 % from the AF ratio in figure 3.11. The specifications given are however highly rounded numbers and thus not considered more accurate than the calculated results.

The calculated AF ratio is implemented in CEA NASA to determine the adiabatic flame temperature as a function of RPM. The inlet temperature, pressure and stoichiometric amounts of reactants are implemented in CEA NASA as well. Figure 3.12 shows the data points determined in CEA NASA along

with a quadratic regression that describes how the flame temperature vary with RPM. The CEA NASA results are given in appendix C.

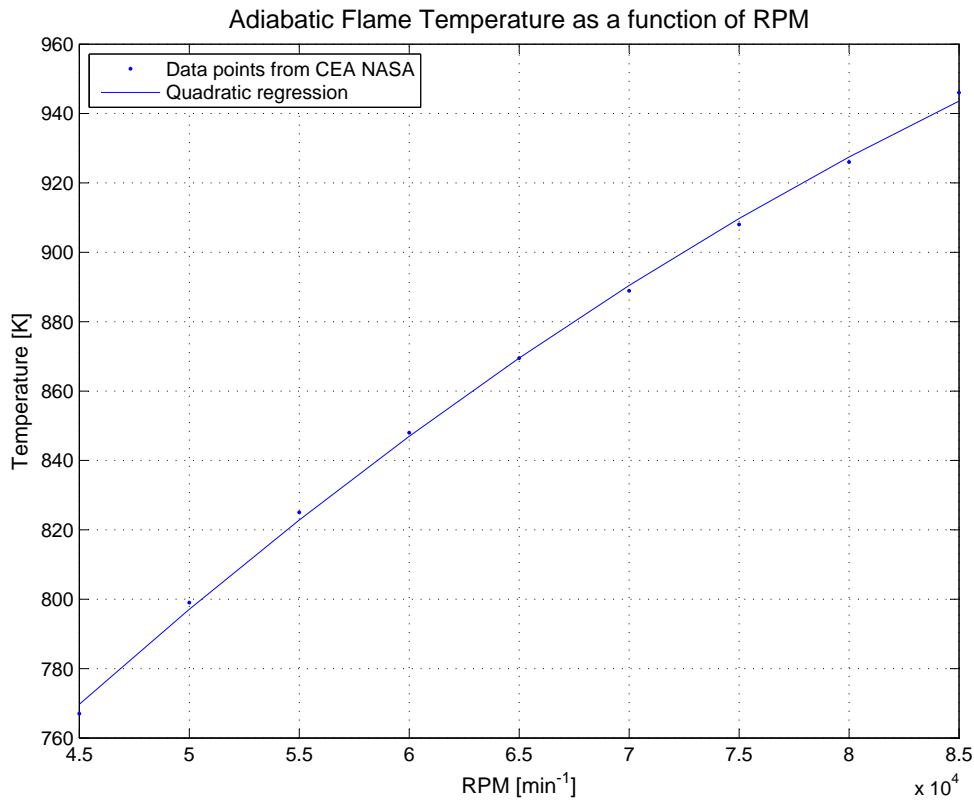
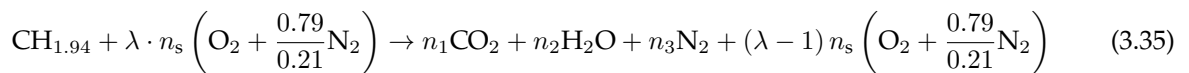


Figure 3.12. The adiabatic flame temperature calculated in CEA NASA as a function of RPM.

The regression of the adiabatic flame temperature is implemented in the combustion modeling to vary the outlet temperature of the combustion chamber with inlet pressure, inlet temperature and RPM.

### 3.5.2 The Oxygen Content in the Exhaust Gas

During the combustion reaction carbon dioxide, water and nitrogen are formed as stated in section 2.2 describing the combustion chamber. Since excess air is added, the reaction products also contain oxygen. The combustion process is given in equation (3.35) where  $n_s$  is the stoichiometric amount of air entering the combustion chamber. The fuel is assumed to consist of  $\text{CH}_{1.94}$ , since CEA NASA uses this composition for the jet fuel JP-4.



The calculated excess air ratio is used in the combustion reaction to determine the mole fraction of oxygen in the flue gas in order to validate the results. The mole content is given as the number of moles of air in the combustion products to the total number of moles in the products as stated in equation (3.36).

$$\text{O}_2 = \frac{n_{\text{O}_2}}{n_{\text{total}}} \quad [\text{mole \%}] \quad (3.36)$$

$n_{\text{O}_2}$  and  $n_{\text{total}}$  are estimated from the combustion reaction, equation (3.35), and the calculated oxygen content can be compared with the content measured in the engine test. In the test the oxygen content is measured at the exhaust outlet. In order to compare the oxygen contents the reference point must be the same and thus the approximated oxygen content must be corrected to the exhaust outlet and not the combustion outlet. At the inlet of the test stand there is a gap where surrounding air,  $\dot{m}_{\text{sur6}}$ , can enter

and be added in the exhaust pipe. If this is the case surrounding air might enter the exhaust pipe and the flue gas contains a larger amount of air, which must be implemented in order to have the same reference point for the comparison. At the exit of the stand there is also a gap, used to cool the exhaust, where the surrounding air,  $\dot{m}_{sur7}$ , can leave the stand. The gaps at inlet and outlet are illustrated in figure 3.13. The difference in the surrounding air flows equals the amount of surrounding air,  $\Delta\dot{m}_{sur}$ , that enters the exhaust pipe.

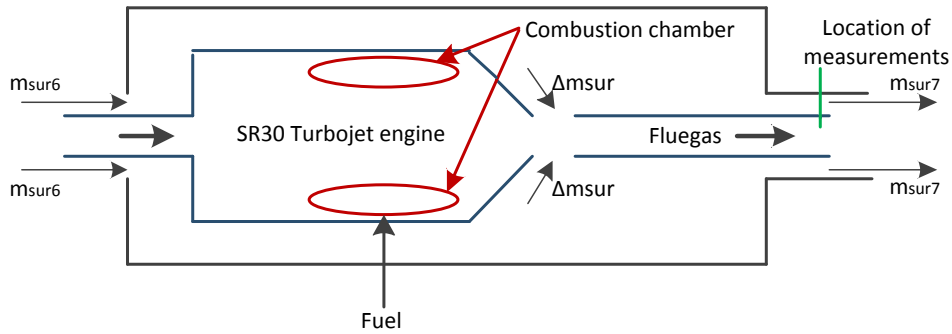


Figure 3.13. The test stand where the gap at inlet and outlet are illustrated.

The combustion reaction, equation (3.35), then contains yet a term on the product side related to  $\Delta\dot{m}_{sur}$ . The product side of equation (3.35) is then extended with the term given in equation (3.37) where  $\Delta n_{sur}$  is the number of moles of surrounding air that enters the exhaust pipe.

$$\Delta n_{sur} \left( O_2 + \frac{0.79}{0.21} N_2 \right) \quad (3.37)$$

As mentioned the air entering the exhaust pipe,  $\Delta n_{sur}$ , must be taken into account when estimating the oxygen content in the exhaust pipe in order to have the same reference point. To determine  $\Delta n_{sur}$  the velocities at the in- and outlet gap are measured at different RPM. The mass flows are then determined from equation (3.1) presented in section 3.1 and  $\Delta n_{sur}$  can be calculated as the difference in inlet and outlet gap mass flow. The oxygen content at exhaust outlet is expected to be larger than the content at combustion outlet since the surrounding air related to  $\Delta n_{sur}$  is added in the exhaust gas.

In appendix E  $\Delta n_{\text{sur}}$  is calculated and it is described in details how the estimated oxygen content in the exhaust pipe is calculated. Figure 3.14 shows the results where the data points, found in the test, are shown along with a quadratic regression describing the data points. The estimated oxygen content at the exhaust outlet is also shown in the figure to be compared with the data points. Furthermore the estimated oxygen content at combustion outlet is shown in order to check that the oxygen content at combustion outlet is actually smaller than the estimated content at exhaust outlet.

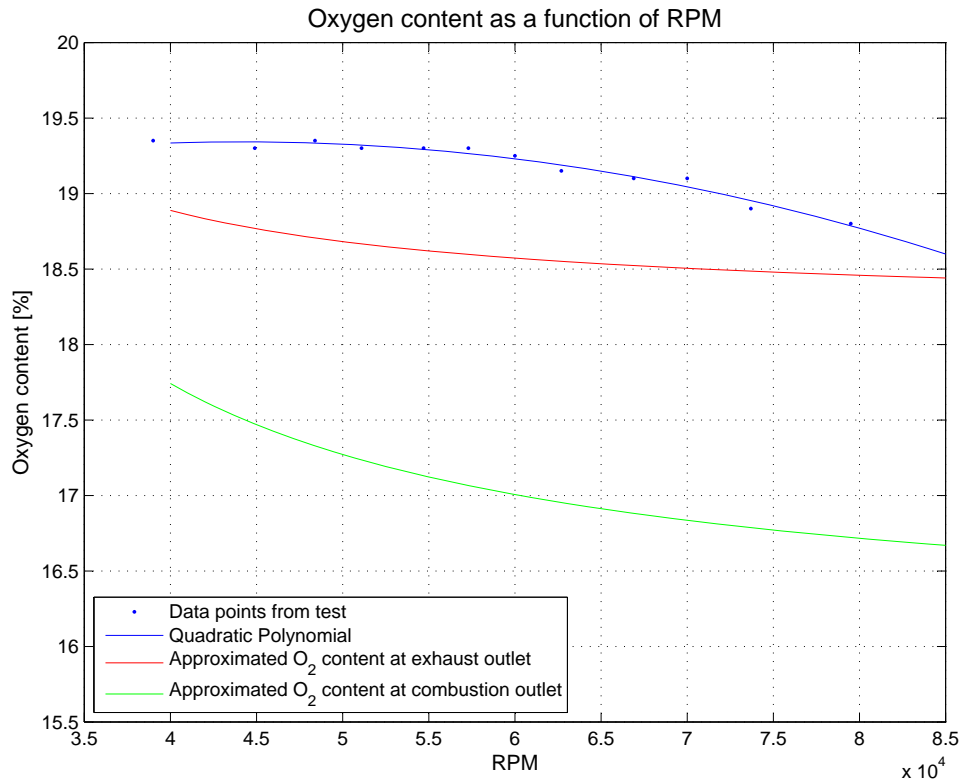


*Figure 3.14.* The oxygen content in the flue gas as a function of RPM. Data points from tests and estimations from calculations are both shown.

From figure 3.14 it can be seen that the measured oxygen content is higher than the estimated content. The maximum deviation of the measured oxygen content to the estimated content is 3.6 %, thus, it seems that the estimated and the measured oxygen content match each other.

### 3.5.3 Determining the Excess Air Ratio from the Oxygen Content

The AF ratio and  $\lambda$  have been calculated from  $\dot{m}_{\text{air}}$  and  $\dot{m}_{\text{fuel}}$  and the calculated parameters seem to fit when comparing the oxygen contents. The parameters can also be estimated from the combustion reaction using the measured oxygen content. Equation (3.36) can be used to determine  $\lambda$  as a function of RPM since  $n_{\text{O}_2}$  and  $n_{\text{total}}$  are functions of  $\lambda$ . Figure 3.15 shows the comparison of  $\lambda$  calculated from the measured air mass flow,  $\dot{m}_{\text{air}}$ , and from the measured oxygen content.

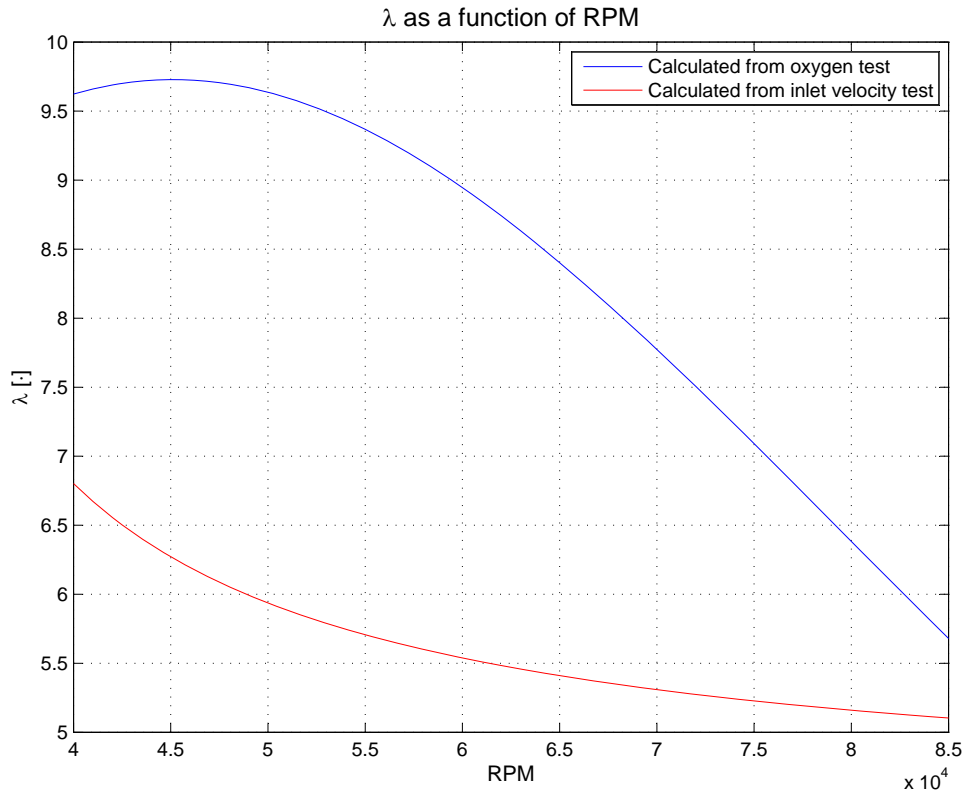


Figure 3.15.  $\lambda$  calculated from the inlet air mass flow test compared to the calculation from the oxygen test.

Using the measured oxygen content gives a higher amount of excess air compared to using  $\dot{m}_{\text{air}}$  and thus the influence of the measured parameters are examined. If  $\dot{m}_{\text{air}}$  and  $\dot{m}_{\text{fuel}}$  are varied with  $\pm 1\%$  respectively,  $\lambda$  reaches a maximum deviation of 2%, while the deviation if decreasing the oxygen content by 1% is 11.8-14.4%. This indicates that  $\lambda$  is highly dependent of the oxygen content whereas the fuel consumption and inlet air mass flow have minimum influence. Therefore it seems a good approximation determining  $\lambda$  using  $\dot{m}_{\text{air}}$  and  $\dot{m}_{\text{fuel}}$  even though the measured results might deviate because of measurement uncertainties. This is due to the fact that deviations of the measured oxygen content affects the results to a greater extent than deviations of the measured  $\dot{m}_{\text{air}}$  and  $\dot{m}_{\text{fuel}}$ .

### 3.6 Modeling of the Axial Turbine

The axial turbine in the SR-30 turbojet engine has one stage consisting of a stator and a rotor. The modeling of these is similar to the compressor modeling presented in section 3.4. The purpose of the stator is to accelerate the flow in order to obtain a high tangential velocity component at outlet of the stator. This component imposes a force on the turbine rotor, which in other words drives the shaft and the compressor impeller. The specific work,  $\dot{w}_{\text{turbine}}$ , done by the turbine on the fluid is defined from the loss of tangential velocity across the rotor as defined with equation (3.38). The work is negative as energy is extracted from the flow, just as the specific compressor work is positive. The turbine work calculated in equation (3.38) is determined without considering any losses in the turbine and thus it is the ideal

turbine work. (W.Bathie, 1984)

$$\dot{w}_{turbine} = -(U_{10} \cdot V_{\theta 10} - U_{11} \cdot V_{\theta 11}) \quad [J/kg] \quad (3.38)$$

The radii of the rotor are very similar for in- and outlet and thus the work depends the most on the change in tangential velocity components.

Due to negative specific work across the turbine rotor, the stagnation temperature will decrease at this stage. Equation (3.39) relates the change of stagnation temperature to the specific turbine work for an isentropic process without losses (W.Bathie, 1984).

$$T_{011s} = T_{10} + \frac{\dot{w}_{turbine}}{C_p} \quad [K] \quad (3.39)$$

Since the model accounts for losses there will be a difference between the isentropic stagnation temperature,  $T_{011s}$ , and the real one,  $T_{011}$ . This difference can be derived from equation (3.40). The approach of calculating the different losses in the turbine is described in subsection 3.6.1.

$$T_{011} = T_{010} - \eta_{fl11} (T_{010} - T_{011s}) \quad [K] \quad (3.40)$$

$\eta_{fl11}$  is an efficiency used only to implement friction losses related to disk friction and friction in the blade rows of the rotor, thus it should not be used to characterise the turbine in any way.  $\eta_{fl11}$  is defined from equation (3.41), where  $\Delta h_{fl11}$  is friction in the blade rows and  $\Delta h_{df11}$  represents disk friction in the rotor.

$$\eta_{fl11} = 1 - \frac{\Delta h_{fl11} + \Delta h_{df11}}{\Delta h_{fl11} + \Delta h_{df11} + \dot{w}_{turbine}} \quad [\cdot] \quad (3.41)$$

The stagnation pressure at rotor outlet is defined from the isentropic stagnation temperature  $T_{011s}$  and the pressure drop  $\Delta P_{fl11}$  caused by friction in the blade rows. The relation used in the modeling is given in equation (3.42).

$$P_{011} = P_{010} \cdot \left( \frac{T_{011s}}{T_{010}} \right)^{\frac{\kappa}{\kappa-1}} - \Delta P_{fl11} \quad [kPa] \quad (3.42)$$

Once the stagnation quantities are calculated with the above given formulas, the static quantities can be calculated from the relations given in section 3.2 about general formulas for isentropic compressible flows. Though, the definition of losses must be presented before applying the above given formulas.

### 3.6.1 Turbine Losses

In subsection 3.4.1 it was described how losses such as friction in the blade rows, disk friction and incidence losses are implemented in the compressor modeling. Also slip and deviation are described, and it is the exact same losses, which have been implemented in the turbine modeling. In other words, the turbine modeling includes incidence losses at stator and rotor inlet, deviation at stator outlet, slip at rotor outlet, friction in the blade rows for both stator and rotor and disk friction associated with the rotor. The losses in the turbine modeling are determined using the same approaches as the ones described in subsection 3.4.1 and to avoid any repetition, the reader is encouraged to look through subsection 3.4.1 to understand the approach of loss modeling in the turbine.

In the compressor modeling it was assumed that an optimum flow angle equals the blade angle, since the blade profiles were not typical airfoils. In the turbine however, the blade profiles are typical airfoils and an optimum flow angle is -4 to -8 degrees relative to the blade angle as described in subsection 3.4.1. This is implemented in the modeling of the turbine, where the optimum flow angle is assumed to be -6 degrees.

### 3.6.2 Efficiency and Reaction Stage

The definition of the total-to-total turbine efficiency is presented with equation (3.43). The total-to-total efficiency is defined as the real specific work of the turbine over the ideal specific work.

$$\eta_{turbine} = \frac{h_{07} - h_{011}}{h_{07} - h_{011s}} = \frac{1 - \frac{T_{011}}{T_{07}}}{1 - \left(\frac{P_{011}}{P_{07}}\right)^{\frac{\kappa-1}{\kappa}}} \quad [.] \quad (3.43)$$

By calculating  $\eta_{turbine}$ , the influence of losses in the turbine can be analysed. This will be done, when presenting the results in the next chapter.

In section 2.3 about degree of reaction for axial turbines, it is described how the dimensions of the SR-30 turbine have similarities to those of a zero reaction turbine. The degree of reaction is defined as the ratio of enthalpy change in the rotor over the enthalpy change across both stator and rotor, as given in equation (3.44). (Dixon and Hall, 2010)

$$R = \frac{h_9 - h_{11}}{h_8 - h_{11}} \quad [.] \quad (3.44)$$

The reaction stage will be calculated and discussed in the modeling results.

### 3.6.3 Velocity Triangles

The flue gas leaving the combustion chamber enters the stator part of the turbine. As for the air flow at inlet of the compressor impeller, it is again assumed that the flue gas has a purely axial velocity, thus potential swirl is neglected. Figure 3.16 illustrates the velocity triangle at inlet of the stator, and it appears how the absolute velocity increases from step 7 to 8. This is due to the way incidence loss is modeled. To compensate for the increase in velocity, the incidence loss,  $\Delta h_{i18}$ , is subtracted from the static temperature.

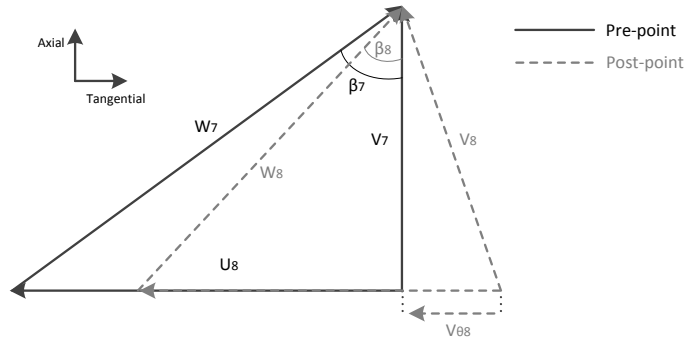


Figure 3.16. Velocity triangle for inlet of turbine stator.

At outlet of the stator the blade angle,  $\alpha_9$ , is  $71^\circ$ , and when the axial component is defined from the conservation of mass flow, the absolute velocity becomes quite big because of this angle. This agrees with the purpose of the stator, which is to accelerate the flow. Deviation occurs at outlet of the stator and the effect of this appears from figure 3.17, where the tangential component of the absolute velocity is decreased from  $V_{\theta b9}$  to  $V_{\theta 9}$ .

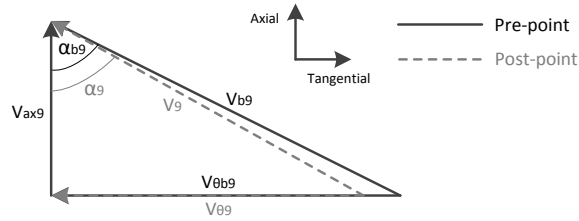


Figure 3.17. Velocity triangle for outlet of turbine stator.

Figure 3.18 is a sketch of the velocity triangle at inlet of the turbine rotor and this sketch must be noticed, as it illustrates complications in the modeling. According to *Ferguson (1963)* a flow may accelerate into a blade row if the flow angle is negative relative to the optimum flow angle. As a result, it is assumed that an increase of absolute velocity from  $\bar{V}_9$  to  $\bar{V}_{10}$  is likely to happen. However, the change of flow angle from  $\beta_9$  to  $\beta_{10}$  is significant and so is the increase of velocity. This is analysed in details when the turbine results are presented in section 4.6.4.

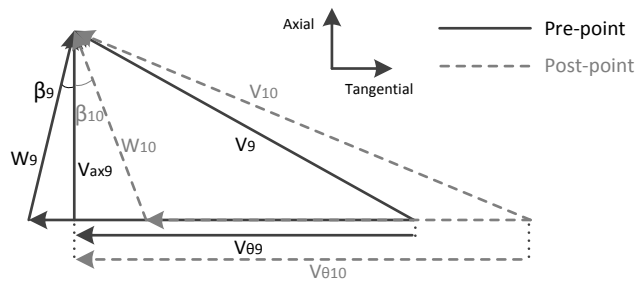


Figure 3.18. Velocity triangle for inlet of turbine rotor.

The impact of slip at rotor outlet is illustrated with the velocity triangle sketched in figure 3.19. It appears how slip makes the absolute velocity leave the rotor in a more axial direction than if slip was somehow avoided. An axial direction is probably preferable, as the flow enters the nozzle.

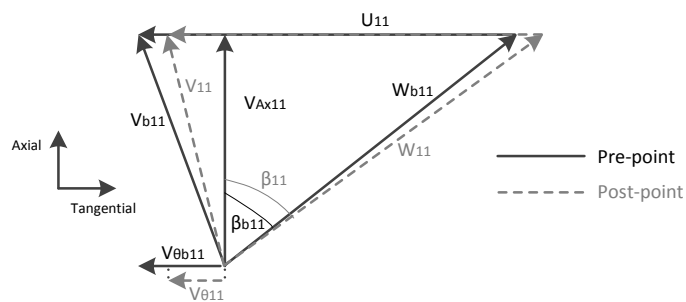


Figure 3.19. Velocity triangle for outlet of turbine rotor.

Figure 3.20 combines the velocity triangles for in- and outlet of the rotor. This is a standard way to visualise the turbine work,  $\dot{w}_{turbine}$ , which according to equation (3.38) is derived from the change of tangential flow velocity. Normally, a multistage turbine can be characterised with respect to reaction stage with this diagram, because the axial velocity component for multistage turbines is usually equal at in- and outlet of the rotor. This is however not the case for the SR-30 turbine, which is why the degree of reaction cannot be determined from this figure.

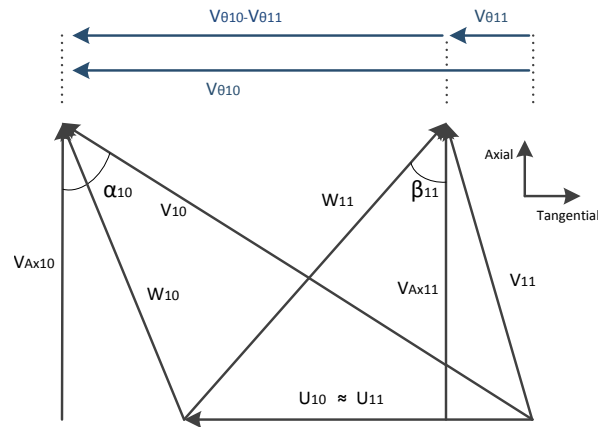


Figure 3.20. Characteristic combined velocity triangle for rotor.

The different approaches used to model the SR-30 turbojet engine have been described throughout this chapter. In general it has been chosen to use compressible flow relations in the modeling along with two dimensional velocity triangles. The centrifugal compressor and the axial turbine are modeled similarly with respect to specific work and implementation of losses. Modeling of the combustion chamber is based on experiments defining the AF ratio and thereby a relation between engine speed and adiabatic flame temperature is made. The next step is to present and validate the modeling results.

# Modeling Evaluation and Validation 4

Modeling results of the SR-30 turbojet engine are evaluated at a range of engine speeds in this chapter. The scientific approach of this project is to make a validated model, and therefore the inductive modeling results will be compared with experimental results from test runs of the SR-30 engine in order to validate the modeling by deduction. Appendix B presents how the test runs have been performed with respect to approach, measuring devices and treatment of data. However, it should be mentioned that the measurements are sorted to remove the transient periods in which the engine is accelerated. In these periods temperatures and pressures are moving towards a static value, and since the modeling results only consider static periods, the transient measurements are not relevant.

Firstly, the results of each submodel are presented and compared with the test results. Thermodynamic properties and losses will be presented as a function of engine speeds, but the modeling results will also be evaluated at a specific speed equal to 70,000 RPM in order to illustrate what happens to the fluid throughout the SR-30 turbojet engine. Finally, relevant results of the complete SR-30 engine, such as thrust and overall efficiency, are compared with both test results, a similar modeling of the SR-30 engine made by *Witkowski et al. (2003)* and the specifications given by the manufacturer *Turbine Technologies (2012)* presented in table 2.1.

## 4.1 The Inlet Nozzle

As mentioned in section 3.3, regarding modeling of the inlet nozzle, the temperature sensor is located at some distance upstream from the outlet of the nozzle in the test engine. For accurate validation the nozzle temperature is evaluated at this same location in the model. Table 4.1 lists the modeling results with respect to thermodynamic properties, mass flow, absolute velocity and Mach number for the nozzle modeling at an engine speed equal to 70,000 RPM.

Component	P	T	P <sub>0</sub>	T <sub>0</sub>	h <sub>0</sub>	m	V	ρ	Mach
	[kPa]	[K]	[kPa]	[K]	[kJ/kg]	[kg/s]	[m/s]	[kg/m <sup>3</sup> ]	[·]
Inlet nozzle	101	287	101	287	413	0.294	14	1.23	0.04
Outlet nozzle	97	286	101	287	413	0.294	84	1.20	0.25

*Table 4.1.* Modeling results at an engine speed of 70,000 RPM.

From the table it appears how the stagnation quantities are constant, while temperature and pressure decreases because of the acceleration of the fluid.

Figure 4.1 presents the static temperature and pressure at outlet of the inlet nozzle as a function of engine speed for both measured values from the test run and predicted values from the modeling. The temperature and pressure at the inlet nozzle depend on the outside conditions, but at the test run the ambient temperature was measured to 13.7°C, which is therefore used as an input in the modeling.

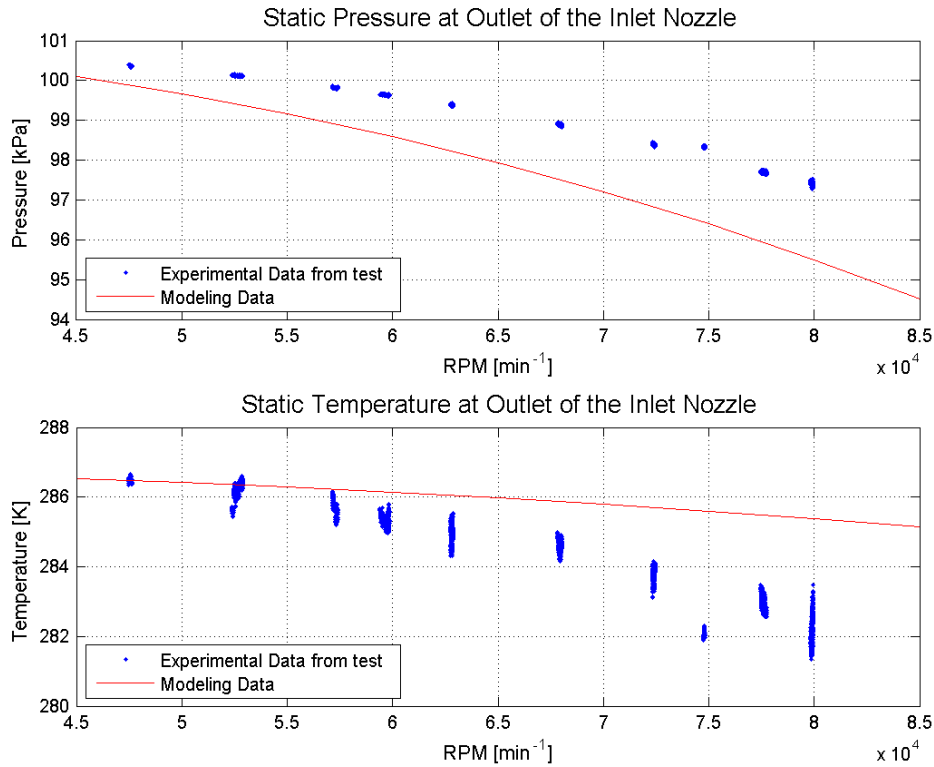


Figure 4.1. Static temperature and pressure at outlet of the inlet nozzle for measured and predicted values.

It appears from figure 4.1, how the tendency of measured and predicted pressures have a fine agreement. The predicted pressures are below the measured ones, which agrees with the fact that any friction in the nozzle has been neglected in the model. A pressure drop due to friction would increase the predicted pressures a bit, since friction will counteract the acceleration of the fluid in the nozzle, and thus the pressure drop across the nozzle will decrease. However, friction is neglected in the nozzles because it is expected to be in the range of 10 Pa, and thus it does not explain the deviation between predicted and measured values, since the deviation, at most, is just below 2 kPa.

The modeled mass flow of air is based on experimental data and any uncertainties will have influence on the output of the model. A predicted pressure, lower than the measured, indicates that the modeled mass flow is too high, since a higher mass flow results in larger acceleration and thus a lower pressure at outlet. On the contrary, the measured temperature is, according to figure 4.1, lower than the predicted value, which indicates that the mass flow of air is set too low in the model, since also temperature decreases with acceleration.

It is worth a remark that the drop in temperature at low engine speeds is only around 1 K. Though, the measurements agree with this drop and based on that it is considered correct. In general, the deviation between predicted and measured values are below 2 kPa and 3 K for pressure and temperature respectively, and the tendencies when the engine speed is increased are similar. As a result, the modeling of the inlet nozzle is considered useful and thus the predicted values can be used as input to the compressor model.

## 4.2 The Compressor Results

Since the air is accelerated by shaft work in the impeller and has its velocity reduced in the diffuser, an increase in static temperature and static pressure is expected throughout the compressor. This hypothesis matches the modeling results listed in table 4.2 for an engine speed equal to 70,000 RPM.

Component	P [kPa]	T [K]	P <sub>0</sub> [kPa]	T <sub>0</sub> [K]	h <sub>0</sub> [kJ/kg]	m [kg/s]	V [m/s]	ρ [kg/m <sup>3</sup> ]	Mach [·]
Inlet nozzle	101	287	101	287	413	0.294	14	1.23	0.04
Outlet nozzle	97	286	101	287	413	0.294	84	1.20	0.25
Inlet compressor	97	283	101	287	413	0.294	85	1.19	0.25
Outlet compressor	207	353	335	405	532	0.294	324	2.04	0.86
Inlet diffuser	218	358	278	384	511	0.294	229	2.11	0.60
Outlet diffuser	271	382	277	384	511	0.294	72	2.47	0.18

Table 4.2. Modeling results at an engine speed of 70,000 RPM.

Figure 4.2 presents the stagnation temperature and pressure at outlet of the diffuser as a function of engine speed for both measured values from the test run and predicted values from the modeling.

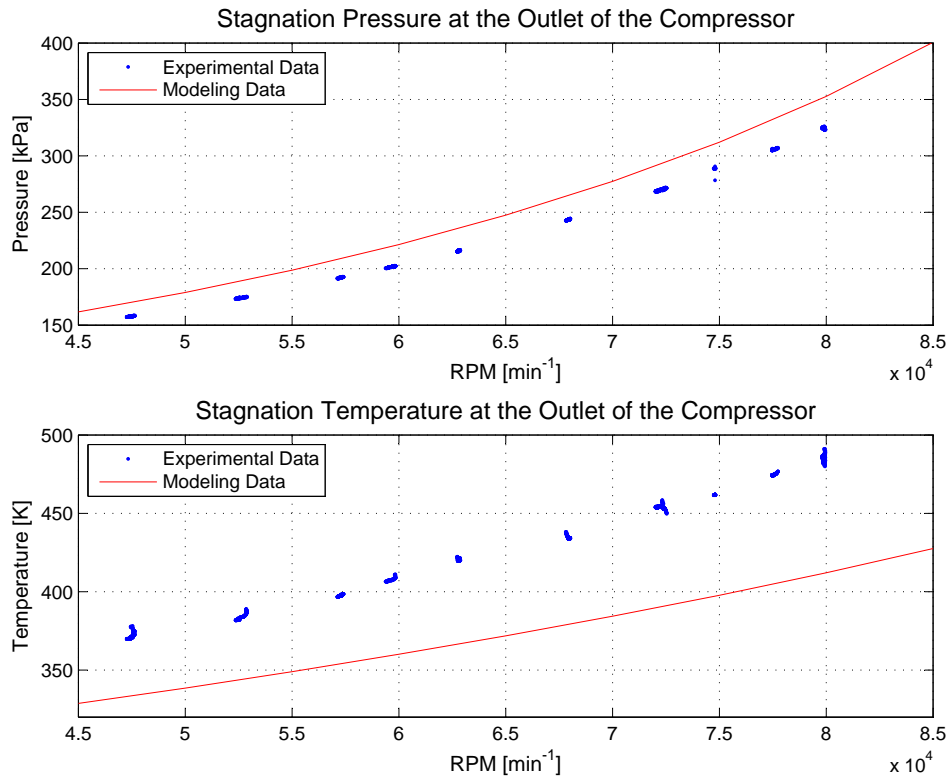


Figure 4.2. Stagnation temperature and pressure at outlet of the compressor for measured and predicted values.

If the model is evaluated with respect to static pressure at 85,000 RPM a predicted static pressure ratio of 4.0 at 85,000 RPM is revealed. This disagrees with the value of 3.4 at 87,000 RPM provided by the manufacturer *Turbine Technologies (2012)*. This may be explained by the fact that some losses associated with leakage flow and mixing flow have been neglected in the modeling. By implementing more losses it is expected that the predicted pressure will decrease while the predicted temperature will increase. Hereby, the deviation between predicted and measured values is reduced as seen from figure 4.2. In general, it must be kept in mind that the compressor modeling is based on two dimensional velocity

triangles, which neglects any swirl and change of velocity in the third dimension. This assumption definitely also contributes to the high compressor performance. In general, it appears how the predicted pressure and temperature follow the tendency of the measured data and remain in the same range. When the simplicity of the modeling is considered the modeling results are rather satisfactory and the compressor model is considered valid with respect to thermodynamic quantities. As a result, the predicted values can be used as input to the combustion model.

#### 4.2.1 Losses in the Compressor

It should be noticed from table 4.2 how the stagnation enthalpy decreases from impeller outlet to diffuser inlet. This is an error in the modeling as the stagnation enthalpy must not change at a point where no work is added or subtracted. However, it is due to the way the incidence loss is modeled. According to literature, the incidence loss is defined as a loss of tangential velocity, which is explained in details in subsection 3.4.1. With respect to vector lengths, the change of absolute velocity will always be bigger than that of the tangential. This also means that since the amount of kinetic energy associated with incidence loss is calculated from the change of tangential velocity, it does not correspond to the overall change of kinetic energy related to the absolute velocity. As a result, the modeling of incidence loss will cause an increase in stagnation enthalpy at points where the absolute velocity is increased due to incidence, and there will be a decrease in stagnation enthalpy at points where the absolute velocity is reduced due to incidence. The change of stagnation enthalpies depends strongly on the size of velocities at the point where the incidence occurs. This explains the fact that the stagnation enthalpy appears to be constant from nozzle outlet to impeller inlet even though the absolute velocity increases. At impeller outlet, where the velocity is relatively high, the incidence loss has a bigger impact, and thus the change of stagnation enthalpy is bigger, which can also be seen from table 4.2. Here the absolute velocity is reduced and so is the stagnation enthalpy.

The impact of the way incidence losses is modeled are sketched for inlet of impeller and diffuser with figure 4.3. The figures are made in the modeling by drawing the velocity vectors at three different engine speeds. Hereby, it is possible to analyse the variation in flow angle and compare it with the blade angle. At the inlet to the impeller, the flow angle is the angle between the axial direction and the relative velocity (the red line) and at the inlet to the diffuser the flow angle is between axial and the absolute velocity (the blue line). The blade angles are illustrated with the black lines. It is clear from the figures that the change of tangential velocity is bigger at diffuser inlet than at impeller inlet, which explain the changes in stagnation enthalpies.

As described in subsection 3.4.1, incidence losses, friction losses and disk friction have been implemented in the compressor modeling. Figure 4.4 illustrates how the different losses in the impeller and the diffuser are predicted to vary with RPM. The losses are shown relative to the real work and a logarithmic scale is used in order to see the small variations.

Figure 4.4 shows that the main loss in the compressor is the incidence loss at inlet of the diffuser, which forms between 2 and 8 % of the total work consumed by the compressor. In the impeller, the main loss is the disk friction, which consumes about 1 % of the compressor work. The incidence loss at impeller inlet is below 0.3 %, which agrees with the previous discussion about the modeling of incidence losses. From figure 4.4 it appears how friction in the blade rows could easily be neglected for a small engine like the SR-30 engine, since the blade rows are short.

It appears from figure 4.4, how none of the incidence losses approach zero anywhere in the operational range of speeds of the SR-30 engine. In other words this means that neither of the blades are designed in order to minimise the incidence loss at some design flow. This is surprising and will be discussed further when also the combustion and turbine results have been presented.

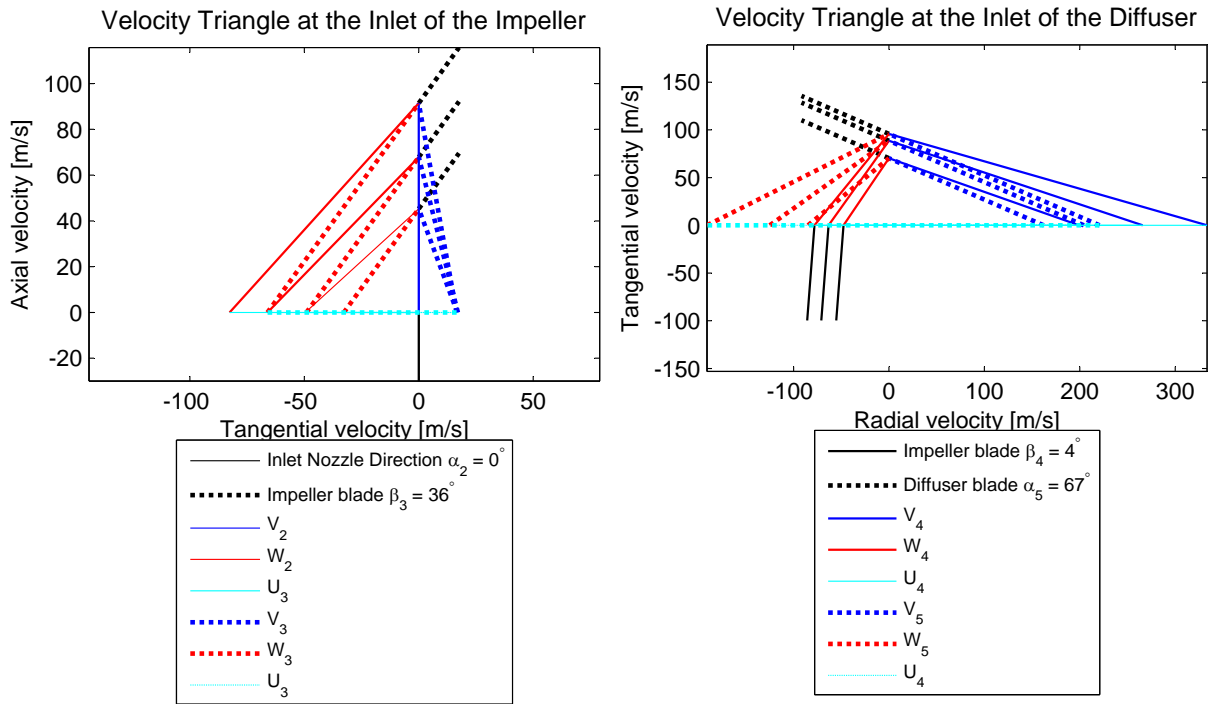


Figure 4.3. Velocity triangle at the inlet of the impeller at three different engine speeds.

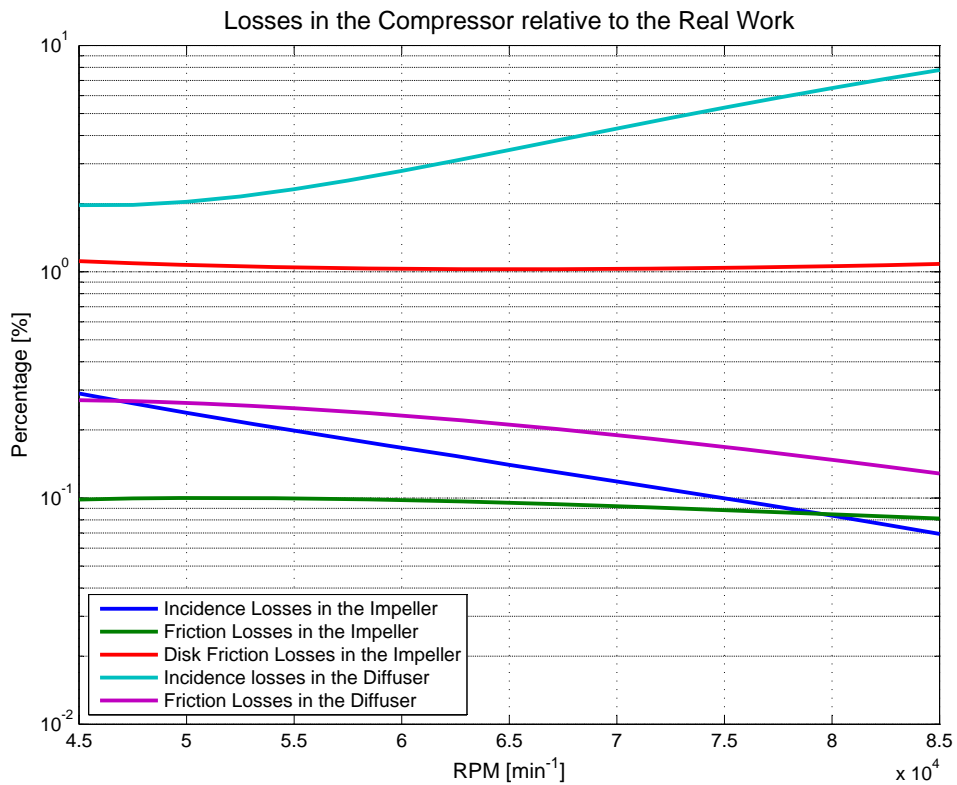


Figure 4.4. Modeled losses in the compressor as a function of RPM.

### 4.3 The Combustion Chamber

In the test stand the stagnation temperature and the static pressure are measured at the combustion outlet and the results are to be compared with predicted values. Table 4.3 extends the modeling results with values from the combustion outlet.

Component	P	T	P <sub>0</sub>	T <sub>0</sub>	h <sub>0</sub>	m	V	ρ	Mach
	[kPa]	[K]	[kPa]	[K]	[kJ/kg]	[kg/s]	[m/s]	[kg/m <sup>3</sup> ]	[.]
Inlet nozzle	101	287	101	287	413	0.294	14	1.23	0.04
Outlet nozzle	97	286	101	287	413	0.294	84	1.20	0.25
Inlet compressor	97	283	101	287	413	0.294	85	1.19	0.25
Outlet compressor	207	353	335	405	532	0.294	324	2.04	0.86
Inlet diffuser	218	358	278	384	511	0.294	229	2.11	0.60
Outlet diffuser	271	382	277	384	511	0.294	72	2.47	0.18
Outlet combustion	271	890	278	896	1055	0.2978	115	1.06	0.20

Table 4.3. Modeling results upstream from combustion chamber evaluated at an engine speed equal to 70,000 RPM.

It appears how pressure through the combustion chamber is constant and only the temperature increases due to the combustion. The modeled static pressure from the combustion equals that of the compressor outlet. Figure 4.5 illustrates the measured temperature from the test and the estimated temperature from CEA NASA.

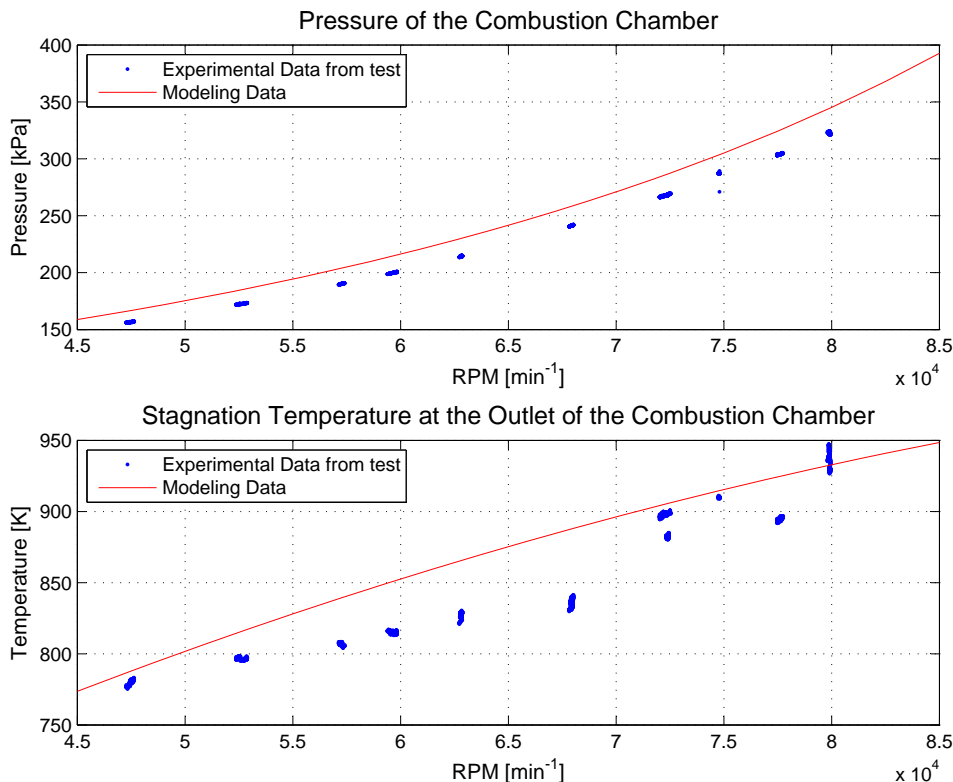


Figure 4.5. The outlet temperature in the combustion chamber.

The figure shows that the static modeled and measured pressure have a fine agreement. Notice that the pressure curves are very similar to the ones of the compressor. This agrees with the modeling which set the static pressure outlet of the compressor and the combustion chamber equal. The figure also shows

how the measured temperature is in the same range as the estimated temperature from CEA NASA. CEA NASA calculates a temperature that deviates with a maximum of around 60 K from the measured data. The modeled temperature is a function of inlet pressure, temperature and AF ratio, which are determined in the compressor model. The output pressure in the compressor model is higher than the measured one and the outlet temperature is lower than the measurements and thus it is examined whether a higher temperature and a lower pressure as input to the combustion chamber will lower the adiabatic flame temperature. However, running the CEA NASA program with these modifications reveals a higher adiabatic flame temperature, which is not desired.

As mentioned in section 2.2 the adiabatic flame temperature decreases when the excess air ratio is increased. As the excess air ratio is closely related to the AF ratio it is expected that the high flame temperature is related to a high AF ratio. However, lowering the AF ratio with 5 % only lowers the adiabatic flame temperature with approximately 2 % and the AF ratio alone can not explain the high outlet temperature from the combustion chamber. The fuel used in CEA NASA to model the combustion chamber is assumed to be JP-4. This assumption may cause the modeled adiabatic flame temperature from the combustion chamber to deviate from the measurements as the fuel used for the measurements and in the model may not be similar.

It can be seen from figure 4.5 at around 70,000 RPM, how the measured temperature does not have a smooth evolution with RPM. The jumps that occur in the measured data may be due to the dynamic behavior of the flame within the combustion chamber, and thus some deviation between the measured and the modeled temperature may be expected (Condra, 2012). Furthermore, the exact location of the temperature measurement in the combustion chamber is unknown and the reference point for the temperature comparison might not be the same which makes the comparison invalid.

Since the range of the measured temperature matches that of the modeled temperature and the dynamic behavior of the flame might cause the flame temperature to deviate from the model, it is concluded that the combustion model is validated and thus the turbine results can now be evaluated.

#### 4.4 The Turbine Results

Stagnation pressure and temperature are measured in the turbine outlet and since energy is extracted in the rotor a decrease in these measurements compared to the combustion outlet is expected. Table 4.4 presents the modeling results upstream from the turbine outlet at an engine speed of 70,000 RPM.

Component	P	T	P <sub>0</sub>	T <sub>0</sub>	h <sub>0</sub>	m	V	ρ	Mach
	[kPa]	[K]	[kPa]	[K]	[kJ/kg]	[kg/s]	[m/s]	[kg/m <sup>3</sup> ]	[.]
Inlet nozzle	101	287	101	287	413	0.294	14	1.23	0.04
Outlet nozzle	97	286	101	287	413	0.294	84	1.20	0.25
Inlet compressor	97	283	101	287	413	0.294	85	1.19	0.25
Outlet compressor	207	353	335	405	532	0.294	324	2.04	0.86
Inlet diffuser	218	358	278	384	511	0.294	229	2.11	0.60
Outlet diffuser	271	382	277	384	511	0.294	72	2.47	0.18
Outlet combustion	271	890	278	896	1055	0.2978	115	1.06	0.20
Inlet turbine stator	270	889	278	896	1055	0.2978	125	1.06	0.21
Outlet turbine stator	188	812	276	896	1057	0.2978	434	0.80	0.77
Inlet turbine rotor	188	811	306	920	1081	0.2978	493	0.81	0.87
Outlet turbine rotor	155	770	168	786	933	0.2978	186	0.70	0.34

Table 4.4. Modeling results upstream from turbine outlet evaluated at an engine speed equal to 70,000 RPM.

As expected, the static temperature and pressure decrease in the turbine according to table 4.4. But the fact that the stagnation quantities all increase significantly in the gap between stator outlet and rotor

inlet must be noticed. This issue will be discussed in section 4.6.1. The Mach numbers predicted with the modeling are similar to the modeling done by *Witkowski et al. (2003)*. According to their report the Mach numbers at stator inlet, rotor inlet and rotor outlet is 0.19, 0.98 and 0.25 respectively at an engine speed of 70,000 RPM.

Figure 4.6 illustrates the stagnation temperature and pressure at outlet of the turbine as a function of RPM for both measured and predicted values.

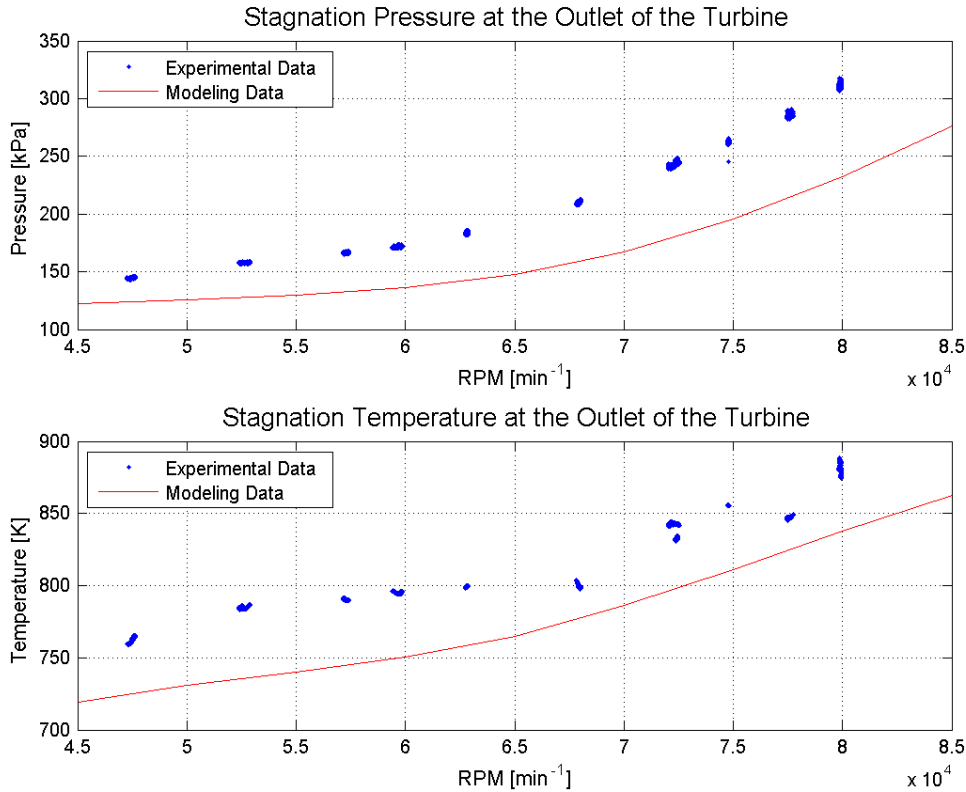


Figure 4.6. The turbine outlet temperature and pressure as a function of RPM.

From figure 4.6 it appears how the predicted pressure is lower than the measured stagnation pressure. At first sight this disagrees with the fact that the predicted pressure is too high in the compressor. But when the impact of a high compressor pressure is analysed, it is found how a too low velocity out of the turbine could be the explanation. The velocity is defined from the conservation of mass flow, and with a high static pressure, the density goes up and the velocity goes down. By decreasing static pressure out of the compressor, the dynamic contribution to the stagnation pressure out of the turbine is then higher, which may improve the predicted results. On the other hand, an increase in velocity affects static pressure in a reductive way, and since the different quantities are closely related it is difficult to give an exact answer to the issue of a predicted stagnation pressure lower than the measurements.

The predicted stagnation temperature is, according to figure 4.6, also lower than that measured in the test runs. This deviation could be explained by the lack of modeling mixing and leakage losses, but the stagnation temperature will also increase if the velocity is increased as mentioned just above with respect to the pressure. In general, the tendency of both predicted pressure and predicted temperature is similar to the measured values, which is satisfactory when the simplicity of the model is considered. As with the compressor, the turbine model is only based on two dimensional velocity triangles. When the third velocity component is neglected, the turbine work may quite likely be overestimated and thus the drop in stagnation quantities across the turbine rotor will be too high. This hypothesis matches the fact that the predicted stagnation quantities are lower than those measured.

#### 4.4.1 Losses in the Turbine

As for the compressor, friction in the blade rows, incidence losses and disk friction have been modeled in the turbine. Figure 4.7 illustrates how the different losses in the rotor and stator are predicted to vary with engine speed. Once again the losses are shown relative to the real turbine work and a logarithmic scale is used to show the variation with RPM.

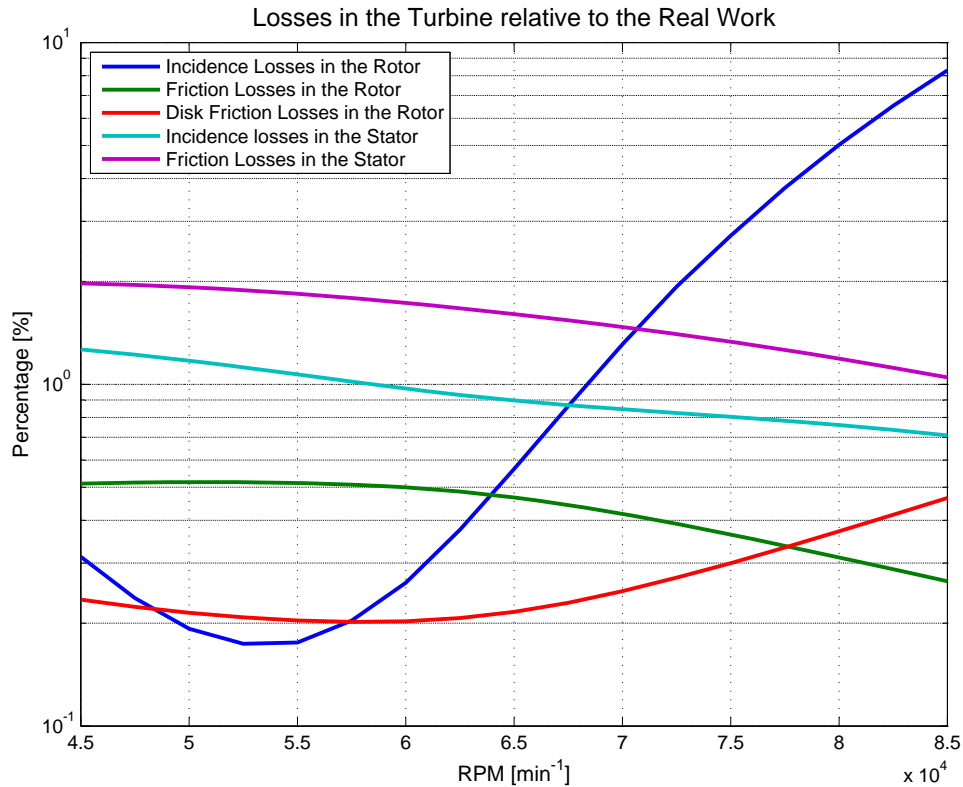


Figure 4.7. Losses in the turbine as a function of RPM.

The real turbine work is defined as the ideal work minus friction losses. According to figure 4.7 it is the incidence loss at inlet of the rotor, which has the major impact. The remaining losses are in the range of 0.1 to 2 % relative to the real turbine work. The incidence loss in the rotor goes just above 8 % at 85,000 RPM and when considering the impact this incidence loss has to the predicted results in table 4.4, it appears that the modeling of this incidence loss is somehow incorrect. The stagnation enthalpy increases in the gap between stator outlet and rotor inlet, which is incorrect as no work is added in this gap. As mentioned in subsection 4.2.1 about compressor losses, the approach to the incidence modeling seems incorrect at points where the absolute velocity is increased due to the incidence loss. This issue is rather important and therefore discussed in details in section 4.6 about general modeling results.

#### 4.5 The Exhaust Nozzle Results

The exhaust nozzle is a converging nozzle in which the flow is accelerated and for which the maximum Mach number is unity. Since the nozzle flow is subsonic, the static outlet pressure is atmospheric. However, recall that there is an exhaust pipe mounted at the end of the exhaust nozzle, but with a little gap in between, where surrounding air can mix with the flue gas. Since this pipe is neither converging or diverging, the static pressure at outlet of the exhaust nozzle can only be set equal to atmospheric, when the exhaust pipe is considered free of friction.

Table 4.5 presents the predicted properties for the outlet of the exhaust nozzle at 70,000 RPM. This table

reveals how the static pressure at outlet of the nozzle is assumed to be atmospheric in the modeling. Furthermore, it appears how the stagnation temperature and thus the stagnation enthalpy is assumed constant across the nozzle.

Component	P	T	P <sub>0</sub>	T <sub>0</sub>	h <sub>0</sub>	m	V	ρ	Mach
Inlet nozzle	101	287	101	287	413	0.3012	14	1.23	0.04
Outlet nozzle	97	286	101	287	413	0.3012	48	1.22	0.14
Inlet compressor	97	283	101	287	413	0.3012	85	1.19	0.25
Outlet compressor	207	353	335	405	532	0.3012	324	2.04	0.86
Inlet diffuser	218	358	278	384	511	0.3012	229	2.11	0.60
Outlet diffuser	271	382	277	384	511	0.3012	72	2.47	0.18
Outlet combustion	271	890	278	896	1055	0.3050	114	1.06	0.19
Inlet turbine stator	270	889	278	896	1055	0.2978	125	1.06	0.21
Outlet turbine stator	188	812	276	896	1057	0.2978	434	0.80	0.77
Inlet turbine rotor	188	811	306	920	1081	0.2978	493	0.81	0.87
Outlet turbine rotor	155	770	168	786	933	0.2978	186	0.70	0.34
Outlet exhaust nozzle	101	752	120	786	933	0.2978	4	0.47	0.51

Table 4.5. The modeling results at an engine speed of 70,000 RPM for the outlet of the exhaust nozzle are highlighted.

The main product of a turbojet engine is obviously thrust. The SR-30 engine is mounted in the test stand in such a way that the thrust can be measured. Figure 4.8 presents the measured thrust along with the predicted thrust as a function of RPM.

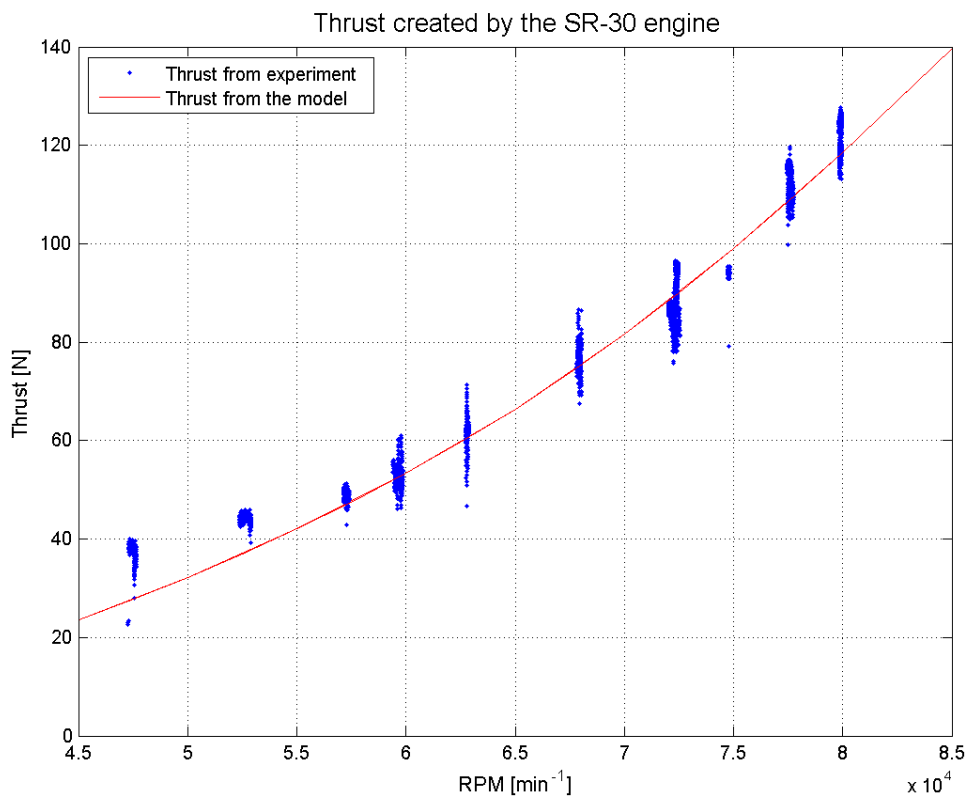


Figure 4.8. The predicted and measured thrust as a function of RPM.

Thrust depends on mass flow and outlet velocity only, and from figure 4.8 it can be concluded that the

predicted thrust matches the measured thrust very well. Based on that, it seems that the modeled mass flow throughout the model and the velocity at outlet of the exhaust nozzle are quite accurate. This is kept in mind when analysing figure 4.9, which presents the stagnation pressure and temperature as a function of RPM with respect to both measured and predicted values.

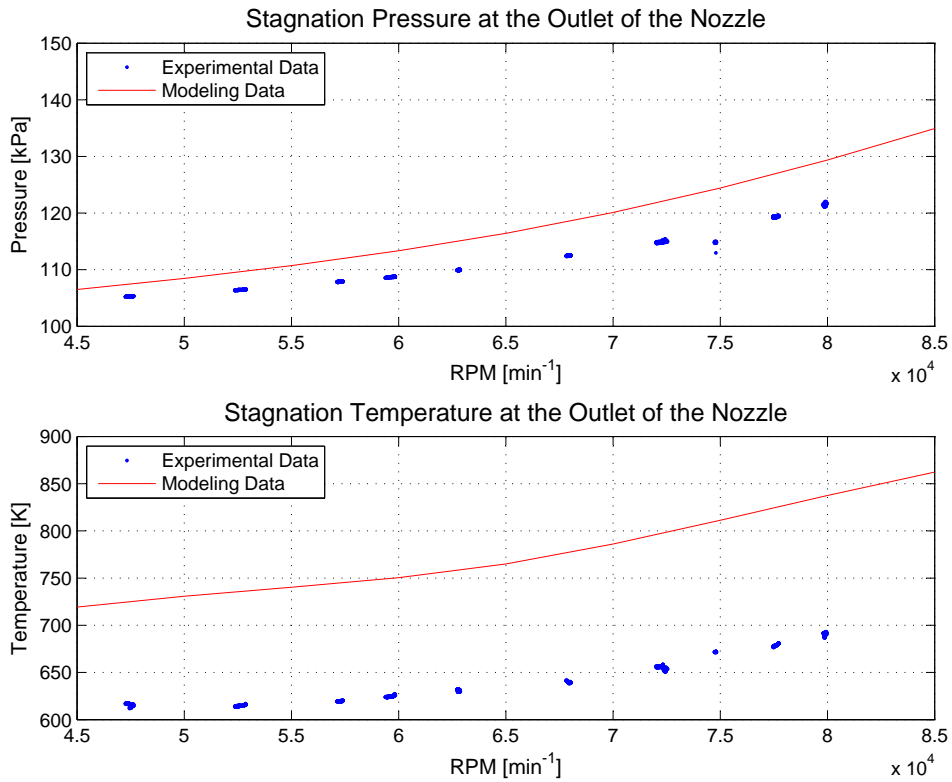


Figure 4.9. The outlet stagnation temperature and pressure of the exhaust nozzle as a function of RPM.

Measured stagnation pressure is, according to figure 4.9, slightly lower than predicted. From figure 4.8 it seemed that the velocity at outlet of the nozzle is modeled with a good accuracy. This means that the dynamic part of the stagnation pressure, presented in figure 4.9, should be accurate. Based on that, it must be the static part of the predicted stagnation pressure that is too high. Recall that the static pressure in the model is set equal to atmospheric at outlet of the exhaust nozzle, and thus it seems from the measurements that the static pressure at this point in reality is lower than atmospheric. This agrees with the fact that surrounding air is actually entering the exhaust pipe, which was concluded at the experiments presented in section 3.5. However, with a static pressure at inlet of the exhaust pipe it means that there must be a pressure rise across the exhaust pipe in order to obtain atmospheric pressure at outlet of the exhaust pipe. This does not seem correct since the flow in reality will experience some friction in the exhaust pipe and thus a pressure drop across the pipe is expected.

From the above given considerations it is difficult to explain the deviation between predictions and measurements of the stagnation pressure given in figure 4.9. Any conclusion will be associated with some guesses and as a result, it is left for future work to perhaps measure the static pressure at outlet of the exhaust nozzle. Thereby, the dynamic pressure and thus the velocity at this point could be defined. This would enable a validation of the conclusion made from figure 4.8, which was that thrust and thereby mass flow and velocity at outlet of the exhaust pipe are modeled correctly.

A validation of the mass flow would be convenient, since the model highly depends on mass flow. Figure 4.9 also presents the measured and predicted stagnation temperature as a function of RPM. There is a big deviation from around 100 to almost 150 K, which is not satisfactory. Such a deviation is reduced if

the mass flow is increased in the model. Apart from that, it is unknown why the predicted stagnation temperature is higher than the measured value.

## 4.6 General System Results

The individual results of each submodel might be satisfactory, but if for instance the work extracted in the turbine is not sufficient to drive the compressor, then the modeling results do not make sense when combined. This section will present relevant discussions about the engine as a united system and a discussion about the way of modeling incidence losses in the compressor and turbine.

In the SR-30 specifications given by the manufacturer, it is stated that the SR-30 engine can reach a maximum speed of 87,000 RPM. In the test runs it was not possible to exceed 80,000 RPM.

### Thrust

The SR-30 specifications also stated a maximum thrust of 180 N, but the highest thrust measured was just below 130 N at 80,000 RPM. At this speed the modeling predicts a thrust of 119 N, which deviates 8 % from the measurements.

### Mass Flow and Fuel Consumption

The SR-30 test stand does not provide information about the mass flow of air at inlet. Therefore, experiments have been made in order to define the mass flow of air. These measurements revealed a mass flow of air into the inlet nozzle of  $0.35 \text{ kg/s}$  at 80,000 RPM, whereas the mass flow according to the specification should be  $0.5 \text{ kg/s}$  at 87,000 RPM. The specific fuel consumption is according to the specification  $6 \text{ g/s}$ , whereas it is modeled to be  $4.6 \text{ g/s}$  and measured to be  $4.5 \text{ g/s}$  at 80,000 RPM.

### Compressor Pressure Ratio

The static pressure measured at 80,000 RPM in the combustion chamber is 310 kPa relative to atmospheric, and thus the pressure ratio across inlet nozzle and compressor is 3.1. To compare, this pressure ratio of the model is predicted to be 3.4 at 80,000 RPM. The specifications give a pressure ratio at maximum speed (87,000 RPM) of 3.4.

The specifications are considered inaccurate due to rounded numbers that does not reflect the measurements. Meanwhile, it is the modeling results that are relevant and they seem to match the measurements with respect to thrust and fuel flow, whereas the predicted pressure rise across the compressor is too high.

## Compressor and Turbine Work

Figure 4.10 illustrates that the predicted turbine work actually does match the compressor work. Actually, the compressor work is as much as 28 % lower than the turbine work at 65,000 RPM. This difference seems high and agrees with the fact that the modeling may overestimate the turbine work. This was concluded in section 4.4 in order to explain that the predicted stagnation temperature and pressure are lower than the measured values.

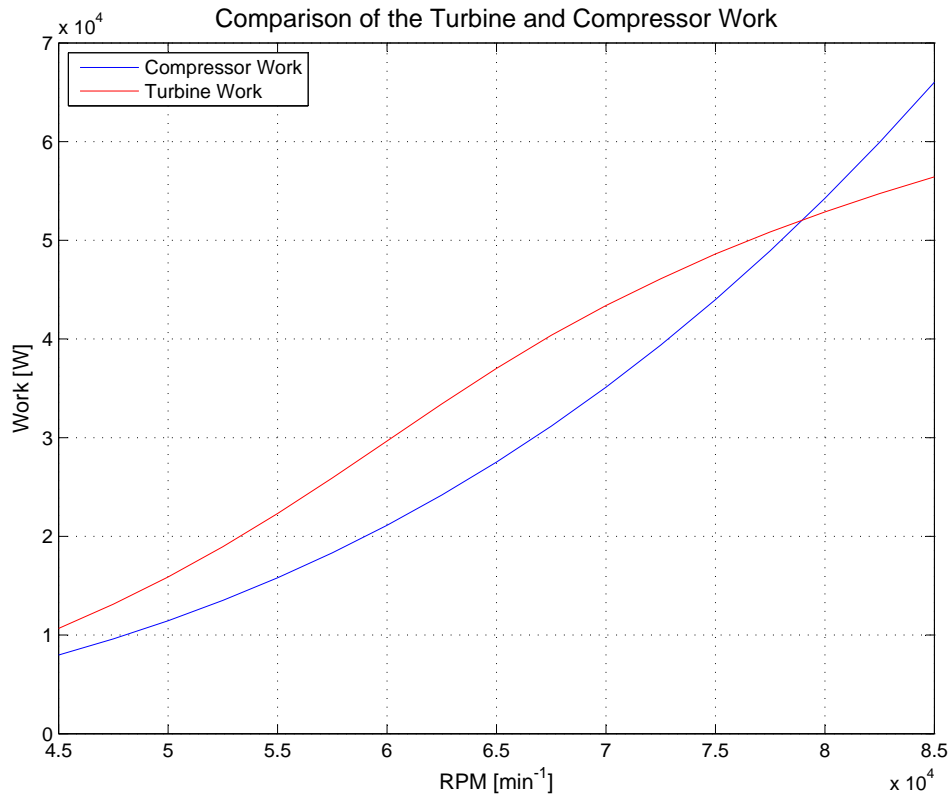


Figure 4.10. Predicted work of the turbine and the compressor as a function of RPM.

Another interesting observation from figure 4.10 is that the turbine work is lower than the compressor work at engine speeds higher than 77,000 RPM. To some extent this agrees with the fact that it is not possible to accelerate the SR-30 test engine to more than just below 80,000 RPM.

### 4.6.1 Issues Related to Incidence Modeling

At the evaluation of both compressor and turbine results it appears that there is an issue related to the approach of modeling incidence losses. As mentioned, the incidence loss is defined from the change of tangential velocity. Since the change of absolute velocity is bigger than that of the tangential component, there will be a change of stagnation enthalpy due to this way of modeling the incidence loss. According to *Ferguson (1963)* a flow will accelerate into a blade row if the flow angle is negative relative to the blade angle and decelerate if the flow angle is positive relative to the blade angle. This means that when the model predicts an acceleration at inlet of for instance the rotor, it seems correct, since the flow angle is on the suction side of the airfoil relative to the blade angle. However, the fact that the stagnation enthalpy actually increases at such a gap has to be incorrect, since no work is added. As a result, it would improve the modeling if the approach is modified so that the stagnation enthalpy is at least kept constant at a gap where the flow accelerates due to incidence. This could be done by defining the incidence loss from the change of absolute velocity rather than only the tangential components. Hereby, the first issue to be looked at in future work is formulated.

Figure 4.11 illustrates the difference between the flow and blade angle as a function of engine speeds for the different inlets where incidence loss is implemented. This figure is made to illustrate how the blades do not seem to be designed in order to reduce incidence loss at some design flow. This appears from the fact that the angles given in figure 4.11 do not approach zero within the relevant range of engine speeds.

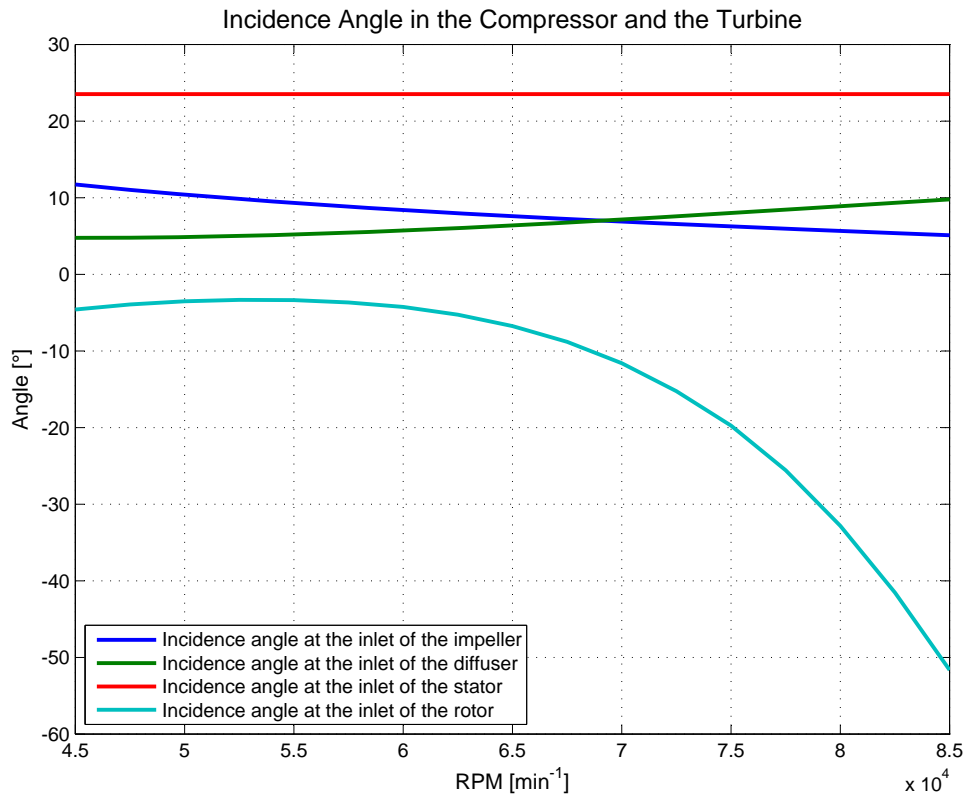


Figure 4.11. Predicted difference between flow and blade angle at the inlets where incidence losses have been implemented.

One would expect that the blades have been designed to reduce incidence losses, but the optimum flow angle may have been sacrificed in order to ensure either an acceleration or deceleration into the particular blade row at all engine speeds. For instance as mentioned in section 2.3, it is very important to avoid diffusion in the turbine blade rows, as diffusion will introduce big losses. In order to avoid deceleration at all engine speeds it may have been chosen to angle the blades at rotor inlet so that the flow angle is always negative relative to the blade angle. Thereby, the flow will accelerate into the blade row and diffusion is avoided. With this in mind, there is however an optimum speed for the incidence loss at inlet of the turbine rotor at around 55,000 RPM. This speed is also close to the optimum for the incidence loss at diffuser inlet and as mentioned previously, incidence losses at these two particular inlets form the major losses in the model. As a result, the blade angles may have been chosen from a combination of reducing incidence losses and ensuring a stable flow into the particular blade row. (Ferguson, 1963)

## 4.6.2 Changes in Stagnation Enthalpy

Validation of the modeling is a matter of checking that the results reflect what will happen in the SR-30 engine in reality. Specific stagnation enthalpy of a control will only change if work is either added or subtracted from the control volume. Thus, the modeling should only predict a change of specific stagnation enthalpy across the impeller, the combustion chamber and the turbine rotor. To check this hypothesis, figure 4.12 presents the predicted specific stagnation enthalpy of the flow at an engine speed of 70,000 RPM.

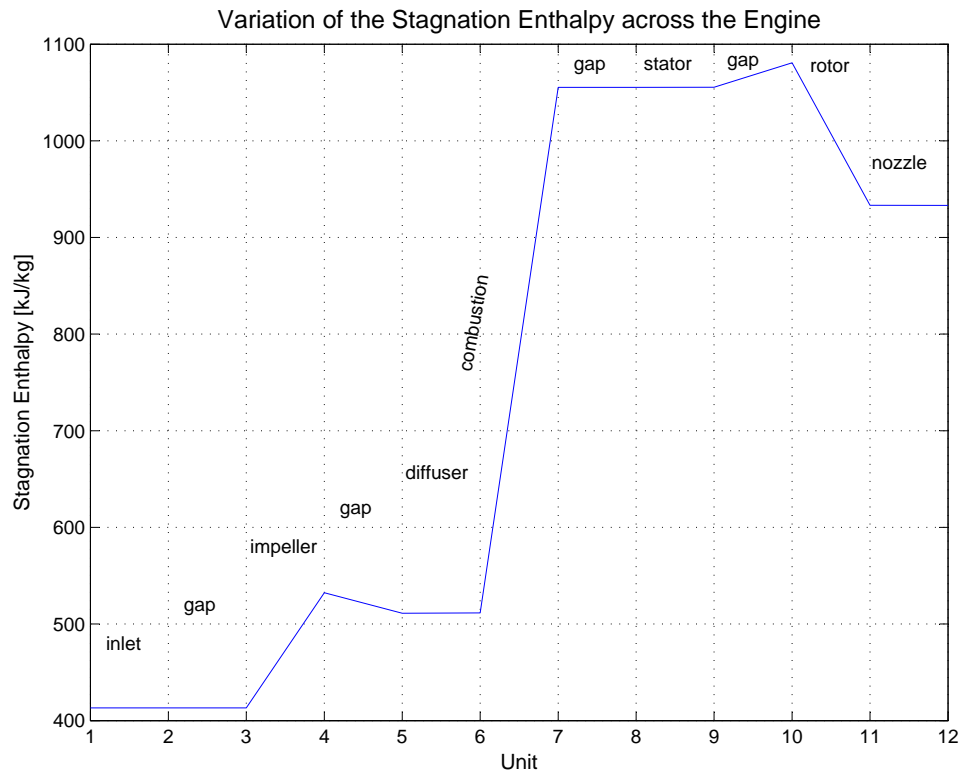


Figure 4.12. Change of specific stagnation enthalpy throughout the SR-30 modeling.

Firstly, the stagnation enthalpy increases across the impeller with a value corresponding to the decrease across the turbine rotor. In addition, the stagnation enthalpy increases significantly in the combustion chamber, where fuel is added. Though, the impeller to diffuser gap and the stator to rotor gap do not have constant stagnation enthalpies. This is due to the mentioned issue about modeling of incidence losses, which is already mentioned in the previous subsection 4.6.1. At the remaining points, including the two nozzles, the diffuser and the stator, there is no change in stagnation enthalpy and apart from the incidence modeling, the model seems valid with respect to specific stagnation enthalpy.

## 4.6.3 Compressor and Turbine Efficiency

The total-to-total efficiency of the compressor and turbine are determined using equations (3.33) and (3.43) presented in the modeling chapter. The efficiencies are evaluated at 70,000 RPM in order to compare with efficiencies determined by *Witkowski et al. (2003)* at this speed. The compressor efficiency is calculated from the modeling results to be 98 % which is high compared to an efficiency of 72 % determined by *Witkowski et al. (2003)*. The modeled turbine efficiency is 98.9 % which compared to 79 % determined by *Witkowski et al. (2003)* is high as well. Efficiencies close to unity means that the real and ideal stagnation enthalpies are similar.

The losses implemented throughout the model will affect the efficiencies, since the real and ideal

stagnation enthalpies are indirectly determined from the real and ideal compressor and turbine work. If more losses were modeled the difference between real and ideal stagnation enthalpy would increase, and thus the efficiencies would decrease towards more reliable values.

For the compressor the real and ideal enthalpies are determined from the inlet nozzle and compressor outlet temperatures and pressures and deviations in these parameters will affect the efficiency. The results from the modeling of the inlet nozzle and compressor are shown in figures 4.1 and 4.2 respectively. The modeled outlet static pressure of the inlet nozzle and the compressor outlet temperature were underestimated compared to the measurements, while the inlet nozzle outlet temperature and the compressor pressure were overestimated. Even though it was concluded that the inlet and the compressor models are valid, the modeled values affects the efficiency calculation. For comparison the efficiency is calculated based on the measurements from the test run.

To determine the efficiency, the inlet and compressor outlet stagnation parameters must be known. The measured parameters at outlet of the inlet nozzle are static quantities and the velocity must be known at this point to determine the stagnation quantities. Equations (3.1), (3.8) and (3.10) presented in the modeling chapter are used to determine the velocity and the stagnation properties. The area, density and pressure are known and the mass flow, determined by means of measurement is assumed to be accurate.

In the compressor outlet the stagnation temperature and pressure are measured directly. The isentropic stagnation temperature is determined using equation 3.7. With this approach the efficiency is calculated to 59.3 %, which is 39 % lower than the measured efficiency. The measured temperatures and pressures are approximated values estimated from figure 4.1 and 4.2. Small variations in these estimations affects the efficiency and it is concluded that the modeled efficiency is highly dependent of the modeled temperatures and pressures. Therefore, the pressure ratio should be used as the crucial parameter in order to analyse validity of the compressor model.

The measured turbine efficiency is found for comparison with the modeled efficiency. The approach for determining the measured turbine efficiency is the same as for the compressor. The efficiency depends on the stagnation temperature and pressure in the combustion outlet and the turbine outlet. The static pressure is measured at the combustion outlet along with the stagnation temperature whereas the outlet parameters from the turbine are stagnation quantities. In order to determine the turbine efficiency from the measurements, iterations must be used since the density and thereby velocity can not be determined directly from the combustion parameters. The iteration method is described in section 3.2.2 and the Matlab script used to find the efficiencies can be found in appendix F.

The turbine efficiency determined from measurements is 90.7, which is still high compared to the efficiency determined by *Witkowski et al. (2003)*. As for the compressor, the efficiency is highly dependent on the stagnation temperatures and pressures, and small variations affects the efficiency calculation.

#### 4.6.4 Degree of Reaction

The relevance of defining the degree of reaction for a turbine was presented in subsection 2.3 along with a hypothesis of R being close to zero. Furthermore, a formula for calculating the degree of reaction was presented in subsection 3.6.2. This particular formula is however modified since the increase in stagnation enthalpy in the gap between stator and rotor affects the calculations. The modification is presented in equation 4.1.

$$R = \frac{h_9 - h_{11}}{h_8 - h_{11}} = \frac{h_{10} - h_{11}}{h_7 - h_9 + h_{10} - h_{11}} \quad [\cdot] \quad (4.1)$$

Figure 4.13 illustrates the degree of reaction as a function of RPM calculated from equation (4.1).

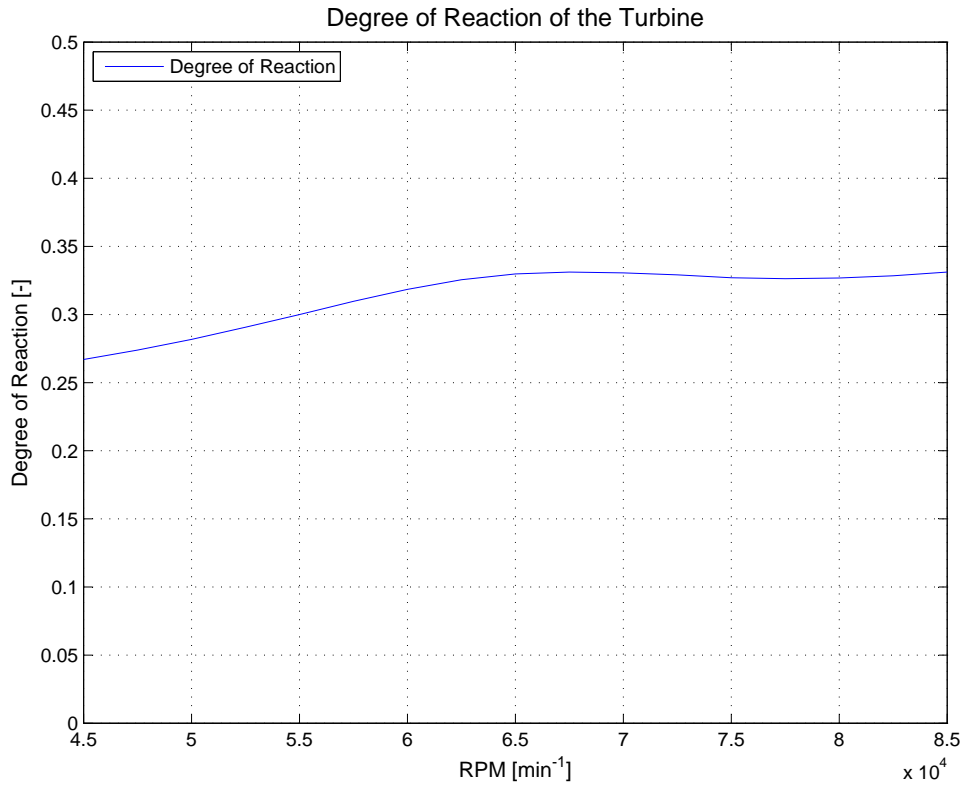


Figure 4.13. Degree of reaction for the single stage axial turbine in the SR-30 turbine.

It appears how the reaction stage is rather constant around 0.3 according to the modeling. It is not possible to compare the reaction stage with measurements, since there are no data available for the gap between stator and rotor. It has been mentioned previously that the turbine work is expected to be overestimated. By decreasing the enthalpy change across the rotor, it can be seen from equation (4.1) that  $R$  is reduced. Thereby, the result goes towards the hypothesis of a reaction stage closer to zero than 0.5.

Throughout this chapter, it is concluded that the model predicts the tendencies of the measurements and that the modeling results are in the same range as the measurements. However, there are several deviations between the predicted and measured values, and as a result the modeling cannot be validated to predict the performance with high accuracy. A highly accurate modeling was the aim of the project, but it has not been possible to fulfill this target. The negative impact of neglecting the third velocity component by using two dimensional velocity triangles is expected significant, when the approach is applied for small scale engines like the SR-30 (Dixon and Hall, 2010). Boundary layers in the blade rows will have a higher impact when the dimensions are small compared to large scale engines. As a result, the inaccuracy of the SR-30 modeling is due to the fact that two dimensional velocity triangles overestimate performance of small scale engines. Based on this it is the belief that the modeling approach applied throughout this project is valid and accurate for turbojet engines at a larger scale than the SR-30.



# Conclusion 5

---

A first step of combining biofuels and aviation is, according to interest groups, engine and fuel testing rather than flight testing. A validated model of the examined turbojet engine is required for engine testing and thus the aim of the project is to make a valid and accurate model of the SR-30 turbojet engine. The model, which is made in Matlab, is based on compressible and isentropic flow relations and the performance of both compressor and turbine is modeled by the use of two dimensional velocity triangles. In the modeling the only inputs are the RPM, the mass flow of air entering the engine and the inlet thermodynamic conditions. Test runs of the SR-30 engine have provided basis for modeling validation.

*Turbine Technologies (2012)* has provided general specifications for the SR-30 engine, but it is the conclusion that these specifications deviate from the measurements made during test runs and thus they have only been used as indicators in the modeling. During the test runs the engine could not run above 80,000 RPM whereas the specifications indicate a maximum RPM of 87,000. Specific fuel consumption is, according to the specifications 6 g/s at 87,000 RPM, whereas it is measured and modeled at 80,000 to be 4.5 and 4.6 g/s respectively. Likewise, the mass flow of air entering the engine is 0.5 kg/s at 87,000 RPM according to the specifications, whereas it is measured and thus modeled to be 0.35 kg/s at 80,000.

Comparison of predicted and measured performance reveals a satisfactory modeling of the inlet nozzle, although no friction losses are considered. The deviations observed are at outlet below 2 kPa and 3 K for static pressure and temperature respectively. The compressor modeling accounts for slip and deviation, incidence losses, disk friction and friction in the blade rows. The incidence loss at diffuser inlet is predicted to consume 7 % of the compressor work at 80,000 RPM. Remaining losses are in the range of 0.1 to 1 %. At 80,000 RPM measurements reveal a static pressure ratio at compressor outlet of 3.1, whereas the modeling predicts 3.4. The predicted stagnation temperature at compressor outlet is lower than the measurements and with the higher pressure ratio in mind, it seems that not enough losses have been implemented and compressor performance is overestimated. In addition, the compressor efficiency is modeled to be 98 % and from measurements calculated to be 59 %. This seems like a significant deviation, but since the efficiencies are rather inaccurate, the pressure ratio of the compressor should be considered as the crucial parameter for model validity.

The combustion chamber is modeled in CEA NASA with JP-4 representing the jet fuel. Test runs measuring the inlet air mass flow and the fuel consumption are used to determine the AF ratio which is implemented in CEA NASA. The modeling predicts an output stagnation temperature in the same range as measurements, which is between 780 and 950 K dependent on engine speed. The combustion is modeled to be in equilibrium, since kinetics and the dynamic behavior of the flame within the combustion chamber is beyond the scope of this report.

The modeling of the single stage axial turbine implements the same losses as for the radial compressor. This does not seem sufficient since the performance is overestimated relative to measurements. This is concluded on the basis of stagnation pressures and temperatures that are predicted to be 50 kPa and 50

K lower than those measured. In addition, the efficiency is predicted to be 99 % whereas measurements indicate 91 %. Finally, the reaction stage indicates an overestimation of the turbine performance since the reaction stage is predicted to be in the range of 0.3 at all speeds. Based on the turbine design it is expected that the degree of reaction should be closer to zero. Such change would be the result of lowering turbine performance. The compressor work is at maximum 28 % lower than the turbine work. The difference between specifications and measurements regarding maximum speed agrees with the comparison of compressor and turbine work, which indicates that the engine cannot exceed 77,000 RPM.

The mass flow of air entering the engine at different speeds is defined from experiments, and the accuracy of this relation is essential for the modeling results. The thrust measured during test runs equals the modeling results, and since thrust only depends on outlet flow velocity and mass flow it seems that the mass flow is modeled correctly throughout the engine modeling. However, it is considered a subject of future work to emphasise the validation of the mass flow due to the significance of this variable.

Plotting the change of specific stagnation enthalpy throughout the modeling reveals that incidence losses are modeled incorrectly. The modeling approach to incidence losses is obtained from reliable literature. However, this approach enables the possibility of an increasing stagnation enthalpy at locations where this is not possible. As a result, it is a subject for future work to modify the modeling of incidence losses in order to get correct energy balances.

Finally, it is validated that the modeling predicts the performance of the SR-30 engine with an accuracy that is sufficient to analyse the tendencies when changing for instance the fuel. The modeling does however not predict the performance of the SR-30 engine with a high accuracy as aimed for in the problem statement. When using two dimensional velocity triangles to model small scale engines, the impact of neglecting the third velocity component rises. Thus it is expected that the modeling approach presented in this report will reveal accurate results with respect to turbojet engines at a larger scale.

## 5.1 Future Work

Three main focuses are considered as subjects for future work in order to improve the modeling of the SR-30 turbojet engine. Firstly, the issue about increasing stagnation enthalpies due to the modeling of incidence losses forms a possible improvement. It is expected that by defining the incidence loss from the change of absolute velocity rather than only the change of tangential velocity, the stagnation enthalpy will remain constant. It means that the stagnation enthalpy will neither decrease at a point where the absolute velocity is increased, nor increase where the velocity decrease due to incidence. Thereby, also the problems associated with the calculation of efficiencies are eliminated. These problems were explained in subsection 4.6.3.

The test engine does not provide information about the mass flow of air that enters the system and to overcome this, an experiment, associated with some inaccuracy, has been performed in the project. The modeling results depend highly on this particular mass flow, and thus the validity of the modeling may be improved by measuring this mass flow in a more accurate way. Future work may be measurements of static pressure at outlet of the exhaust nozzle. Along with the measurements of stagnation pressure at the same location, such experiments provide exact information about the flow velocity at outlet of the exhaust nozzle. This information can be used to calculate the mass flow of flue gas out of the system, since the thrust delivered by the engine is also measured in the test engine. Now, with the mass flow of flue gas and the fuel flow it is possible to obtain exact values for the inlet mass flow of air. This will, as mentioned, improve the validation of the modeling.

Evaluation of the combustion modeling revealed an outlet temperature higher than the one measured during test runs. This may be influenced by the mass flow of air into the combustion chamber, but it could quite likely also be the choice of fuel in CEA NASA that causes this deviation. An experiment with the purpose of defining the heating value of the test fuel could be subject of future work, since this would validate or falsify the choice of jet fuel in CEA NASA.

The problem statement of this project is formulated from the wish of doing fuel and engine testing as a first step rather than flight testing in the aim of combining biofuel and aviation. When the SR-30 model is considered valid, the next step is to vary for instance the fuel input, in particular biofuels, in order to model the affects such variations have on the engine performance. Concludingly, the approach may be applied in connection with engine testing, which as mentioned is the first step of combining biofuels and aviation.



# Bibliography

---

- ATAG (2009), *Beginner's guide to aviation biofuels*, Technical report, Air Transport Action Group. Attached on CD.
- Bridgat (2012), *Search for: o128671*, [www.bridgat.com](http://www.bridgat.com). Viewed: 30.04.2012.
- CAAFI (2007), *Roadmaps*, Technical report, CAAFI, Commercial Aviation Alternative Fuels Initiative. Attached on CD.
- Cengel, Yunus A. and Michael A. Boles (2007), *Thermodynamics - An Engineering Approach*, McGraw-Hill. ISBN: 978-007-125771-8.
- Condra, Thomas (2012), *Personal Contact*, Aalborg University.
- Cumsty, N.A (2004), *Compressor Aerodynamics*, Krieger Publishing Company. ISBN: 1-57524-247-8.
- Dixon, S.L. and C.A. Hall (2010), *Fluid Mechanics and Thermodynamics of Turbomachinery*, Elsevier. ISBN: 978-1-85617-793-1.
- Ferguson, T. B. (1963), *Centrifugal Compressor Stage*, Butterworths.
- Glassman, Arthur J. (1994), *Turbine design and application (nasa sp-290)*, Technical report, NASA.
- Grundfos (2008), *The Centrifugal Pump*, Grundfos Management A/S.
- Hughes, William F. and John A. Brighton (1991), *Theory and Problems of Fluid Dynamics*, McGraw-Hill. ISBN: 0-07-031117-X.
- Jiang, Wei, Jamil Khan and Roger A. Dougal (2005), *Dynamic centrifugal compressor model for system simulation*, Technical report, Elsevier. Attached on CD.
- Kreyszig, Erwin (2006), *Advanced Engineering Mathematics 9.th Ed.*, John Wiley and Sons. ISBN: 978-0-471-72897-9.
- Munson, Bruce, Donald Young and Theodore Okiishi (2006), *Fundamentals of Fluid Mechanics 5th ed.*, John Wiley and Sons. ISBN: 0-471-67582-2.
- Paul, M. Vincent De (1998), *Turbines a fluide compressible*, Technical report, Centrale Paris. Attached on CD.
- Ph. Novelli (2011), *Sustainable way for alternative fuels and energy in aviation*, Technical report, SWAFEA, Sustainable Way for Alternative Fuels and Energy for Aviation. Attached on CD.
- Turbine Technologies (2012), *Gas Turbine Lab*, [www.turbinetechnologies.com](http://www.turbinetechnologies.com). Viewed: 22.03.2012.
- Turns, Stephen (2000), *An Introduction to Combustion 2.ed.*, McGraw-Hill. ISBN: 0-07-230096-5.
- Walker, Roger (2007), *Density of Liquids*, [simetric.co.uk](http://simetric.co.uk). Viewed: 10.05.2012, Attached on CD.
- W.Bathie, Willian (1984), *Fundamentals of Gas Turbines*, John Wiley and Sons. ISBN: 0-471-86285-1.
- Witkowski, T., S. White, C. Ortiz Dueñas, P. Strykowski and T. Simon (2003), *Characterizing the performance of the sr-30 turbojet-engine*, Technical report, University of Minnesota. Attached on CD.



# Appendix

---



# The Modeling A

---

This appendix presents the mainfile and the submodels used in the modeling of the SR-30 engine. In the mainfile all the submodels are implemented along with a Matlab script that plots chosen modeled and measured parameters as a function of RPM in order to do a comparison. In the mainfile a loop solves the modeling at different RPM between 45,000 and 85,000 and thus it is possible to plot the results as a function of RPM.

The input to the mainfile is the inlet pressure and temperature. Other than these the only inputs that are implemented in the modeling is the mass flow of air and fuel based on test results on the engine and the dimensions of the engine provided by *Turbine Technologies*.

The following pages consists of the matlab scripts used to model ther turbojet engine. A digital version of the Matlab scripts are added in appendix (CD) along with the test results.

```

% The Combustion function is applied in the 'main file' of our 6th semester
% project.
% it models the combustion chamber of the jet engine
function [P7,T7,m7] = Combustion(P6,m6,m_fuel,m_RPM);

% Equilibrium calculations for the fuel JP-4 and Air
rho_fuel = 817; %kg/m3 at 15C
M_fuel = 13.94; %kg/kmol
M_air = 28.8; %kg/kmol

%%%%%%%%%%%%%%%%%%%%%%%%%%%%%%%%%%%%%%%%%%%%%%%%%%%%%%%%%%%%%%%%%%%%%%%%%%%%%%
% Data from the poster used to determine AF
m_out_poster = 0.5; % data from poster provided by Lasse
Thrust_poster=40*4.448; %N from Poster
% 1.221b/lbhour
% 0.4536kg/lb
m_fuel_poster = 1.22*0.4536/4.448*Thrust_poster/3600*1000;%kg/s
m_air_poster = m_out_poster*m_fuel_poster; % kg/s
AF_poster = m_air_poster/m_fuel_poster; % air fuel ratio from the poster
%%%%%%%%%%%%%%%%%%%%%%%%%%%%%%%%%%%%%%%%%%%%%%%%%%%%%%%%%%%%%%%%%%%%%%%%%%%%%%
% The combustion mass flow outlet
m7 = (m6+m_fuel);

%%%%%%%%%%%%%%%%%%%%%%%%%%%%%%%%%%%%%%%%%%%%%%%%%%%%%%%%%%%%%%%%%%%%%%%%%%%%%%
% Determining a relation between RPM and adiabatic flame temperature
RPM_adia = [45000;5000;85000];
T_adia = [767 799 825 848 869.5 888.9 908 926 946];
coef = polyfit(RPM_adia,T_adia,2);
p_adia1 = coef(1); p_adia2 = coef(1,2); p_adia3 = coef(1,3);
T_adia_app = p_adia1.*RPM_adia.^2+p_adia2.*RPM_adia+p_adia3;

% Plot of the adiabatique temperature as function of the RPM
% figure(10)
% plot(RPM_adia,T_adia, 'r')
% hold on
% plot(RPM_adia,T_adia_app)
% title('Adiabatic Flame Temperature as a function of RPM', 'FontSize',13)
% xlabel('RPM [min^-1]','FontSize',11),ylabel('Temperature [K]','FontSize',11)
% legend('Data Points from CEA NASA','Quadratic regression','Location','NW')
% grid on

T_adia_app = (p_adia1.*RPM.^2+p_adia2.*RPM+p_adia3);
T7 = T_adia_app; %Result from CEA Nasa where p6, phi, n_fuel and ns are implemented
P7 = P6; % the pressure is assumed constant in the combustion chamber

```

```

% The Compressor function is applied in the 'main file' of our 6th semester
% project.
% it models the impeller of the jet engine
function [Cp3,Cp4,h04,h04,P3,T3,V3_abs,rho3,T03,P03,P4,T4,m4,V4,rho4,T04,P04,U4,
V_radial4,V4_tan,Workreal,Mach3,Mach4,A4,beta4,incidenceangle3,slipangle4,dh_il3,
dh_df3,dP_fl3,dh_fl3] = CompressorRotor(fluid,Cp2,P2,T2,m2,V2,rho2,T02,P02,rpm,h02);

% Mass balance
m4=m2;
m3=m2;

% 3. Inlet of the Impeller%%
%%% The measures :
% Height and diameter are measured in Solidworks
OuterD3 = 63.5e-3; %m Diameter of outer inlet
InnerD3 = 21.056e-3; %m Radius of inner inlet
A3 =(OuterD3/2)^2*pi - (InnerD3/2)^2*pi; %m2 Inlet Area when neglecting the blade area
bladeheight3 = (OuterD3-InnerD3)/2; %m height of the blade

%blade speed
Tip_speed3 = rpm*2*pi/60 * InnerD3/2; %m/s
U3 = [-Tip_speed3 0]; %m/s

%%% Velocities at the Inlet.
% The radial dimension is eliminated in order to get 2-dimensional velocity triangles
V3_axial = V2; %m/s
beta3 = (443.89+27.86)/2/180*pi; %Angle from Solidworks
W3 = [V3_axial*tan(beta3) V3_axial]; %m/s
W3_abs = vec1(W3); %m/s
W2 = [-U3(1) V3_axial]; %m/s
beta2 = atan(W2(1)/W2(2)); %rad
V3_abs_vec = W3+U3; %m/s
V3_abs=vec1(V3_abs_vec); %m/s

%%% Incidence Loss
incidenceangle3 = (beta2-beta3)*180/pi; %degree
dh_il3 = 1/2*(W2(1)-W3(1))^2;

%%% Iteration calculating the parameters at the inlet
P3 = P2; T3 = T2; rho3 = rho2; %guess values
tolerance = 1e-5;
error3=1;
i=1;
while tolerance<error3(i);
Cp3(i) = Cp2; %J/kg*K
kappa(i+1) = refpropm('K','T',(T2+T3(i))/2,'P',(P2+P3(i))/2,fluid); %Cv/Cp [-]
Mach3(i+1) = V3_abs/refpropm('A','T',T3(i),'P',P3(i),fluid);
T3(i+1)=T2-dh_il3/Cp3(i); %K
T03(i+1)=T3(i+1)+V3_abs^2/(2*Cp3(i)); %K

```

```

P03(i+1)=P02*(T03(i+1)/T02)^(kappa(i+1)/(kappa(i+1)-1)); %kPa
P3(i+1)=P03(i+1)/(1+(kappa(i+1)-1)/2*Mach3(i+1)^2)^(kappa(i+1)/(kappa(i+1)-1)); %kPa
rho3(i+1)=refprop('D','T',T3(i+1),'P',P3(i+1),fluid); %kg/m3

%error matrix
error_matrix3(i,:)=[(P3(i)-P3(i+1))/P3(i) (T3(i)-T3(i+1))/T3(i) 0 0 (W3_abs-V3_abs)
/V3_abs (rho3(i)-rho3(i+1))/rho3(i) (Mach3(i)-Mach3(i+1))/Mach3(i)];
error3(i+1,1) = max(abs(error_matrix3(i,:)));
i=i+1;
end

%Plot of the error matrix
% errormatrix_size=size(error_matrix3);
% iterations=(1:l:errormatrix_size(1));
% figure(4)
% plot(iterations,error_matrix3), axis([1 errormatrix_size(1) -0.2 0.2]); legend
('P','T','P0','T0','m','V','rho','Mach'); title('Error as a function of
iterations','FontSize',13); xlabel('Iterations','FontSize',11); ylabel
('Errors','FontSize',11);

T3=T3(i) ; Mach3=Mach3(i) ; rho3=rho3(i) ; P3=P3(i) ; P03=P03(i) ; T03=T03(i) ; Cp3=Cp3(i-1) ;

% Enthalpies at the inlet
h3 = refprop('H','T',T3,'P',P3,fluid); %J/kg*K An average value over the stator
h03 = h3 + V3_abs^2/2;

% PLOTS of Velocity triangle :
% V3_vec=V3_abs_vec; W3_vec = W3;
% V3_vec_plot = [-V3_vec(1) 0;0 V3_vec(2)]; W3_vec_plot = [-W3_vec(1) 0;0 W3_vec
(2)]; U3_plot = [-V3_vec(1) 0;-V3_vec(1)+U3(1) U3(2)]; Blade3_plot = [0 V3_vec(2);
0+30*sin(beta3) V3_vec(2)+30*cos(beta3)];
% V2_vec=[0 V2]; W2_vec = V2_vec-U3;
% V2_vec_plot = [-V2_vec(1) 0;0 V2_vec(2)]; W2_vec_plot = [-W2_vec(1) 0;0 W2_vec
(2)]; U2_plot = [-V2_vec(1) 0;-V2_vec(1)+U3(1) U3(2)]; Blade2_plot = [-V2_vec(1) 0;-
V2_vec(1)-30*sin(0) 0-30*cos(0)];

% figure(5)
% plot(Blade2_plot(:,1),Blade2_plot(:,2),'black',Blade3_plot(:,1),Blade3_plot(:,
2),'black')
% hold on
% plot(W2_vec_plot(:,1),W2_vec_plot(:,2),'b',W2_vec_plot(:,1),W2_vec_plot(:,2),'r',
U2_plot(:,1),U2_plot(:,2),'c')
% plot(V3_vec_plot(:,1),V3_vec_plot(:,2),'b',W3_vec_plot(:,1),W3_vec_plot(:,2),'r',
r',U3_plot(:,1),U3_plot(:,2),'c')
% title('Velocity Triangle at the Inlet of the Impeller','FontSize',13)
% legend('Inlet Nozzle Direction \alpha_2 = 0^\circ','Impeller blade \beta_3 =
36^\circ','V_2','W_2','U_3','V_3','W_3','U_3','Location','SO'); axis('equal');
% xlabel('Tangential velocity [m/s]','FontSize',11),ylabel('Axial velocity
[m/s]','FontSize',11)

% 4. OULET OF THE IMPELLER %
% % % % measurements
bladeheight4 = 5.082e-3; %Axial height of outlet area

```

```

r4 = (104.773e-3)/2; % radius
Tip_speed4 = (rpm*2*pi/60)*r4; %m/s
U4 = [-Tip_speed4 0]; %blade speed

%Blade area defined by a medium width which is subtracted from the perimeter:
bladewidth4 = ((1.560+1.339)*1e-3)/2; %m
A4 = (pi*r4-12*bladewidth4)*bladeheight4; %m2

% % % % friction loss
% Mean dimensions
A_mean = (A3+A4)/2; %Mean area of in- and outlet
width3 = ((OuterD3+InnerD3)/2)*pi/12; % Width at impeller inlet
width4 = r4*2*pi/12; % Width at impeller outlet
w_mean = (width3+width4)/2; %Mean width of impeller channels
h_mean = (bladeheight3+bladeheight4)/2; %mean height
Dh = 2*A_mean/(w_mean+h_mean); %hydraulic diameter
l_mean = 65e-3; %mean channel
% calculation of the friction coefficient
syms f
visk3 = refprop('V','T',T3,'P',P3,fluid)/rho3; %Kinematic viscosity
Re = vecl(U4)*bladeheight4/visk3; %Article_noref
epsilon = 0.000045; %m ASSUMPTION, it is the roughness of commercial steel taken from
an exercise in strømningslære
% Friction factor f from Colebrook and White
f=solve(1/(f*(1/2))+2*log((epsilon/Dh)*0.2703+2.51/(Re*sqrt(f))),f); % Colebrook and
White, Ferguson page 51
f=eval(f);

% % % % Velocities at the outlet of the rotor part :
% The axial dimension is eliminated in order to get 2-dimensional velocity triangles
T4=380; T04s = T03; P4=167; rho4=refprop('D','T',T4,'P',P4,fluid); % guess values
error4=1; i=1;
while tolerance<error4(i);
V_radial4(i) = m4/(A4*rho4(i)); %m/s
beta4=(4.62+4.10)/2/180*pi; %rad
slipfactor4 = 1-sqrt(cos(beta4))/(12)^0.7;
W4(i) = V_radial4(i)/cos(beta4); %m/s
W4_tan(i) = W4(i)*sin(beta4); %m/s
V4_tan(i) = (W4_tan(i) + U4(i))*slipfactor4; %m/s % The slip factor is multiplied to
the tangential velocity as it is considered to be idealized (CUMSTY p.245)
V4_abs_vec(i+1,:) = [V4_tan(i) V_radial4(i)];
V4_abs(i+1)=vecl(V4_abs_vec(i+1,:)); %m/s

% % % Friction Loss
W_mean = (vecl(W3)+W4(i))/2; % Mean relative velocity
dh_fl3(i) = (f*1_mean*W_mean^2/(2*Dh))*12; %J/kg
dP_fl3(i) = (f*1_mean*W_mean^2/(2*Dh))*12*(rho3+rho4(i))/2*1e-3; %kPa

% % % Disk Friction "The Centrifugal Pump" Grundfos
visk4(i) = refprop('V','T',T4(i),'P',P4(i),fluid)/rho4(i); %Pa.s
m_disc = 1/6; % coefficient for a smooth surface
e_disc = 0.3e-3; % axial distance to wall at the periphery of the impeller
r_mean = ((OuterD3+InnerD3)/4+r4)/2; %mean radius
k = 7.3*10^-4*((visk3+visk4(i))/(2*10^6/(abs(U4(1))*r_mean)))^(m_disc); %empirical value

```

```

dh_df3(i) = k*(rho3+rho4(i))/2*abs(U4(i))^3*r_mean*2*(r_mean*2+5*e_disc)/m3; %J/kg

%% Work Calculations - Reference: Page 240, Book: Fundamentals of Gas Turbines
Workideal(i) = (U4(i)*V4_tan(i)-U3(i)*V3_abs_vec(1)); %m2/s2 = J/kg From Dixon p. 222
eq. 7.3
W_loss = dh_df3(i) + dh_fl3(i); %J/kg
Workreal(i)=Workideal(i)+W_loss; %J/kg
eta4(i)=1-W_loss/Workreal(i);

Cp4(i) = refpropm('C','T',(T4(i)+T3)/2,'P',(P4(i)+P3)/2,fluid); %J/kg*K
kappa(i) = refpropm('K','T',(T4(i)+T3)/2,'P',(P4(i)+P3)/2,fluid); %Cv/Cp
T04s(i+1) = T03 + Workideal(i)/Cp4(i); %K isentropic temperature
T04(i+1) = T03*(T04s(i+1)/T03-1)/eta4(i) + 1;
T4(i+1) = T04(i+1) - V4_abs(i+1)^2/(2*Cp4(i));
Mach4(i+1) = V4_abs(i+1)/refpropm('A','T',T4(i+1),'P',P4(i),fluid);
P4(i+1) = P03*(T04s(i+1)/T03)^(kappa(i)/(kappa(i)-1))-dP_fl3(i); %kpa
P4(i+1) = P04(i+1)/((1+(kappa(i)-1)/2*Mach4(i+1)^2)^(kappa(i)/(kappa(i)-1))); %kpa
rho4(i+1) = refpropm('D','T',T4(i+1),'P',P4(i),fluid); %kg/m3

error_matrix4(i,:) = abs([(P4(i)-P4(i+1))/P4(i) (T4(i)-T4(i+1))/T4(i) (P04(i)-P04(i+1))/P04(i) (T04(i)-T04(i+1))/T04(i) 0 (V4_abs(i)-V4_abs(i+1))/V4_abs(i) (rho4(i)-rho4(i+1))/rho4(i) (Mach4(i)-Mach4(i+1))/Mach4(i)]);
error4(i+1,i) = max(error_matrix4(i,:));
i=i+1;
end
W4 = V4_abs_vec(i,:)-U4;
slipang1e4 = (beta4-atan(W4(1)/W4(2)))*180/pi;

%Plot of the errors matrix
% errormatrix_size=size(error_matrix4);
% iterations=(1:i:errormatrix_size(1));
% figure(6)
% plot(iterations,error_matrix4), axis([1 errormatrix_size(1) -0.01 0.02]); legend
('P','T','P0','T0','m','V','rho','Mach'); title('Error as a function of
iterations','fontsize',13); xlabel('Iterations','fontsize',11); ylabel
('Errors','fontsize',11);

% Definition of the results that are given as outputs
P4=P4(i); Mach4=Mach4(i); T4=T4(i); V4=abs(V4_abs(i)); rho4=rho4(i); Workreal=Workreal
(i-1); P04=P04(i); T04=T04(i); V_radial4 = abs(V_radial4(i-1)); V4_tan = V4_tan(i-1);
dh_df3=dh_df3(i-1); dP_fl3=dP_fl3(i-1); dh_fl3=dh_fl3(i-1); Workideal=Workideal(i-1);
T04s=T04s(i); Cp4=Cp4(i-1);

%% Enthalpies
h4 = refpropm('H','T',T4,'P',P4,fluid);
h04 = h4 + V4^2/2;

```

```

% The Diffuser function is applied in the 'main file' of our 6th semester
% project.
% % it models the diffuser of the jet engine
function [Cp6,Cp5,h05,h06,P6,T6,m5,m6,rho6,T05,P05,P5,T5,V5_abs,rho5,Mach5,Mach6,T06,
P06,V6_abs,angle5,sangle6,dh_i15,dh_i16,dP_fl6] = CompressorStator(fluid,Cp4,h02,P4,
T4,m4,rho4,T04,P04,V_radial4,V4_tan,A4,T02,P02,T2,P2);
% Mass balance
m6=m4;
m5=m4;

%% 5. INLET OF THE DIFFUSER %%
%%% measurements
D5 = 105.41e-3;
bladeheight5 = 4.891e-3;
A5_stator = pi*D5*bladeheight5; % Neglecting bladearea
% The ratio of impeller outlet area and diffuser inlet area in order to check
smoothness of expansion
Ratio_compressorgab = A4/A5_stator;

%%% Iterations
%The axial dimension is eliminated in order to get 2-dimensional velocity triangles
P5 = P4; T5 = T4; rho5 = rho4; % guess values
tolerance = 1e-5; error5=1; i=1;

while tolerance<error5(i);
V5_radial = V_radial4; %m/s
alfa5 = (90-23.48)/180*pi; % rad Angle from Solidworks
V5_abs(i+1) = V5_radial/cos(alfa5); %m/s
V5_tan(i+1) = -V_radial4*tan(alfa5);%m/s

%% Incidence loss
dh_i15(i) = 1/2*(V4_tan-V5_tan(i+1))^2; %J/kg

Cp5(i) = Cp4; %J/kg*K
T5(i+1) = T4+dh_i15(i)/Cp5(i); %K
T05(i+1) = T5(i+1)+V5_abs(i+1)^2/(2*Cp5(i)); %K
kappa(i+1) = refpropm('K','T',(T4+T5(i+1))/2,'P',(P4+P5(i))/2,fluid); %Cv/Cp [-]
P05(i+1)=P04*(T05(i+1)/T04)^(kappa(i+1)/(kappa(i+1)-1)); %kPa
Mach5(i+1) = V5_abs(i+1)/refpropm('A','T',T5(i+1),'P',P5(i),fluid);
P5(i+1)=P05(i+1)/((1+(kappa(i+1)-1)/2*Mach5(i+1)^2)^(kappa(i+1)/(kappa(i+1)-1))); %kPa
rho5(i+1)=refpropm('D','T',T5(i+1),'P',P5(i+1),fluid); %kg/m3

error_matrix5(i,:)=([(P5(i)-P5(i+1))/P5(i) (T5(i)-T5(i+1))/T5(i) (P05(i)-P05(i+1))/P05
(i) (T05(i)-T05(i+1))/T05(i) 0 (V5_abs(i)-V5_abs(i+1))/V5_abs(i) (rho5(i)-rho5(i+1))
/rho5(i) (Mach5(i)-Mach5(i+1))/Mach5(i) 1);
error5(i+1,1) = max(abs(error_matrix5(i,:)));
i=i+1;
end

alfa4 = -atan(V4_tan/V_radial4);
iangle5 = (alfa4-alfa5)*180/pi; %incidence angle

%Plot of the errors matrix :
% errormatrix_size=size(error_matrix5);

```

```

% iterations=(1:1:errormatrix_size(1));
%figure(7)
% plot(iterations,error_matrix5), axis([1 errormatrix_size(1) -0.2 0.2]); legend
('P','T','P0','T0','m','V','rho','Mach'); title('Error as a function of
iterations', 'FontSize',13); xlabel('Iterations', 'FontSize',11); ylabel
('Errors','FontSize',11);

V5_abs=V5_abs(i); T5=T5(i); dh_i15=dh_i15(i-1); Mach5=Mach5(i); rho5=rho5(i); P5=P5(i);
P05=P05(i); T05=T05(i); Cp5=Cp5(i-1);

% Enthalpies of the inlet
h5 = refprop('H','T5','P5','fluid'); %J/kg*K An average value over the stator
h05 = h5 + V5_abs^2/2; %J/kg.K

% PLOTS of the Velocity triangles:
% V5_vec=[V5_tan(i) V5_radial]; W5_vec = V5_vec-U4;
% V5_vec_plot = [-V5_vec(1) 0:0 V5_vec(2)]; W5_vec_plot = [-W5_vec(1) 0:0 W5_vec
(2)]; U5_plot = [-V5_vec(1) 0:-V5_vec(1)+U4(1) U4(2)]; Blades_plot = [0 V5_vec(2):0-
100*sin(alpha5) V5_vec(2)+100*cos(alpha5)];
% V4_vec=[V4_tan V_radial4]; W4_vec = V4_vec-U4;
% V4_vec_plot = [-V4_vec(1) 0:0 V4_vec(2)]; W4_vec_plot = [-W4_vec(1) 0:0 W4_vec
(2)]; U4_plot = [-V4_vec(1) 0:-V4_vec(1)+U4(1) U4(2)]; Blade4_plot = [-W4_vec(1) 0:-
W4_vec(1)-100*sin(beta4) 0-100*cos(beta4)];

% figure(8)
% plot(Blade4_plot(:,1),Blade4_plot(:,2),'black',Blade5_plot(:,1),Blade5_plot(:,
2),'black')
% hold on
% plot(W4_vec_plot(:,1),V4_vec_plot(:,2),'b',W4_vec_plot(:,1),W4_vec_plot(:,2),'r',
U4_plot(:,1),U4_plot(:,2),'c')
% plot(V5_vec_plot(:,1),V5_vec_plot(:,2),'b',W5_vec_plot(:,1),W5_vec_plot(:,2),':
r',U5_plot(:,1),U5_plot(:,2),'c')
% title('Velocity Triangle at the Inlet of the Diffuser','FontSize',13)
% legend('Impeller blade \beta_4 = 4^\circ','Diffuser blade \alpha_5 =
67^\circ','W_4','U_4','W_5','U_5','location','SO'); axis('equal');
% xlabel('Radial velocity [m/s]','FontSize',11),ylabel('Tangential velocity
[m/s]','FontSize',11)

%% OUTLET OF THE DIFFUSER %%
%%%%measurements
bladeheight6 = 7.267e-3; %m Axial height of outlet area
bladewidth6 = 9.79e-3; %m
FootArea = 1/2*1.317e-3*1.751e-3; %m
D6 = 150.975e-3; %m outer diameter
bladearea = 18*(bladeheight6*bladewidth6+FootArea); %m2
A6 = pi*D6*bladeheight6-bladearea; %m2 outlet area

%%%%Friction loss
%Mean dimensions
A_mean = (A5_stator+A6)/2; %Mean area of in- and outlet
w_mean = ((9.962+5.303)/2)^1e-3; %Mean width of impeller channels
h_mean = (bladeheight5+bladeheight6)/2;
Dh = 2*A_mean/(w_mean+h_mean); %hydraulic diameter

```

```

l_mean = 119*1e-3; % m Mean channel length
%Calculation of the friction coefficient
syms f
visk5 = refprop('V','T5','P5','fluid)/rho5; %Kinematic viscosity
Re = V5_abs*Dh/visk5;
epsilon = 0.000045; %m ASSUMPTION, it is the roughness of commercial steel taken from
an exercise in strammingslere
% Friction factor f from Colebrook and White
f=solve(1/(f*(1/2))+2*log((epsilon/Dh)*0.2703+2.51/(Re*sqrt(f))),f); % Colebrook and
White, Ferguson page 51
f=eval(f);

T06=T05;
%%%% Iterations :
% We eliminate the axial dimension in order to get 2dimensional velocity triangles
% Guess values:
T6=T5; P6=P5; P06=P05;
rho6=refprop('D','T6','P6','fluid'); %kg/m3
error6=1; i=1;
while tolerance<error6;
V6_radial(i) = m6/(A6*rho6(i)); %m/s
alpha6 = (90-47.05)/180*pi; %rad
slipfactor6 = 1-sqrt(cos(alpha6))/(i8)^0.7;
V6_tan(i+1) = -V6_radial(i)*tan(alpha6)*slipfactor6; %m/s
V6_abs_vec(i+1,:) = [V6_tan(i+1);V6_radial(i)]; %m/s
V6_abs(i+1) = vecl(V6_abs_vec(i+1,:)); % m/s Absolute value

%%Friction Loss
V_mean(i+1) = (V6_abs(i+1)+V5_abs)/2; % Mean absolute velocity
dh_fl16(i) = f*V_mean(i+1)^2*l_mean/(2*Dh)*18; %J/kg friction loss used as a heat loss
dP_fl16(i) = f*V_mean(i+1)^2*l_mean/(2*Dh)*(rho5+rho6(i))/2*18*1e-3; %kPa friction loss
used as a pressure drop

Cp6(i) = refprop('C','T6','P6','fluid'); %J/kg*K An average
value over the stator
T6(i+1)=(T06-(V6_abs(i+1)^2)/(2*Cp6(i))+dh_fl16(i)/Cp6(i)); %K
Mach6(i+1) = V6_abs(i+1)/refprop('A','T6','P6','fluid');
kappa(i+1) = refprop('K','T6','P6','fluid'); %Cv/Cp [-]
P6(i+1)=P06(i)/((1+(kappa(i+1)-1)/2*Mach6(i+1)^2)^(kappa(i+1)/(kappa(i+1)-1))); %kPa
rho6(i+1)=refprop('D','T6','P6','fluid'); %kg/m3
P06(i+1)=P05-dp_fl16(i); %kPa
error_matrix6(i,:)=abs([(P6(i)-P5(i+1))/P6(i) (T6(i)-T6(i+1))/T6(i) (P06(i)-P06(i+1))
/P06(i) 0 (V6_abs(i)-V6_abs(i+1))/V6_abs(i) (rho6(i)-rho6(i+1))/rho6(i) (Mach6(i)-
Mach6(i+1))/Mach6(i)];
error6(i+1,1) = max(error_matrix6(i,:));
i=i+1;
end
sangle6 = (-atan(V6_abs_vec(i,1)/V6_abs_vec(i,2))-alpha6)*180/pi; % deviation angle
%Plot of the errors matrix
% errormatrix_size=size(error_matrix6);

```

```

% iterations=(1:1:errormatrix_size(1));
% figure(9)
% plot(iterations,error_matrix6, axis([1 errormatrix_size(1) 0 0.2]); legend
('P','T','P0','T0','m','V','rho','Mach'); title('Error as a function of
iterations', 'fontSize',13); xlabel('Iterations', 'fontSize',11); ylabel
('Errors', 'fontSize',11);

% Definition of the results that are given as outputs
P06=P06(i); P6=P6(i); T6=T6(i); V6_abs=abs(V6_abs(i)); rho6=rho6(i); Mach6=Mach6(i);
Cp6=Cp6(i-1);
dh_fl6=dh_fl6(i-1);dP_fl6=dP_fl6(i-1);

% Enthalpies
h06 = refprop('H','T',T06,'P',P06,fluid);
T06s = (P06/(P02))^(1/(kappa(i-1)-1)/kappa(i-1))*(T02);
h06s_C = refprop('H','T',T06s,'P',P06,fluid);

% Overall compressor efficiency
eta_c = (h06s_C-h02)/(h06-h02)

% Values used when calculating the efficiency from measurements:
kappa_mean_compressor = refprop('K','T',(T2+T6)/2,'P',(P2+P6)/2,fluid);
Cp_mean_compressor = refprop('C','T',(T2+T6)/2,'P',(P2+P6)/2,fluid);

```

```

% The Inlet function is applied in the 'main file' of our 6th semester project.
% it models the inlet of the jet engine
function [Cp1,Cp2,h01,h02,P2,T2,m2,V2_abs,V1_abs,rho1,rho2,T02,P02,Mach2,Mach1,P01,T01,
T2_star] = Inlet(fluid,P1,T1,m1);

%% GIVEN PARAMETERS %%
% Mass balance
m2=m1;

% Dimensions are measured from Solid Works
D2 = 64.770e-3; %m outlet diameter of the nozzle
D1 = 149.606e-3; D1_linear = 125.701e-3; dist_D = 77.028e-3; %m inlet diameter of the
nozzle
Dx = (D2-D1_linear)/dist_D; %m %Coefficient for the diameter gradient of the nozzle
D_hub=21.056e-3; % diameter of the hub inside the nozzle

% Pressure is measured at a distance dist_P2 from D2.
dist_P2 = 19.304e-3; %m

% Diameter of the nozzle at the sensor place
D2_star = D1_linear+(dist_D-dist_P2)*Dx; %m

% Constants
kappa1 = refprop('K','T',T1,'P',P1,fluid); %cv/cp
Cp1 = refprop('C','T',T1,'P',P1,fluid); %J/kg*K
rho1=refprop('D','T',T1,'P',P1,fluid); %kg/m3
A1 = D1^2/4*pi; %m2 inlet area
A2 = (D2^2/4-D_hub^2/4)*pi; %m2 outlet area
A2_star=D2_star^2/4*pi; %m2 area where the temperature sensors is placed

%% 1. INLET %%
V1_abs = m1/(rho1*A1); %m/s
Mach1=V1_abs/refprop('A','T',T1,'P',P1,fluid);
T01 = T1+V1_abs^2/(2*Cp1); %K Stagnation temperature
P01=P1*(1+(kappa1-1)/2*Mach1^2)^(kappa1/(kappa1-1)); %kPa Stagnation Pressure
% Enthalpies at the Inlet
h1 = refprop('H','T',T1,'P',P1,fluid); %J/kg*K An average value over the stator
h01 = h1 + V1_abs^2/2; % J/kg*K stagnation enthalpie

%% OUTLET %%
T02 = T01; P02 = P01; % No work done to the flow
% Iteration calculating the temperature at the temperature sensor place
rho2_star=rho1; P2_star=P1; T2_star=T1; Mach2_star=Mach1; %Guess values
tolerance = 1e-3; error2_star=1; i=1;

while error2_star > tolerance
    V2_abs_star(i+1) = m1/(rho2_star(i)*A2_star); %m/s
    Mach2_star(i+1)= V2_abs_star(i+1)/refprop('A','T',T2_star(i),'P',P2_star(i),
fluid);
    rho2_star(i+1)= refprop('D','T',T2_star(i),'P',P2_star(i),fluid); %kg/m3
    kappa2_star(i+1) = refprop('K','T',(T2_star(i)+T1)/2,'P',(P2_star(i)+P1)/2,fluid);
    %cv/cp
    P2_star(i+1)=P02/((1+(kappa2_star(i+1)-1)/2)*Mach2_star(i+1)^2)^(kappa2_star(i+1)
/(kappa2_star(i+1)-1)); %kpa
    Cp2_star(i+1) = refprop('C','T',(T2_star(i)+T1)/2,'P',(P2_star(i+1)+P1)/2,fluid);

```



```

lambda_app = n_air/ns;
phi_app = 1/lambda_app;
AF_app = m_air_app/m_fuel;

% Plot: Silencer inlet mass flow and fuel consumption
figure(1)
subplot(2,1,1)
hold on
plot(RPM_plot,m_air_plot)
title('Inlet air mass flow as a function of RPM','FontSize',13); xlabel('RPM','FontSize',11)
ylabel('Mass flow [kg/s]','FontSize',11)
legend('Data points','Linear approximation','Location','NW')
grid on
subplot(2,1,2)
plot(RPM_test,m_fuel_test,'.')
hold on
plot(RPM_plot,m_fuel_plot)
title('Fuel consumption as a function of RPM','FontSize',13); xlabel('RPM','FontSize',11)
ylabel('Mass flow [kg/s]','FontSize',11)
legend('Data points','Linear approximation','Location','NW')
grid on

% Plot: Lambda and AF determined from inlet air mass flow
figure(2)
subplot(2,1,1)
plot(RPM,AF_app)
title('AF ratio as a function of RPM','FontSize',13); xlabel('RPM','FontSize',11)
ylabel('AF [\cdot]','FontSize',11)
grid on
subplot(2,1,2)
plot(RPM_plot,lambda_app)
title('\lambda as a function of RPM','FontSize',13); xlabel('RPM','FontSize',11)
ylabel('\lambda [\cdot]','FontSize',11)
grid on
end

```

```

% The mainfile of our turbo-jet-engine project, 6th semester.
% The mainfile consists of subfunctions that evaluates inputs to each
% submodel and returns the output of these.
clc; clear all;
iteration=0;
for i=45000:2500:85000; % range for the engine speed [45000 85000]
iteration=iteration+1;

% Definition of parameters:
P = zeros(12,1); % Pressure kPa
T = zeros(12,1); % Temperature K
m = zeros(12,1); % Mass flow kg/s
h = zeros(12,1); % Specific enthalpy kJ/kg
V = zeros(12,1); % Volume flow m3/s
rho = zeros(12,1); % Velocity m/s
rho = zeros(12,1); % Density Kg/m3
T0 = zeros(12,1); % Stagnation Temperature (Total) K
P0 = zeros(12,1); % Stagnation Pressure (Total) K
Mach = zeros(12,1); % Mach number
fluid = 'air.PPF'; % Definition of fluid to be used in REFPROP

P_atm=101.325; % Atmospheric pressure kPa
P(1)=P_atm;
T(1)=273.15+13.7; % Kelvin
RPM =i; %engine speed

% The inlet mass flow
[AF,phi,m_fuel,m(1)] = Inlet_massflow(fluid,RPM,T(1),P(1));

% The inlet: Modelled as a compressible fluid
[Cp(1),Cp(2),h0(1),h0(2),P(2),T2_out,m(2),V(2),V(1),rho(1),rho(2),T0(2),P0(2),Mach(2),Mach(1),P0(1),T0(1),T(2)] = Inlet(fluid,P(1),T(1),m(1));

% The CompressorRotor:
[Cp(3),Cp(4),h0(3),h0(4),P(3),T(3),V(3),rho(3),T0(3),P0(3),P(4),T(4),m(3:4),V(4),rho(4),T0(4),P0(4),U4,V_radial(4),V_tan(4),Work_Compressor,Mach(3),Mach(4),A4,beta4,iangle(3),sangle(4),dh_il3,dh_df3,dP_fl3,dh_fl3] = CompressorRotor(fluid,Cp(2),P(2),T2_out,m(2),V(2),rho(2),T0(2),P0(2),Mach(2));

% The Diffuser:
[Cp(6),Cp(5),h0(5),h0(6),P(6),T(6),m(5),m(6),rho(6),T0(5),P0(5),P(5),T(5),V(5),rho(5),Mach(5),Mach(6),T0(6),P0(6),V(6),iangle(5),sangle(6),dh_il5,dh_fl6,dP_fl6] = CompressorStator(fluid,Cp(4),h0(2),P(4),T(4),rho(4),rho(4),T0(4),P0(4),V_radial(4),V_tan(4),A4,T0(2),P0(2),T(2),P(2));

% The Combustion Chamber:
[P(7),T(7),m(7)] = Combustion(P(6),m(6),m_fuel,RPM);

% The TurbineStator:
[Cp(7),Cp(8),Cp(9),h0(7),h0(8),h0(9),V(7),P0(7),T0(7),rho(7),Mach(7),P(9),T(9),m(9),m(8),V(9),V(8),rho(9),P0(9),T0(9),T0(8),T(8),P(8),Y9_tan,V9_axial,h(8),h(9),Mach(8),Mach(9),iangle(8),sangle(9),alfa9,dh_il8,dh_fl9,h7] = TurbineStator(fluid,P(7),T(7),m(7));

% The TurbineRotor:

```



```

% The Nozzle function is applied in the 'main file' of our 6th semester
% project.
% it models the exhaust nozzle of the jet engine
% The Thrust is calculated without concerning the ambient velocity, because
% this is none in this project.
function [Cp12,h012,P12,T12,P012,T012,rho12,m12,V12,Thrust,Mach12] = Nozzle(fluid,
P_atm,P11,T11,P011,T011,m11);

m12=m11;
T012=T011;
P012=P011;
P12=P_atm;

##### measurements

r12 = 0.054283/2; %radius of the outlet surface
A12= pi*r12^2; %m^2

%% 12. NOZZLE OUTLET
rho12=refprop('D','T',T11,'P',P12,fluid);%kg/m3
kappa=1.4; Mach12=0.8; T12=T11; % guess values

tolerance = 1e-10; error12=i; i=1;
while tolerance<error12(i);
V12(i+1) = m12/(A12*rho12(i)); %m/s
kappa(i+1) = refprop('K','T',T12(i)+T11)/2,'P',(P12+P11)/2,fluid); %Cv/Cp [-]
Cp12(i) = refprop('C','T',T12(i)+T11)/2,'P',(P12+P11)/2,fluid); %J/kg*K
P012(i+1)=P12*(1+(kappa(i+1)-1)/2*Mach12(i)^2)/(2*Cp12(i)); %kPa
T12(i+1) = T012 - (V12(i+1))^2/(2*Cp12(i)); %K
Mach12(i+1) = V12(i+1)/refprop('A','T',T12(i+1),'P',P12,fluid);
rho12(i+1)=refprop('D','T',T12(i+1),'P',P12,fluid); %kg/m^3

error_matrix12(i,:)=abs([0 (T12(i)-T12(i+1))/T12(i) 0 0 (V12(i)-V12(i+1))/V12(i)
(rho12(i)-rho12(i+1))/rho12(i) Mach12(i)-Mach12(i+1))/Mach12(i)]);
error12(i+1,1) = max(error_matrix12(i,:));
i=i+1;
end

% Definition of the results that are given as outputs
T12 = T12(i); V12 = V12(i); rho12 = rho12(i); Mach12=Mach12(i); Cp12=Cp12(i-1);
P012=P012(i);

### Enthalpies
h12=refprop('H','T',T12,'P',P12,fluid); %[J/kg]
h012 = h12 + V12^2/2; %[J/kg]

##### thrust created by the engine
Thrust = m12*V12; % N the engine is assumed to have a null velocity

```

```

% The TurbineRotor function is applied in the 'main file' of our 6th semester
% project.
% it models the rotor of the jet engine
function [Cp10,Cp11,h010,h011,P11,T11,m11,V11_abs,rho11,P011,T011,P010,T10,P10,P10,
rho10,V10_abs,Mach10,Mach11,incidenceangle10,sangle11,dh_ill0,dh_fll0,dh_sfl1,R9,
Workreal] = TurbineRotor(fluid,Cp9,P9,T9,m9,V9_tan,V9_axial,P09,T09,RPM,h9,T07,P07,T7,
P7,R7);
m10=m9; m11=m9;

%% 10. ROTOR INLET

##### Dimensions : Measured from Solidworks
InnerD10 = 65.71e-3; % inner diameter
OuterD10 = 89.91e-3; % outer diameter
Bladeheight10 = (OuterD10-InnerD10)/2; %Measure from Solidworks
A10 = InnerD10*pi*Bladeheight10;

% Calculation of the blade speed U10 :
Tip_speed10 = RPM*2*pi/60*(InnerD10+OuterD10)/4; %m/s
U10 = [-Tip_speed10 0]; %m/s

##### Velocity triangles
W9 = [V9_tan-U10(1) V9_axial]; %m/s
beta9 = -atan(W9(1)/W9(2)); %rad
beta10=(56.92-6)/180*pi; %rad
W10 = [-V9_axial*tan(beta10) V9_axial]; %m/s
V10_vec = [W10(1)+U10(1) W10(2)]; %m/s
V10_abs = vecl(V10_vec); %m/s

##### Incidence Loss
incidenceangle10 = (beta9-beta10)/pi*180; %degrees
dh_ill0 = 1/2*(W9(1)-W10(1))^2; %J/kg

##### Iterations
rho10=refprop('D','T',T9,'P',P9,fluid);T10=T9;P10=P9; % guess values
tolerance = 1e-5; error10 = 1; i=1;
while tolerance<error10(i);
Cp10(i) = Cp9; %J/kg*K
T10(i+1) = T9-dh_ill0/Cp10(i); %K
T010(i+1) = T10(i+1)+V10_abs^2/(2*Cp10(i)); %K
Mach10(i+1) = V10_abs/refprop('A','T',T10(i+1),'P',P10(i),fluid);
kappa(i+1) = refprop('K','T',T9+T10(i))/2,'P',(P9+P10(i))/2,fluid); %Cv/Cp [-]
P010(i+1)=P09*(T010(i+1)/T09)^(kappa(i+1)/(kappa(i+1)-1)); %kPa
P10(i+1)=P010(i+1)/(1+(kappa(i+1)-1)/2*Mach10(i+1)^2)/(kappa(i+1)/(kappa(i+1)-1)); %
kPa
rho10(i+1)=refprop('D','T',T10(i+1),'P',P10(i+1),fluid); %kg/m3

error_matrix10(i,:)=abs([((P10(i)-P10(i+1))/P10(i) (T10(i)-T10(i+1))/T10(i)
P010(i+1)/P010(i) (T010(i)-T010(i+1))/T010(i) 0 (rho10(i)-rho10(i+1))/rho10(i)
(Mach10(i)-Mach10(i+1))/Mach10(i) 0)];
error10(i+1,1) = max(error_matrix10(i,:));
i=i+1;
end

```

```

%Plot of the error matrix
% errormatrix_size=size(error_matrix10);
% iterations=(1:l:errormatrix_size(1));
% figure(13)
% plot(iterations,error_matrix10), axis([1 errormatrix_size(1) 0 0.2]); legend
('P','T','P0','T0','m','V','rho','Mach'); title('Error as a function of
iterations','fontSize',13); xlabel('Iterations','fontSize',11); ylabel
('Errors','fontSize',11);

T10 = T10(i); P10=P10(i); rho10 = rho10(i); Mach10=Mach10(i); V10_tan=V10_vec(1);
P010=P010(i); T010=T010(i); Cp10=Cp10(i-1);

% Enthalpies
h10=refpropm('H','T',T10,'P',P10,fluid); %[J/kg]
h010 = h10 + V10_abs^2/2; %[J/kg]

W10b=vec1(W10);

% PLOTS of the Velocity triangles:
% W10_vec = W10;
% V10_vec_plot = [-V10_vec(1) 0; 0 V10_vec(2)]; W10_vec_plot = [-W10_vec(1) 0; 0
W10_vec(2)]; U10_plot = [-V10_vec(1) 0;-V10_vec(1)+U10(1) U10(2)]; Blade10_plot = [0
V10_vec(2); 0-100*sin(beta10) V10_vec(2)+100*cos(beta10)];
% V9_vec=[V9_tan V9_axial]; W9_vec = V9_vec-U10;
% V9_vec_plot = [-V9_vec(1) 0; 0 V9_vec(2)]; W9_vec_plot = [-W9_vec(1) 0; 0 W9_vec
(2)]; U9_plot = [-V9_vec(1) 0;-V9_vec(1)+U10(1) U10(2)]; Blade9_plot = [-V9_vec(1) 0;-
V9_vec(1)+100*sin(alpha9) 0-100*cos(alpha9)];

% figure(14)
% plot(Blade9_plot(:,1),Blade9_plot(:,2),'black',Blade10_plot(:,1),Blade10_plot(:,
2),'black')
% hold on
% plot(W9_vec_plot(:,1),V9_vec_plot(:,2),'b',W9_vec_plot(:,1),W9_vec_plot(:,2),'r',
U9_plot(:,1),U9_plot(:,2),'c')
% plot(W10_vec_plot(:,1),V10_vec_plot(:,2),'b',W10_vec_plot(:,1),W10_vec_plot(:,
2),'r',U10_plot(:,1),U10_plot(:,2),'c')
% title('Velocity Triangle at the Inlet of the Rotor','FontSize',13)
% legend('Stator blade \alpha_9 = 71^\circ','Rotor blade \beta_10 =
62^\circ','V_9','W_9','U_{10}','V_{10}','W_{10}','U_{10}'); axis('equal')
% xlabel('Tangential velocity [m/s]','FontSize',11),ylabel('Axial velocity
[m/s]','FontSize',11)

% 11. ROTOR OUTLET
% Dimensions : Measured from Solidworks
InnerD11 = 67.869e-3; %m inner diameter
OuterD11 = 89.915e-3; %m outer diameter
Bladeheight11 = (OuterD11-InnerD11)/2; %Measure from Solidworks
All = InnerD11*pi*Bladeheight11; %m2 outlet area

% calculation of the blade speed U :
Tip_speed11 = RPW*2*pi/60 * (InnerD11+OuterD11)/4; %m/s
U11 = [-Tip_speed11 0]; %m/s

```

```

% Friction loss
% Mean dimensions
A_mean = (All+All0)/2; %Mean area of in- and outlet
width10 = ((InnerD10+OuterD10)/2)*pi/26; % Width at impeller inlet
width11 = ((InnerD11+OuterD11)/2)*pi/26; % Width at impeller outlet
w_mean = (width10+width11)/2; %Mean width of impeller channels
h_mean = (Bladeheight11+Bladeheight10)/2;
Dh = 2*A_mean/(w_mean+h_mean);
l_mean = 60e-3; % m Mean channel length; MUST BE FOUND
% calculation of the friction coefficient
syms f
visk10 = refpropm('V','T',T10,'P',P10,fluid)/rho10; %Pa.s
Re = V10_abs*Bladeheight11/visk10; %Article_noref
epsilon = 0.000045; %m ASSUMPTION, it is the roughness of commercial steel taken from
an exercise in strammingslære
% Friction factor f from Colebrook and White
f=solve(1/(f^(1/2))+2*log((epsilon/Dh)*0.2703+2.51/(Re*sqrt(f))),f); % Colebrook and
White, Ferguson page 51
f=eval(f);

% Velocity triangles
% We eliminate the radial dimension in order to get 2-dimensional velocity triangles
T11=T10; P11=P10; rho11=refpropm('D','T',T10,'P',P10,fluid); Mach11=0.5; kappa=1.4;
T011=T09; P011=P09; % guess values
error11=1; i=1;
while tolerance<error11(i);
V11_axial(i) = m11/(All*rho11(i)); %m/s
beta11 = 61.76/180*pi; %rad
W11(i+1) = V11_axial(i)/cos(beta11); %m/s
slipfactor11 = 1-sqrt(cos(beta11))/(26)^0.7; % slip factor
W11_tan(i+1) = W11(i+1)*sin(beta11); %m/s
V11_tan(i+1) = (W11_tan(i+1)+U11(1))*slipfactor11; %m/s
V11_abs_vec(i+1,:) = [V11_tan(i+1); V11_axial(i)]; %m/s
V11_abs(i+1)=vec1(V11_abs_vec(i+1,:)); %m/s

% All stage 9 should be changed to stage 10, but they are done like this as
% the incidence loss have a bad impact on stage 10

% Friction Loss
W_mean = (vec1(W10)+W11(i))/2; % Mean relative velocity
dh_f110(i) = (f*1_mean*W_mean^2/(2*Dh))*12; %J/kg
dP_f110(i) = (f*1_mean*W_mean^2/(2*Dh))*(rho10+rho11(i))/2)*12*1e-3; %kPa

% Disc Friction "The Centrifugal Pump" Grundfos
visk11(i) = refpropm('V','T',T11(i),'P',P11(i),fluid)/rho11(i);
m_disc = 1/6; % smooth surface
e_disc = 0.5e-3; % axial distance to wall at the periphery of the impeller
r_mean = ((OuterD10+InnerD10)/4+(InnerD11+OuterD11)/4)/2;
k = 7.3*10^-4*(visk10+visk11(i))/2*10^6/(abs(U11(1))*r_mean))^(-m_disc); %[-]
dh_df11(i) = k*(rho10+rho11(i))/2*abs(U11(1))^3*r_mean^2*(r_mean^2+5*e_disc)/m10; %J/kg

```

```

%work calculations
Work(i) = -(U10(i)*V10_tan(i))-(U11(i)*V11_tan(i+1)); %J/kg
W_loss = dh_dfl1(i)+dh_fl10(i); %J/kg
Workreal(i)=Work(i)+W_loss; %J/kg

etall(i)=1+W_loss/(Work(i));
Cp11(i) = refpropm('C','T',(T10+T11(i))/2,'P',(P10+P11(i))/2,fluid); %J/kg*K
kappa(i+1) = refpropm('K','T',(T10+T11(i))/2,'P',(P10+P11(i))/2,fluid); %Cv/Cp [-]
T011s(i+1) = T010 + Work(i)/Cp11(i); %K isentropic temperature
T011(i+1) = T09 - etall(i) * (T09 - T011s(i+1)); %K
T11(i+1) = T011(i+1) - V11_abs(i+1)^2/(2*Cp11(i)); %K
Mach11(i+1) = V11_abs(i+1)/refpropm('A','T',T11(i+1),'P',P11(i),fluid);
P011(i+1) = P010*(T011s(i+1)/T010)^(kappa(i)/(kappa(i)-1))-qp_fl10(i); %kpa
P11(i+1) = P011(i+1)/((1+(kappa(i)-1)/2*Mach11(i+1)^2)^(kappa(i)/(kappa(i)-1))); %kpa
rho11(i+1)=refpropm('D','T',T11(i+1),'P',P11(i+1),fluid); %kg/m3

error_matrix11(i,:)=abs((P11(i)-P11(i+1))/P11(i) (T11(i)-T11(i+1))/T11(i) (P011(i)-P011(i+1))/P011(i) (T011(i)-T011(i+1))/T011(i) 0 ((V11_abs(i)-V11_abs(i+1))/(V11_abs(i)
(i) (rho11(i)-rho11(i+1))/rho11(i) (Mach11(i)-Mach11(i+1))/Mach11(i) 0 ));
error11(i+1,1) = max(error_matrix11(i,:));
i=i+1;
end

W11 = V11_abs(i)-U11; %relative velocity
sangle11 = (beta11-atan(W11(1)/W11(2)))*180/pi; % degree deviation angle
disp('The ratio of throat areas in the turbine rotor, used to characterise the
reaction stage')
Ratio_Throatareas =A10*cos(beta10)/(A11*cos(beta11));

%plot of the errors matrix
% errormatrix size=size(error_matrix11);
% iterations=(1:1:errormatrix_size(1));
% figure(i5)
% plot(iterations,error_matrix11, axis([1 errormatrix_size(1) 0 0.2]); legend
('P','T','P0','T0','m','V','rho','Mach'); title('Error as a function of
iterations','fontsize',13); xlabel('Iterations','fontsize',11); ylabel
('Errors','fontsize',11);
dv=V10_tan - V11_tan(i);

%% Definition of the results that are given as outputs
P11=P11(i); Mach11=Mach11(i); T11=T11(i); V11_abs=vecl(V11_abs_vec(i,:)); rho11=rho11
(i); T011s=T011s(i); P011=P011(i); T011=T011(i); Work=Work(i-1); Cp11 = Cp11(i-1);
dh_fl10=dh_fl10(i-1);
dh_dfl1=dh_dfl1(i-1);
dp_fl10=dp_fl10(i-1);
etall=etall(i-1);
T11s = T011s - V11_abs^2/(2*Cp11);
Workreal=Workreal(i-1);
visk11=visk11(i-1);

% Enthalpies
h11 = refpropm('H','T',T11,'P',P11,fluid); %[J/kg]
h011 = h11 + V11_abs^2/2;

```

```

h07 = refpropm('H','T',T07,'P',P07,fluid);
T011s = (P011/P07)^(kappa(i)-1)/kappa(i)*T07;
h011s = refpropm('H','T',T011s,'P',P011,fluid); %[J/kg]

% Total to Total efficiency of the turbine
eta_turbine = (h07-h011)/(h07-h011s)

% Reaction stage
sprintf('The area ratio of A10 over A11 is %d',A10/A11)
disp('The reaction stage : ')
R9= (h10 - h11)/((h7-h9)+(h10-h11))

```

```

% The TurbineStator function is applied in the 'main file' of our 6th semester
% project.
% It models the stator of the jet engine
function(Cp7,Cp8,Cp9,h07,h08,h09,v7,P07,T07,rho7,Mach7,P9,T9,m9,m8,v9,v8_abs,rho9,P08,
P09,T08,T09,rho8,T8,P8,v9_tan,v9_axial,h8,h9,Mach8,Mach9,incidenceangle8,sangle9,alpha9,
dh_il8,dh_fl9,h7) = TurbineStator(fluid,P7,T7,m7);

m8=m7; m9=m7;

%% 8. INLET OF THE STATOR %%

%% Dimensions : Measured from Solidworks
Innerradius8 = (88.186*1e-3)/2; %Inner radius
Outerradius8 = (88.252*1e-3)/2; %outer radius
% We neglect the bladearea, due to the aerodynamic shape.
A8 = Outerradius8^2*pi-Innerradius8^2*pi; % inlet area
Bladeheight8=Outerradius8-Innerradius8; % height of the blade

%%%%%%%%%%%%%%%%%%%%%%%%%%%%%%%%%%%%%%%%%%%%%%%%%%%%%%%%%%%%%%%%%%%%%%%%%%%%%%
%% calculation of the velocity and stagnation properties from the combustion chamber
%%
rho7 = repropm('D','T',T7,'P',P7,fluid);
% We assume that the area at outlet of combustion equals inlet of turbine stator.
% Furthermore, the velocity V7 is assumed purely axial.
V7 = m7/(A8*rho7); % Axial velocity
kappa7 = repropm('K','T',T7,'P',P7,fluid); % Ratio of specific heats
Mach7 = V7/repropm('A','T',T7,'P',P7,fluid);
P07 = (1+(kappa7-1)/2*Mach7^2)^(kappa7/(kappa7-1))*P7; % Stagnation pressure
T07 = (P07/P7)^(kappa7-1)/kappa7)*T7; % Stagnation temperature
Cp7 = repropm('C','T',T7,'P',P7,fluid); %J/kg*K

% Enthalpies of the combustion chamber
h7 = repropm('H','T',T7,'P',P7,fluid); %J/kg*K
h07 = h7 + V7^2/2; %J/kg.K

%%%%%%%%%%%%%%%%%%%%%%%%%%%%%%%%%%%%%%%%%%%%%%%%%%%%%%%%%%%%%%%%%%%%%%%%%%%%%%
%% Velocity triangles at the inlet of the stator
%The radial dimension is eliminated in order to get 2-dimensional velocity triangles
V8_axial = V7; %m/s
alpha8=(12.33+22.71)/2+6)/180*pi; %rad. when the ideal blade angle is -6°
V8_tan = -V8_axial*tan(alpha8); %m/s
V8_abs_vec=[V8_tan V8_axial]; %m/s
V8_abs = vec1(V8_abs_vec); %m/s

%%Incidence Loss
incidenceangle8 = alpha8*180/pi;
dh_il8 = 1/2*(-V8_abs_vec(1))^2; %J/kg The tangential component of V7 is assumed zero.

%%Iteration
rho8=repropm('D','T',T7,'P',P7,fluid); kappa=1.4; Mach8=0.4; P8=P7; T8=T7; % guess
values
tolerance = 1e-3; error8=1; i=1;

```

```

while tolerance<error8(i);
Cp8(i) = Cp7; %J/kg*K
T8(i+1) = T7 - dh_il8/Cp8(i); %K
T08(i+1)=T8(i+1)+V8_abs^2/(2*Cp8(i)); %K
Mach8(i+1) = V8_abs/repropm('A','T',T8(i+1),'P',P8(i+1),fluid); %Cv/Cp [-]
kappa(i+1) = repropm('K','T', (T7+T8(i))/2,'P', (P7+P8(i))/2,fluid); %Cv/Cp [-]
P08(i+1)=P07*(T08(i+1)/T07)^((kappa(i+1)-1)/(kappa(i+1)-1)); %kPa
P8(i+1)=P08(i+1)/((1+(kappa(i+1)-1)/(2*Mach8(i+1)^2)^(kappa(i+1)/(kappa(i+1)-1)))); %kPa
rho8(i+1)=repropm('D','T',T8(i+1),'P',P8(i+1),fluid); %kg/m3

error_matrix8(i,:)=abs([(P8(i)-P8(i+1))/P8(i) (T8(i)-T8(i+1))/T8(i) (P08(i)-P08(i+1))/
P08(i) (T08(i)-T08(i+1))/T08(i) 0 (rho8(i)-rho8(i+1))/rho8(i) (Mach8(i)-Mach8(i+1))/
Mach8(i) 0]);
error8(i+1,l) = max(error_matrix8(i,:));
i=i+1;
end

%plot of the error matrix
% error_matrix_view=error_matrix8*1e3
% errormatrix size=size(error_matrix8);
% iterations=(1:1:errormatrix_size(1));
% figure(11)
% plot(iterations,error_matrix8), axis([1 errormatrix_size(1) 0 0.2]); legend
('P','T','P0','T0','m','v','rho','Mach'); title('Error as a function of
iterations','fontsize',13); xlabel('Iterations','fontsize,11); ylabel
('Errors','fontsize,11);

T8 = T8(i); P8=P8(i); rho8=rho8(i); Mach8=Mach8(i); T08=T08(i); P08=P08(i); Cp8=Cp8(i-1);

%% Enthalpies
h8 = repropm('H','T',T8,'P',P8,fluid); %J/kg*K An average value over the stator
h08 = h8 + V8_abs^2/2;

%% 9. STATOR OUTLET %%

%% Dimensions : Measured from Solidworks
Innerradius9 = 68.186/2*1e-3; % Measure from Solidworks
Outerradius9 = 88.252/2*1e-3;
A9 = Outerradius9^2*pi-Innerradius9^2*pi;
Bladeheight9=Outerradius9-Innerradius9;

%%Friction loss
%Mean dimensions
A_mean = (A9+A8)/2; %Mean area of in- and outlet
w8 = (Innerradius9+Outerradius8)/2*pi/21; %Width of stator outlet
w9 = (Innerradius9+Outerradius9)/2*pi/21; %Width of stator outlet
w_mean = (w8+w9)/2; %Mean width of impeller channels
h_mean = (Bladeheight8+Bladeheight9)/2; %mean height
Dh = 2*A_mean/(w_mean*h_mean);
l_mean = 285*1e-3; % m Mean channel length;
% calculation of the friction coefficient
syms f

```

```

visk8 = refpropm('V','T','P',P8,fluid)/rho8; %Pa.s
Re = V8_abs*Dh/visk8; %Reynold number
epsilon = 0.000045; %m ASSUMPTION, it is the roughness of commercial steel taken from
an exercise in strömingsläre
% Friction factor f from Colebrook and White
f=solve(1/(f*(1/2))+2*log((epsilon/Dh)*0.2703+2.51/(Re*sqrt(f))),f); % Colebrook and
White, Ferguson page 51
f=eval(f);

%%Velocity triangle
% We eliminate the radial dimension in order to get 2-dimensional velocity triangles
T9=T9; P9=207; rho9=refpropm('D','T',T9,'P',P9,fluid); kappa=1.35; Mach9=0.96; % guess
values
P09=P08; T09=T08;

error9=1; i=1;
clear Cp;
while tolerance<error9(i);
V9_axial(i) = m9/(A9*rho9(i)); %m/s
alfa9 = (71.09+71.11)/(2*180)*pi; %m/s
deviation9 = 1-sqrt(cos(alfa9))/(21)^0.7;
V9_tan(i+1) = -V9_axial(i)*tan(alfa9)*deviation9; %m/s
V9_abs_vec(i+1,:) = [V9_tan(i+1) V9_axial(i)]; %m/s
V9_abs(i+1) = vec1(V9_abs_vec(i+1,:)); %m/s

%%Friction Loss
V_mean(i+1) = (V9_abs(i+1)+V8_abs)/2; % Mean absolute velocity
dP_f19(i) = f*V_mean(i+1)^2*1_mean/(2*Dh)*(rho8+rho9(i))/2*1e-3*21; %kPa
dh_f19(i) = f*V_mean(i+1)^2*1_mean/(2*Dh)*21; %J/kg

Cp9(i) = refpropm('C','T',(T8+T9(i))/2,'P',(P8+P9(i))/2,fluid); %J/kg*K
T9(i+1)=T09(i) - V9_abs(i+1)^2/(2*Cp9(i)) + dh_f19(i)/Cp9(i); %K
T09(i+1)=T08*(P09(i)/P08)^(kappa(i)-1)/kappa(i); %K
Mach9(i+1) = (V9_abs(i+1))/refpropm('A','T',T9(i+1),'P',P9(i),fluid);
kappa(i+1) = refpropm('K','T',(T8+T9(i+1))/2,'P',(P8+P9(i))/2,fluid); %Cv/Cp [-]
P09(i+1)=P08 - dP_f19(i); %kPa
P9(i+1)=P09(i+1)/(1+(kappa(i+1)-1)/2*(Mach9(i+1))^2)^(kappa(i+1)/kappa(i+1)-1)); %kPa
rho9(i+1)=refpropm('D','T',T9(i+1),'P',P9(i+1),fluid); %kg/m^3

error_matrix9(i,:)=[(P9(i)-P9(i+1))/P9(i) (T9(i)-T9(i+1))/T9(i) (V9_abs(i)-V9_abs(i+1))
/V9_abs(i) (rho9(i)-rho9(i+1))/rho9(i) (Mach9(i)-Mach9(i+1))/Mach9(i)];
error9(i+1,i) = max(abs(error_matrix9(i,:)));
i=i+1;
end
sangla9 = (atan(-V9_abs_vec(i,1)/V9_abs_vec(i,2))-alfa9)*180/pi; % deviation angle

%Plot of the error matrix
% errormatrix_size=size(error_matrix9);
% iterations=(1:i:errormatrix_size(i));
% figure(i2)
% plot(iterations,error_matrix9, axis([1 errormatrix_size(i) -0.12 0.12]); legend
('P','T','V','rho','Mach'); title('Error as a Function of Iterations','fontsize',13);
xlabel('Iterations','fontsize',11); ylabel('Errors','fontsize',11);

```

```

% Definition of the results that are given as outputs
P9=P9(i); T9=T9(i); V9=V9_abs(i); Cp9=Cp9(i-1);
rho9=rho9(i); V9_tan = V9_tan(i);P09=P09(i);T09=T09(i);
Mach9=Mach9(i); V9_axial=V9_axial(i-1);
dh_f19=dh_f19(i-1);

%%Enthalpies
h9 = refpropm('H','T',T9,'P',P9,fluid); %J/kg*K An average value over the stator
h09 = h9 + V9^2/2; %J/kg*K

```

# Test Run of the SR-30 Engine B

The appendix will be dealing with the tests on the SR-30 turbojet engine. The jet engine is mounted in a test stand with pre-installed sensors. An overview of the sensors are listed in figure B.3. Data can be logged from these sensors by software delivered by the manufacturer, Turbine Technologies. Figure B.1 shows the interface of the program and the pre-installed sensor locations.

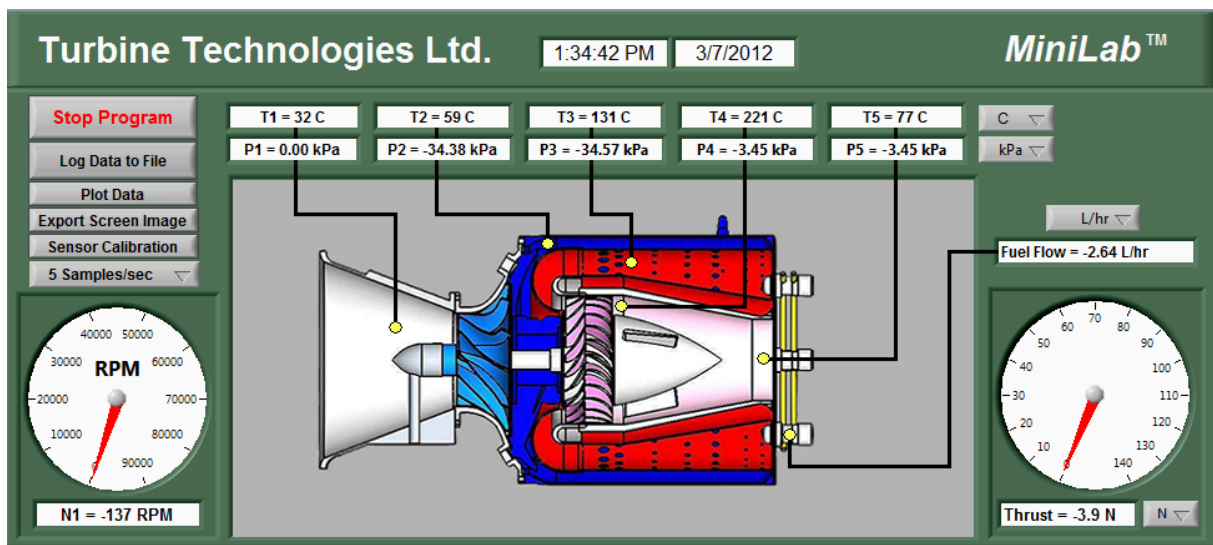
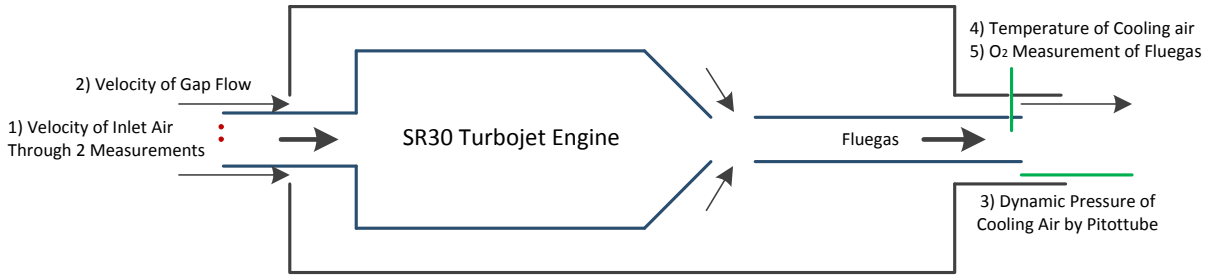


Figure B.1. Interface of the program, Minilab, supplied by Turbine Technologies.

Additional measurements were made during the tests in order to enable proper modeling of the combustion. The location of the probes used are shown in figure B.2. These measurements included the:

- 1) Speed of the flow into the turbine through the silencer.
- 2) Speed through the gap between silencer and the casing.
- 3) Dynamic pressure in the outer tube of the exhaust pipe.
- 4) The temperature of the cooling air leaving the exhaust pipe.
- 5) The O<sub>2</sub> content in the flue gas.



**Figure B.2.** Illustration of the test stand with locations of measurements

To ensure compatibility in between the results, all the measurements were done at the same time. To see how the engine performed at different stages, the fuel flow was increased by a certain range of RPM's. As the transient periods is not modeled the data in those periods are not included for comparison and only data from the steady states are used for comparison.

The velocity of the flow at the inlet was measured at the middle of the flow and at a half radius, while the gap flow was measured above and under the silencer. This was done to investigate if the velocity profile had any impact at the two locations. The dynamic pressure measured in the exhaust pipe, denoted by 3) in figure B.2, was used to calculate the velocity of the exhaust gas in the outer tube of the exhaust pipe.

A list of the devices used for measuring, are located in table B.1, while the sensors in the jet engine are listed in figure B.3. It is worth a notice that the inlet pressure and the temperature in the combustion chamber are not stagnation quantities like the rest of the sensors.

Measurement	Device	Accuracy
O <sub>2</sub> content	Servomex A570	1% at one digit
Dynamic Pressure	Testo 512	0.5% of f.s.v
Temperature	Eirelec LTD	-
Velocity	Swema air 30	5%

**Table B.1.** Specifications on accuracy from manuals.

**TABLE A  
Sensor List**

<b>Symbol</b>	<b>Function</b>	<b>Manufacturer/type</b>	<b>Range (PSIG)</b>	<b>Output (V)</b>
P <sub>1</sub>	Compressor inlet Pitot/static probe	Setra Model 256	0-1	0 - 5
P <sub>02</sub>	Compressor exit Stagnation probe	Setra Model 209	0-50	0.5 - 5.5
P <sub>3</sub>	Combustion chamber Static port	Setra Model 209	0-50	0.5 - 5.5
P <sub>04</sub>	Turbine stage exit Stagnation probe	Setra Model 209	0-5	0.5 - 5.0
P <sub>05</sub>	Thrust nozzle exit Stagnation probe	Setra Model 209	0-5	0.5 - 5.0
RPM	Engine shaft speed	TTL generator	52,000 rpm 60,000 rpm 70,000 rpm 80,000 rpm	4.50 Volts 5.28 Volts 6.07 Volts 6.89 Volts
FFS	Fuel flow sensor	Setra Model 209	0-200	0.5 - 5.5
T <sub>f</sub>	Thrust force	TTL strain gage thrust yoke system	Calibrate to panel meter	0-100 mV
T <sub>1</sub>	Compressor Inlet	K-type thermocouple Alumel-Chromel	mV	
T <sub>02</sub>	Compressor exit Stagnation probe	K-type thermocouple	mV	
T <sub>03</sub>	Turbine stage inlet Stagnation probe	K-type thermocouple	mV	
T <sub>04</sub>	Turbine stage exit Stagnation probe	K-type thermocouple	mV	
T <sub>05</sub>	Thrust nozzle exit Stagnation probe	K-type thermocouple	mV	

*Figure B.3.* sensor specifications from Turbine Technologies



# Combustion Calculations by CEA NASA

---

The combustion chamber is modeled in CEA NASA at different RPM. The inlet pressure, inlet temperature and the AF ratio are implemented in CEA NASA in order to determine the adiabatic flame temperature. The input parameters are listed in table C.1 along with the RPM.

RPM [ $\text{min}^{-1}$ ]	Temperature [K]	Pressure [kPa]	AF ratio [.]
45,000	325.5	159.2	91.0
50,000	335.0	175.7	86.2
55,000	345.3	194.9	82.8
60,000	356.2	217.0	80.4
65,000	367.9	242.5	78.5
70,000	380.3	272.0	77.1
75,000	393.7	306.3	75.9
80,000	408.1	346.7	74.9
85,000	423.7	394.5	74.1

*Table C.1.* The CEA NASA input parameters.

In the following, parts of the output files from CEA NASA are shown. Here the input parameters and the output adiabatic flame temperature can be seen. In appendix F the full output files from CEA NASA are to be found.

For an RPM of 45,000 the combustion products from the output file are shown in order to see that the amount of combustion products other than Ar, CO<sub>2</sub>, H<sub>2</sub>O, NO, N<sub>2</sub> and O<sub>2</sub> is lower than 5 ppm. It can be seen that air in CEA NASA includes argon, however, argon is neglected in the combustion calculations due to the small mole fraction. The combustion products are only shown in the output file for 45,000 RPM. In the other output files only inlet parameters and adiabatic flame temperature are shown.

RPM = 45,000:

CASE =

	REACTANT	MOLES	ENERGY KJ/KG-MOL	TEMP K
FUEL	JP-4	0.0002690	-22723.000	298.000
OXIDANT	Air	0.0004001	598.134	323.000

O/F= 73.00166 %FUEL= 1.351321 R,EQ.RATIO= 0.202614 PHI,EQ.RATIO= 0.201400

THERMODYNAMIC PROPERTIES

P, BAR 1.5559  
T, K 868.55  
MOLE FRACTIONS

\*Ar 0.00924  
\*CO2 0.02834  
H2O 0.02718  
\*NO 0.00001  
\*N2 0.77022  
\*O2 0.16501

\* THERMODYNAMIC PROPERTIES FITTED TO 20000.K

PRODUCTS WHICH WERE CONSIDERED BUT WHOSE MOLE FRACTIONS  
WERE LESS THAN 5.000000E-06 FOR ALL ASSIGNED CONDITIONS

*C	*CH	CH2	CH3	CH2OH
CH3O	CH4	CH3OH	CH3OOH	*CN
CNN	*CO	COOH	*C2	C2H
C2H2,acetylene	C2H2,vinylidene	CH2CO, ketene	O(CH)2O	HO(CO)2OH
C2H3,vinyl	CH3CN	CH3CO,acetyl	C2H4	C2H4O,ethylen-o
CH3CHO,ethanal	CH3COOH	OHCH2COOH	C2H5	C2H6
CH3N2CH3	C2H5OH	CH3OCH3	CH3O2CH3	CCN
CNC	OCCN	C2N2	C2O	*C3
C3H3,1-propynl	C3H3,2-propynl	C3H4,allene	C3H4,propyne	C3H4,cyclo-
C3H5,allyl	C3H6,propylene	C3H6,cyclo-	C3H6O,propylox	C3H6O,acetone
C3H6O,propanal	C3H7,n-propyl	C3H7,i-propyl	C3H8	C3H8O,1propanol
C3H8O,2propanol	CNCOCN	C3O2	*C4	C4H2,butadiyne

C4H4,1,3-cyclo-	C4H6,butadiene	C4H6,1butyne	C4H6,2butyne	C4H6,cyclo-
C4H8,1-butene	C4H8,cis2-buten	C4H8,tr2-butene	C4H8,isobutene	C4H8,cyclo-
(CH3COOH)2	C4H9,n-butyl	C4H9,i-butyl	C4H9,s-butyl	C4H9,t-butyl
C4H10,n-butane	C4H10,isobutane	C4N2	*C5	C5H6,1,3cyclo-
C5H8,cyclo-	C5H10,1-pentene	C5H10,cyclo-	C5H11,pentyl	C5H11,t-pentyl
C5H12,n-pentane	C5H12,i-pentane	CH3C(CH3)2CH3	C6H2	C6H5,phenyl
C6H5O,phenoxy	C6H6	C6H5OH,phenol	C6H10,cyclo-	C6H12,1-hexene
C6H12,cyclo-	C6H13,n-hexyl	C6H14,n-hexane	C7H7,benzyl	C7H8
C7H8O,cresol-mx	C7H14,1-heptene	C7H15,n-heptyl	C7H16,n-heptane	C7H16,2-methylh
C8H8,styrene	C8H10,ethylbenz	C8H16,1-octene	C8H17,n-octyl	C8H18,n-octane
C8H18,isoctane	C9H19,n-nonyl	C10H8,naphthale	C10H21,n-decyl	C12H9,o-bipheny
C12H10,biphenyl	*H	HCN	HCO	HCCN
HCCO	HNC	HNCO	HNO	HNO2
HNO3	HO2	*H2	HCHO,formaldehy	HCOOH
H2O2	(HCOOH)2	*N	NCO	*NH
NH2	NH3	NH2OH	NO2	NO3
NCN	N2H2	NH2NO2	N2H4	N2O
N2O3	N2O4	N2O5	N3	N3H
*O	*OH	O3	C(gr)	H2O(cr)
H2O(L)				

RPM = 50,000:

CASE =

	REACTANT	MOLES	ENERGY KJ/KG-MOL	TEMP K
FUEL	JP-4	0.0002690	-22723.000	298.000
OXIDANT	Air	0.0004001	860.497	332.000

O/F= 69.77947 %FUEL= 1.412839 R, EQ. RATIO= 0.211900 PHI, EQ. RATIO= 0.210700

THERMODYNAMIC PROPERTIES

P, BAR 1.7110  
T, K 899.26

RPM = 55,000:

CASE =

	REACTANT	MOLES	ENERGY KJ/KG-MOL	TEMP K
FUEL	JP-4	0.0002690	-22723.000	298.000
OXIDANT	Air	0.0004001	1152.211	342.000

O/F= 67.56679 %FUEL= 1.458432 R, EQ. RATIO= 0.218790 PHI, EQ. RATIO= 0.217600

THERMODYNAMIC PROPERTIES

P, BAR 1.8940  
T, K 924.72

RPM = 60,000:

CASE =

	REACTANT	MOLES	ENERGY KJ/KG-MOL	TEMP K
FUEL	JP-4	0.0002690	-22723.000	298.000
OXIDANT	Air	0.0004001	1473.363	353.000

O/F= 65.93065 %FUEL= 1.494084 R, EQ. RATIO= 0.224181 PHI, EQ. RATIO= 0.223000

THERMODYNAMIC PROPERTIES

P, BAR 2.1091  
T, K 947.24

RPM = 65,000:

CASE =

	REACTANT	MOLES	ENERGY KJ/KG-MOL	TEMP K
FUEL	JP-4	0.0002690	-22723.000	298.000
OXIDANT	Air	0.0004001	1824.065	365.000

O/F= 64.68339 %FUEL= 1.522455 R, EQ. RATIO= 0.228475 PHI, EQ. RATIO= 0.227300

THERMODYNAMIC PROPERTIES

P, BAR 2.3620  
T, K 967.84

RPM = 70,000:

CASE =

	REACTANT		MOLES	ENERGY KJ/KG-MOL	TEMP K
FUEL	JP-4		0.0002690	-22723.000	298.000
OXIDANT	Air		0.0004001	2204.453	378.000

O/F= 63.70249 %FUEL= 1.545536 R,EQ.RATIO= 0.231970 PHI,EQ.RATIO= 0.230800

THERMODYNAMIC PROPERTIES

P, BAR 2.6596  
T, K 987.30

RPM = 75,000:

CASE =

	REACTANT		MOLES	ENERGY KJ/KG-MOL	TEMP K
FUEL	JP-4		0.0002690	-22723.000	298.000
OXIDANT	Air		0.0004001	2614.695	392.000

O/F= 62.93893 %FUEL= 1.563992 R,EQ.RATIO= 0.234765 PHI,EQ.RATIO= 0.233600

THERMODYNAMIC PROPERTIES

P, BAR 3.0117  
T, K 1005.86

RPM = 80,000:

CASE =

	REACTANT		MOLES	ENERGY KJ/KG-MOL	TEMP K
FUEL	JP-4		0.0002690	-22723.000	298.000
OXIDANT	Air		0.0004001	3054.992	407.000

O/F= 62.27249 %FUEL= 1.580466 R,EQ.RATIO= 0.237262 PHI,EQ.RATIO= 0.236100

THERMODYNAMIC PROPERTIES

P, BAR 3.4292  
T, K 1024.51

RPM = 85,000:

CASE =

	REACTANT		MOLES	ENERGY KJ/KG-MOL	TEMP K
FUEL	JP-4		0.0002690	-22723.000	298.000
OXIDANT	Air		0.0004001	3525.582	423.000

O/F= 61.72348 %FUEL= 1.594299 R,EQ.RATIO= 0.239358 PHI,EQ.RATIO= 0.238200

THERMODYNAMIC PROPERTIES

P, BAR 3.9264  
T, K 1043.00

# Determining the Excess Air Ratio using the Inlet Mass Flow

# D

The AF ratio and  $\lambda$  are determined from equations (D.1) and (D.2) and thus the fuel consumption,  $m_{fuel}$ , and the inlet air mass flow,  $m_{air}$ , must be known along with the stoichiometric amount of air,  $m_s$ .

$$AF = \frac{m_{air}}{m_{fuel}} \quad [-] \quad (D.1)$$

$$\lambda = \frac{m_{air}}{m_s} \quad [-] \quad (D.2)$$

The fuel consumption is measured in the test runs, which are described in appendix B. The inlet air mass flow is determined by measuring the inlet velocity. The velocity is measured using a hand held hot wire anemometer and therefore some deviation is expected. The inlet pipe has a diameter of 155 mm and thus the velocity profile for the inlet cannot be neglected. To approximate the inlet velocity profile the velocity is measured at two points in the inlet area. One measurement is done in the middle of the inlet,  $v_{inlet1}$ , and another a fourth of the diameter from the middle,  $v_{inlet2}$ .

The results of velocities at inlet are given in table D.1 at different RPM. The difference in inlet velocity,  $\Delta v_{inlet}$ , is also given in the table.

RPM	$v_{inlet1}$ [m/s]	$v_{inlet2}$ [m/s]	$\Delta v_{inlet}$ [m/s]
39000	6.2	6.1	0.1
47500	7.6	7.5	0.1
52500	8.6	8.5	0.1
57200	9.6	9.5	0.1
59600	10.6	10.3	0.3
62800	10.8	10.6	0.2
68000	12.5	12.1	0.4
72300	13.3	12.9	0.4
74800	13.8	12.5	0.7
77500	14.8	14.3	0.5
79900	15.9	14.3	1.6

*Table D.1.* The test results showing the RPM and the velocities at inlet.

From the table it can be seen that the difference in velocity increases with RPM. The maximum velocity difference appears at the maximum RPM. Here the difference is 10 %. The lowest difference is 1.6 % at

the lowest RPM. Since the difference in the two velocity measurements is maximum 10 % the velocity profile is assumed to look like the one illustrated in figure D.1.

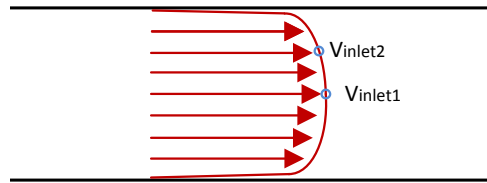


Figure D.1. A velocity profile for turbulent flow through a pipe. The location of the two velocity measurements are illustrated in the figure. (Munson et al., 2006)

This velocity profile corresponds to a profile for turbulent flow and since the measurements are done with a hand held anemometer the velocities are not considered accurate and to determine the mean velocity it is assumed to be a fair approximation to take the mean value of the two measurements.

The mass flow of the inlet air is then calculated from the velocity  $V_{inlet1}$  using equation (D.3).

$$m_{inlet} = V_{inlet1} \cdot A_{inlet} \cdot \rho \quad [kg/s] \quad (D.3)$$

The fuel consumption is measured in  $l/h$  and then converted to  $kg/s$ . To convert the consumption a density of  $817 \frac{kg \text{ fuel}}{m^3}$  is used (Walker, 2007). To express the mass flow of air and fuel as a function of RPM, linear relations are found. These linear relations are shown in figure D.2 along with the data points obtained in the tests.

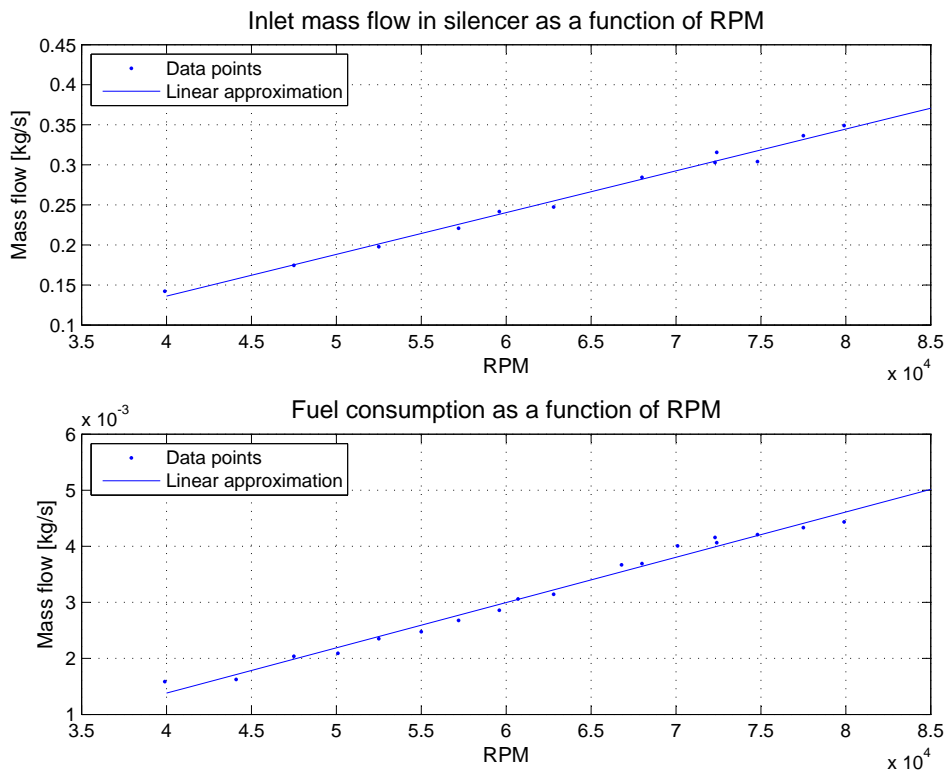
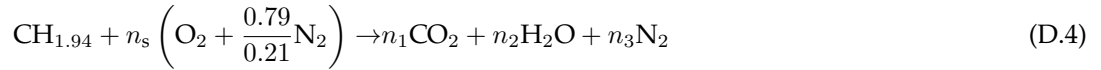


Figure D.2. The fuel consumption and inlet air flow as a function of RPM.

The linear approximations relating fuel consumption and inlet mass flow to the speed are used to determine the AF ratio and  $\lambda$ . The stoichiometric amount of air,  $m_s$ , is found from the stoichiometric reaction given in equation (D.4).  $m_s$  is determined using equation (D.7) from the oxygen balance for the reaction and the molar mass of air.  $n_1$  and  $n_2$  are determined from the carbon and hydrogen balances equations (D.5) and (D.6).



$$n_1 = 1 \quad [\text{kmol}] \quad (\text{D.5})$$

$$n_2 = \frac{1.94}{2} \quad [\text{kmol}] \quad (\text{D.6})$$

$$n_s = \frac{n_2}{2} \quad [\text{kmol}] \quad (\text{D.7})$$

Now equations (D.1) and (D.2) are used to determine the AF and  $\lambda$  and the results are shown in figure D.3.

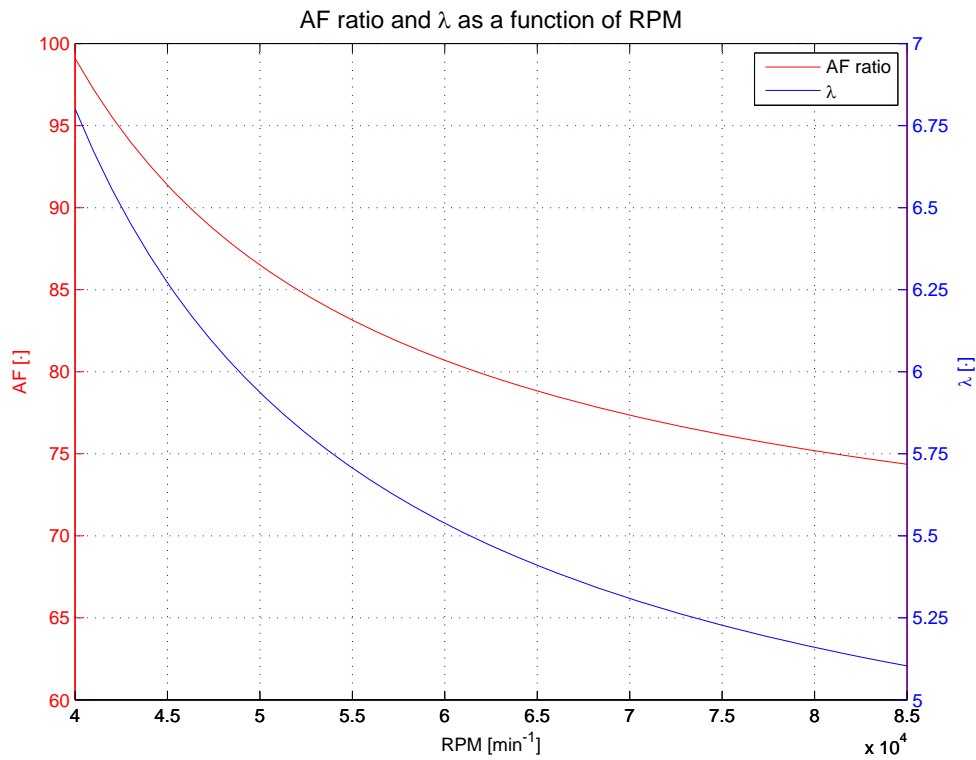


Figure D.3. The AF ratio and excess air  $\lambda$  as a function of RPM.



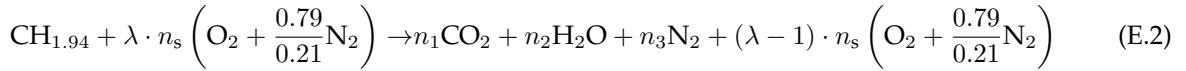
# Estimating the Oxygen Content in the Exhaust Pipe



This appendix determines the oxygen content of the exhaust pipe using the combustion reaction.  $\lambda$  determined in appendix D is used to approximate the oxygen content in the combustion products. The oxygen content is calculated using equation (E.1) as the ratio of the number of moles to the total number of moles in the products.

$$O_2 = \frac{n_{O_2}}{n_{total}} \quad [\text{mole \%}] \quad (\text{E.1})$$

The approximated values are to be compared with an oxygen content measured in the exhaust gas during engine tests described in appendix B. In order to compare the two values they need to have same reference point. To get this the approximated content must be calculated in the exhaust gas and not after the combustion chamber. Thus the amount of surrounding air entering the exhaust pipe  $\Delta n_{sur}$  must be implemented as described in section 3.5. The oxygen content at exhaust outlet is larger than at combustion outlet due to the extra surrounding air entering the exhaust pipe. The combustion reaction, given in equation (E.2), then contains the term given in equation (E.3) related to the mass flow  $\Delta m_{sur}$ .



$$\Delta n_{sur} \left( O_2 + \frac{0.79}{0.21} N_2 \right) \quad (\text{E.3})$$

$n_1, n_2, n_3$  and  $n_s$  relates to the stoichiometric combustion reaction,  $(\lambda - 1) \cdot n_s$  relates to the excess air and  $\Delta n_{sur}$  to the surrounding air entering the test stand through the gaps at inlet and outlet. The relation between  $\Delta n_{sur}$  and the surrounding air is given in equation (E.4).

$$\Delta n_{sur} = n_{sur6} - n_{sur7} \quad [kmol] \quad (\text{E.4})$$

The combustion reaction is used to determine the number of moles of oxygen and the total number of moles in the products. In equations (E.5) and (E.6)  $n_{O_2}$  and  $n_{total}$  are given. Note that the total number of moles of air is the term  $((\lambda - 1) \cdot n_s + \Delta n_{sur})$  multiplied by  $(1 + \frac{0.79}{0.21})$  because there is a total of  $(1 + \frac{0.79}{0.21})$  moles in the composition of air.

$$n_{O_2} = (\lambda - 1) \cdot n_s + \Delta n_{sur} \quad [kmol] \quad (\text{E.5})$$

$$n_{total} = n_1 + n_2 + n_3 + ((\lambda - 1) \cdot n_s + \Delta n_{sur}) \cdot \left( 1 + \frac{0.79}{0.21} \right) \quad [kmol] \quad (\text{E.6})$$

$n_1, n_2, n_3$  and  $n_s$  are determined from the oxygen, carbon, nitrogen and hydrogen balances as described in appendix D. The amount of surrounding air,  $\Delta n_{sur}$ , entering the exhaust pipe is determined from the mass flow of surrounding air,  $\Delta m_{sur}$ , and the molar mass of air. The mass flow of surrounding air is determined from the velocities at inlet and outlet gaps, which are measured using a hot wire anemometer.

Equation (E.7) shows how the velocity is related to the mass flow.

$$m_{\text{sur}} = V_{\text{sur}} \cdot A_{\text{gap}} \cdot \rho \quad \left[ \frac{\text{kg}}{\text{s}} \right] \quad (\text{E.7})$$

The mass flows at inlet and outlet are related to RPM by linear regressions and  $\Delta m_{\text{sur}}$  is also expressed by a linear regression. Figure E.1 shows the measured velocities  $m_{\text{sur}6}$  and  $m_{\text{sur}7}$  at inlet and outlet of the gaps and the linear regressions for  $m_{\text{sur}6}$ ,  $m_{\text{sur}7}$  and  $\Delta m_{\text{sur}}$ .

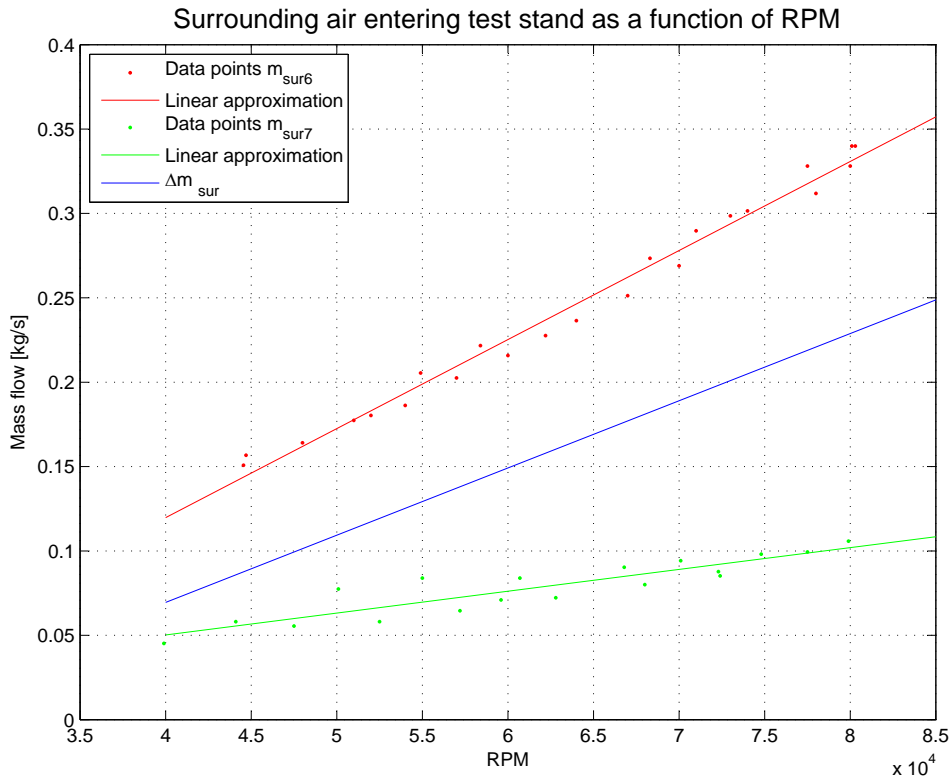


Figure E.1. Data points and approximation of the air mass flow at inlet and outlet gap and an approximation of  $\Delta m_{\text{sur}}$  from the linear approximations.

Now  $n_{O_2}$  and  $n_{total}$  can be determined from equations (E.5) and (E.6) and the oxygen content,  $O_2$ , can be calculated using equation (E.1). Figure E.2 shows the data points of the oxygen content, a linear regression of the data points, the approximated oxygen content at exhaust outlet and the approximated oxygen content at combustion outlet from the combustion reaction without and with the surrounding air respectively.

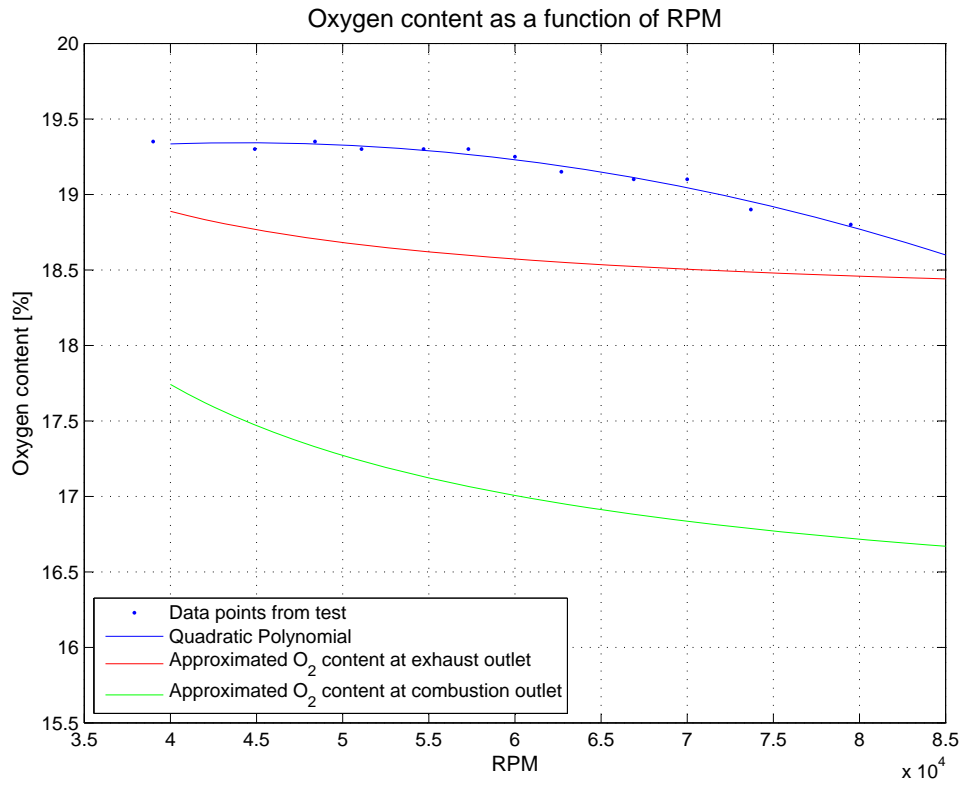


Figure E.2. Data points and approximation of the air mass flow at inlet and outlet gap and an approximation of  $\Delta m_{sur}$  from the linear approximations.



# CD Content F

---

- REFPROP Software as a .RAR file.
- Matlab model and data files.
- CEA Nasa results as .PDF files.
- The report as a .PDF file.
- A folder with the webpages and reports used as references.
- A folder containing all data from test runs.